Chapter 6

Feasibility Study on Magnetically Levitated Planar Actuator

This chapter proposes a conceptual design for a planar actuator having the same configuration for the magnetic circuits as for the planar motion control so that the mover can be magnetically suspended. In addition, it presents a feasibility verification of motion-control characteristics by numerical analysis.

6. Feasibility Study on Magnetically Levitated Planar Actuator

This chapter presents a feasibility verification as to whether a planar actuator can magnetically suspend a mover, capable of 3-DOF motions on a plane, so as to further improve the drive performance of a planar actuator. First, the planar actuator is redesigned so it can both suspend the mover and control the planar motions. Then, the planar motion and magnetic suspension characteristics of the planar actuator are verified by numerical analysis.

6.1. Conceptual Design of Magnetically Levitated Planar Actuator

This section presents a compatibility verification of planar motion and magnetic suspension, and then introduces a conceptual design for a planar actuator with a magnetically suspended mover.

6.1.1. Design Considerations

The proposed planar actuator has spatially superimposed magnetic circuits for the x–, y– and α–directions, which are its most important feature and enable the mover to travel over a wide movable area on a plane by exciting only two polyphase armature conductors. The magnetically levitated planar actuator is also designed so that all the magnetic circuits are mutually superimposed, as in the following methodology:

(i) Compatibility verification of both 3-DOF planar motion and magnetic-suspension controls of the planar actuator designed in Chapter 3.

(ii) Redesign the planar actuator, without increasing the number of the armature conductors, so that planar motion and magnetic suspension are compatible if they are found not to be in (i).

In order to design the planar actuator, a numerical analysis of 6-DOF driving forces for 6-DOF mover positions is performed.

6.1.2. 6-DOF Force Analysis

This section presents an analytical model of driving forces with 6 DOF, and then presents the results of the analysis.

(i) Analytical model for 6-DOF driving forces:

The driving forces, including the suspension forces, greatly depend on the size of the gap between the mover and armature conductors, and therefore this gap needs to be precisely controlled. Generally, reducing this gap increases the driving forces. If the mover is located below the stator, attraction forces to the stator are required to suspend the mover. However, the attraction forces are increased by reducing the gap, which makes the vertical motions of the mover unstable. Conversely, if the mover is located above the stator, repulsion forces from the stator are required to suspend the mover. The repulsion forces are increased by reducing the gap, and so the vertical motions are stable. Therefore, in this study, the mover of the magnetically levitated planar actuator is positioned on the stator.

Figure 6.1.2-1 shows the analytical model for the driving forces. In this figure, the mover and polyphase armature conductors for the x– or y–directions only are shown. A moving 2-D Halbach permanent-magnet array has the same structure as shown in Fig. 3.2.1-1, and four-pole-and-seven-segment magnetization with pole-pitch length τ_{PM} = 3 mm along the x_f– and y_f–directions. Its dimensions are 11 mm × 11 mm × 2 mm, which are almost two-fifths the size of the magnet-array dimension shown in Fig. 3.2.1-1. The ultimate miniaturization of the permanent-magnet mover enables higher accelerations to be generated using the same armature currents and flux density as given in Subsection 3.3.1.

Figure 6.1.2-2 shows an analytically obtained flux-density distribution on the plane 0.5 mm below the mover bottom for the x_m– and y_m–directions. Figure 6.1.2-2 indicates that the permanent-magnet mover also generates a quasi-sinusoidal flux density with a pitch length of τ = 2.1 mm in the x_m– and y_m–directions. On the other hand, pitch lengths of the meander-shaped armature conductors are equal to the pitch τ (= 2.1 mm).

In the mover motions, there are 3-DOF rotations. However, this analysis deals with the rotations around only one axis (x_m, y_m, or z_m). The rotational angles around the x_m–, y_m–, and z_m–axes are referred to as roll angle γ, pitch angle β, and yaw angle α, respectively.

The driving forces acting on the mover can be calculated from the Lorentz force law with the same equations as Eqs. (3.3.1-1)–(3.3.1-8).

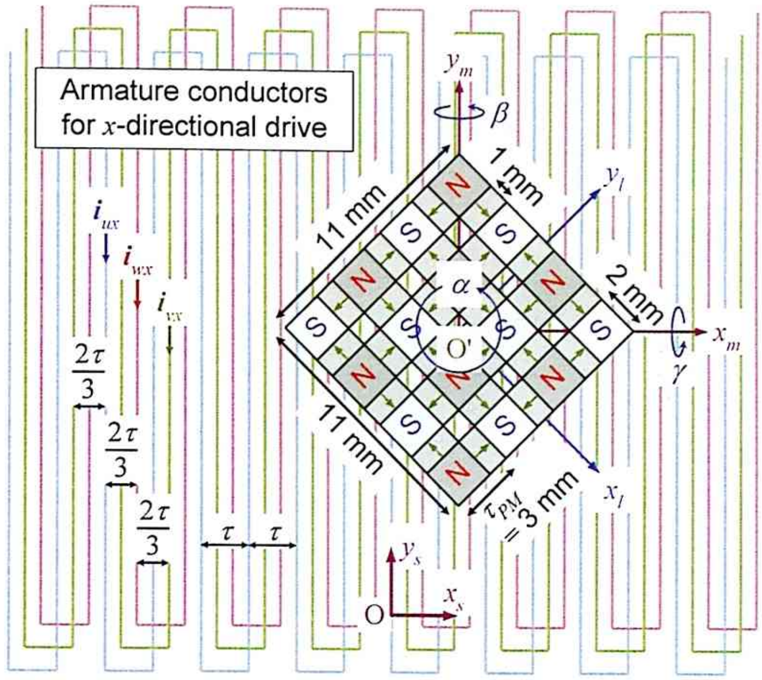

(a) Supplying three-phase currents for the x–directional drive.

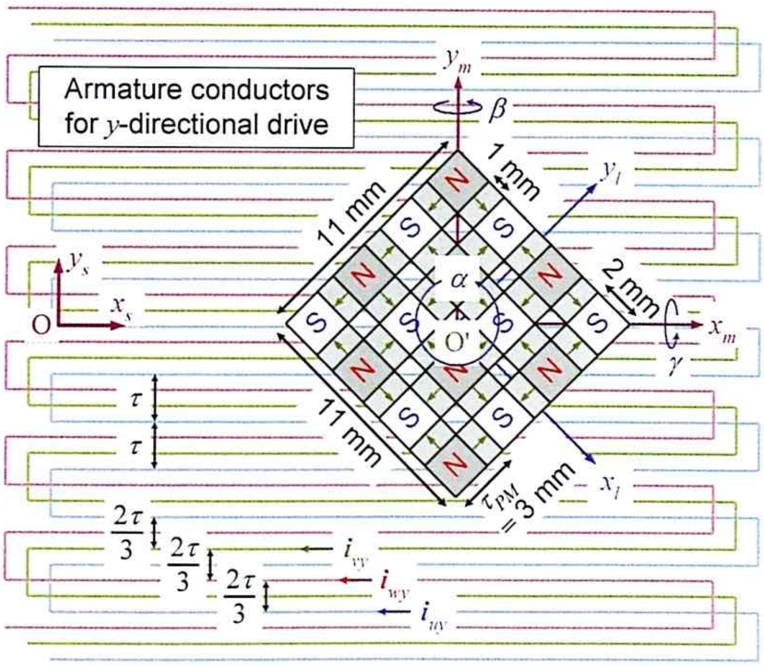

(b) Supplying three-phase currents for the y–directional drive.

Fig. 6.1.2-1: Analytical model for 6-DOF driving forces.

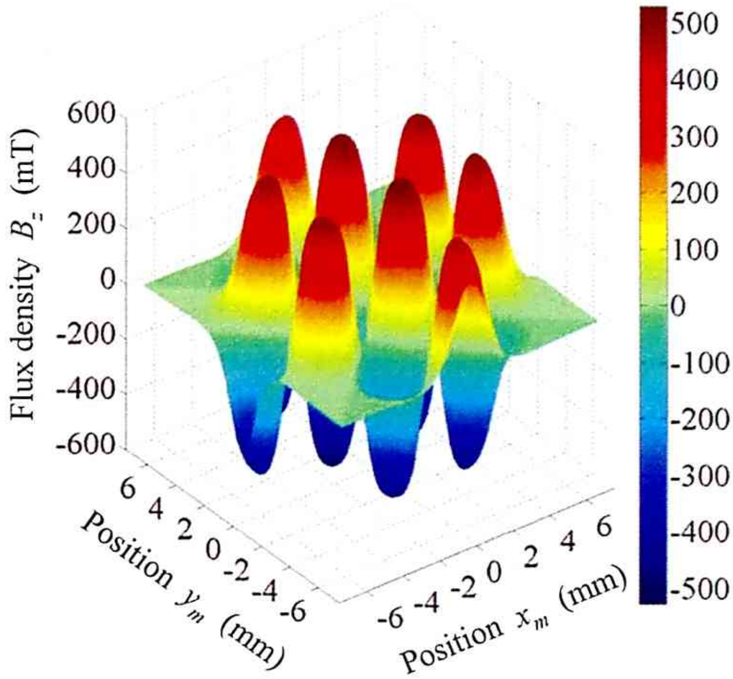

Fig. 6.1.2-2: Flux-density distribution on the plane 0.5 mm below the mover bottom.

(ii) Analysis results for 6-DOF driving forces:

Figure 6.1.2-3 shows the analysis results of the driving forces F_x, F_z, T_x, T_y, T_z for the yaw angle α when the d– and q–axis currents for the x–directional drive are supplied (I_{dx} = 1 A, or I_{qx} = 1 A), the air gap between the mover bottom and armature conductors is 0.5 mm, and the pitch and roll positions are not displaced ($\beta = \gamma = 0$ deg). Figure 6.1.2-3 indicates that the d–axis current generates the translational forces F_z and torques T_z, and the q–axis current generates the translational forces F_x and torques T_x, T_y. The translational forces F_x, F_z and torques T_y are almost constant, and the torques T_x and T_z are proportional to the yaw angle α when the yaw angle $\alpha \approx 0$ deg. Because of the symmetric magnetization of the mover, the same driving forces can be generated every 180 deg.

In the same way, the driving forces resulting from the d– and q–axis currents for the y–directional drive I_{dy}, I_{qy} can be numerically analyzed, and are shown in Fig. 6.1.2-4. From these results, the d–axis currents for the x– and y–directional drives I_{dx} and I_{dy} generate nearly equal translational forces F_z and torques T_z, and therefore cannot be uniquely determined from the total translational forces F_z and torques T_z. In other words, with only the d–axis currents for the x– and y–directional drives I_{dx} and I_{dy}, 2-DOF driving forces cannot be controlled. The torques resulting from the q–axis currents for the x– and y–directional drives I_{qx} and I_{qy} are similar because of the symmetry of the actuator.

When the yaw angle $\alpha = \pm 24.7$ deg and ± 45 deg, 3-DOF translational forces cannot be generated regardless of the magnitudes of the d– and q–axis currents I_{dx}, I_{qx}. This is presumed to be caused by the magnetic field resulting from magnet mover, which is tilted an angle of 24.7 deg or 45 deg.

The mover generates opposite magnetic poles every pitch length τ in the y_m–direction, and so the magnetic poles at a position and 5τ-distant position along the y_m–direction are mutually opposite as shown in Fig. 6.1.2-5. When tilted by $\alpha_0 = 23.6$ deg (close to 24.7 deg) in the α–direction, the mover generates opposite magnetic poles every 2τ along the x_s–direction as shown in Fig. 6.1.2-5 because of geometry relation as shown in the following equation:

$$\alpha_0 = \sin^{-1}\left(\frac{2\tau}{5\tau}\right) = 23.6 \text{ deg} . \qquad (6.1.2\text{-}1)$$

Then, the same armature currents flow every 2τ along the x_s–direction. Therefore, if the magnet mover generates a completely-sinusoidal magnetic field distribution in the x_m– and y_m–directions, each phase current generates opposite translational forces every 2τ in the x_s–direction during the yaw angle $\alpha = 23.6$ deg. Consequently, these opposite translational forces can be mutually offset. The error between the theoretically (23.6 deg) and analytically (24.7 deg) obtained yaw angle is presumed to be caused by an incomplete sinusoidal magnetic field generated by the magnet mover.

As mentioned in Subsection 3.2.1, the miniaturized mover also generates a quasi-sinusoidal flux density in the x_l– and y_l–directions. When the mover is tilted by 45 deg in the α–direction as shown in Fig. 6.1.2-6, the flux densities B_x, B_y, B_z below the mover are approximately expressed as follows:

$$B_x(x_l, y_l, z_s) = -B_{zm}(z_s)\sin\left(\frac{\pi}{\tau_{PM}}x_l\right)\cos\left(\frac{\pi}{\tau_{PM}}y_l\right) \qquad (6.1.2\text{-}2)$$

$$B_y(x_l, y_l, z_s) = B_{zm}(z_s)\cos\left(\frac{\pi}{\tau_{PM}}x_l\right)\sin\left(\frac{\pi}{\tau_{PM}}y_l\right) \qquad (6.1.2\text{-}3)$$

$$B_z(x_l, y_l, z_s) = B_{zm}(z_s)\sin\left(\frac{\pi}{\tau_{PM}}x_l\right)\sin\left(\frac{\pi}{\tau_{PM}}y_l\right) \qquad (6.1.2\text{-}4)$$

So, armature currents flowing through a line l_{jk} ($j = x$ or y, $k = u$, v, or w) in armature conductors, i_{jk} generate no translational force because average of the flux densities B_x, B_y, B_z with respect to the y_s–direction is nearly equal to zero, that is, translational force $\boldsymbol{F}$, shown in Eq. (3.3.1-3), is expressed as follows:

$$\int_{jk} B_x\, dy_s \approx 0, \quad \int_{jk} B_y\, dy_s \approx 0, \quad \int_{jk} B_z\, dy_s \approx 0 \qquad (6.1.2\text{-}5)$$

$$\boldsymbol{F} = -\sum_{j,k} \int_{jk} \left(\boldsymbol{i}_{jk} \times \boldsymbol{B}\right) dl_{jk} \approx 0 \qquad (6.1.2\text{-}6)$$

Figures 6.1.2-3 and 6.1.2-4 also indicate that a magnitude of torque T_z resulting from the mover tiled by 24.7 deg is larger than that by 45 deg. Magnitudes of torques T_x and T_y resulting from the mover tiled by 45 deg are equal because flux density resulting from the magnet mover is symmetrically distributed in the x_s– and y_s–directions. On the other hand, magnitudes of torques T_x and T_y resulting from the mover tiled by 24.7 deg are not equal because of asymmetric distribution of the flux density in the x_s– and y_s–directions.

Figures 6.1.2-7 and 6.1.2-8 show the analysis results of the torques T_x, T_y, T_z for the pitch angle β when the d– and q–axis currents are supplied (I_{dx} = 1 A, I_{qx} = 1 A, I_{dy} = 1 A, or I_{qy} = 1 A), the yaw and roll positions are not displaced ($\alpha = \gamma = 0$ deg). From these results, it can be seen that the d–axis currents generate the torques T_y proportional to the pitch angle β, and the q–axis currents generates the almost constant torques T_y. Figure 6.1.2-9 shows schematic views of the generation of the torques T_y. The q–axis current for the y–directional drive also generates the torques T_z proportional to the pitch angle β.

Figures 6.1.2-10 and 6.1.2-11 show the analysis results of the torques T_x, T_y, T_z for the roll angle γ when the d– and q–axis currents are supplied (I_{dx} = 1 A, I_{qx} = 1 A, I_{dy} = 1 A, or I_{qy} = 1 A), the yaw and pitch positions are not displaced ($\alpha = \beta = 0$ deg). From these results, it can be seen that the d–axis currents generates the torques T_x proportional to the roll angle γ, and the q–axis currents generates the almost constant torques T_x. Figure 6.1.2-12 shows schematic views of the generation of the torques T_x. The q–axis current for the x–directional drive also generates the torques T_z proportional to the roll angle γ.

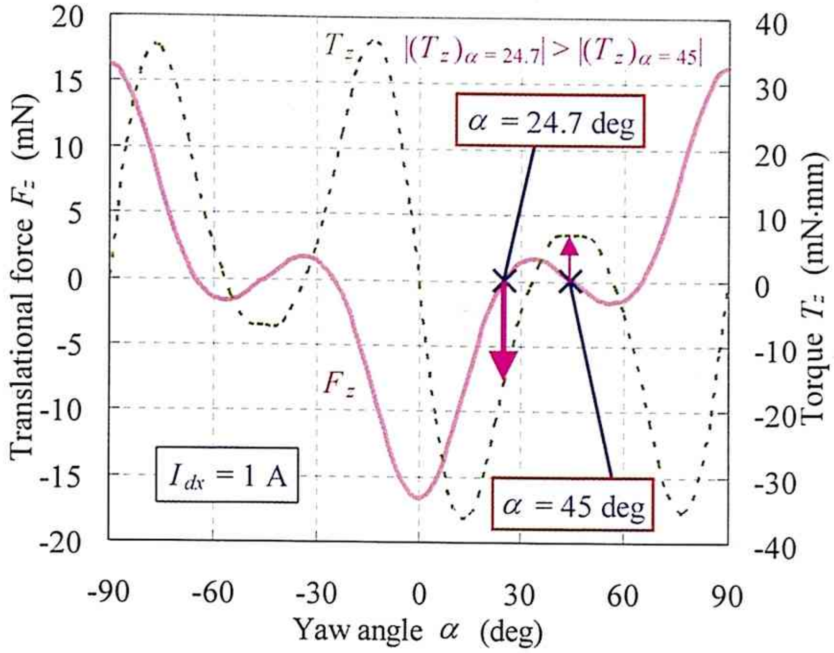

(a) Driving forces from the d–axis current for the x–directional drive I_{dx} = 1 A.

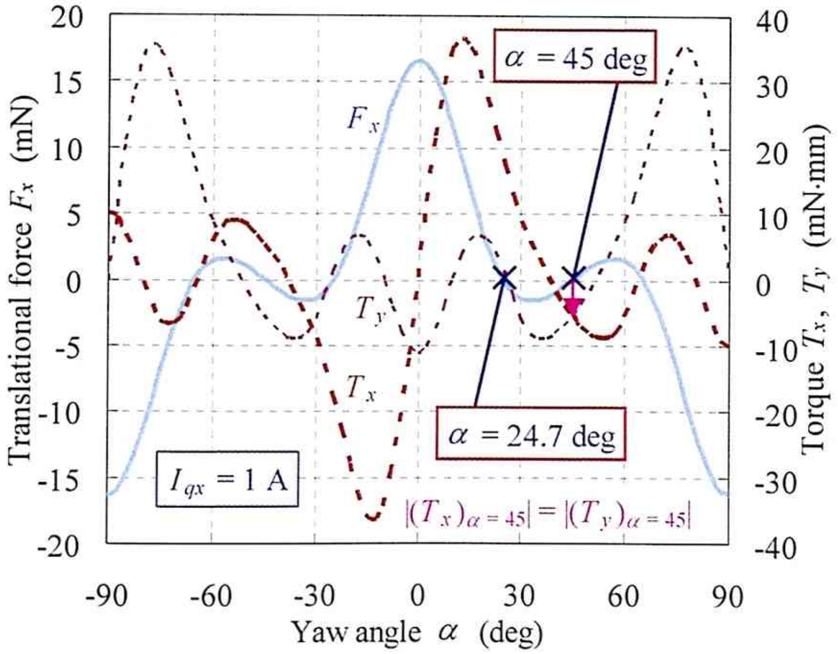

(b) Driving forces from the q–axis current for the x–directional drive I_{qx} = 1 A.

Fig. 6.1.2-3: Driving forces for yaw angle α at pitch and roll angles $\beta = \gamma = 0$ deg when the armature currents for the x–directional drive are supplied.

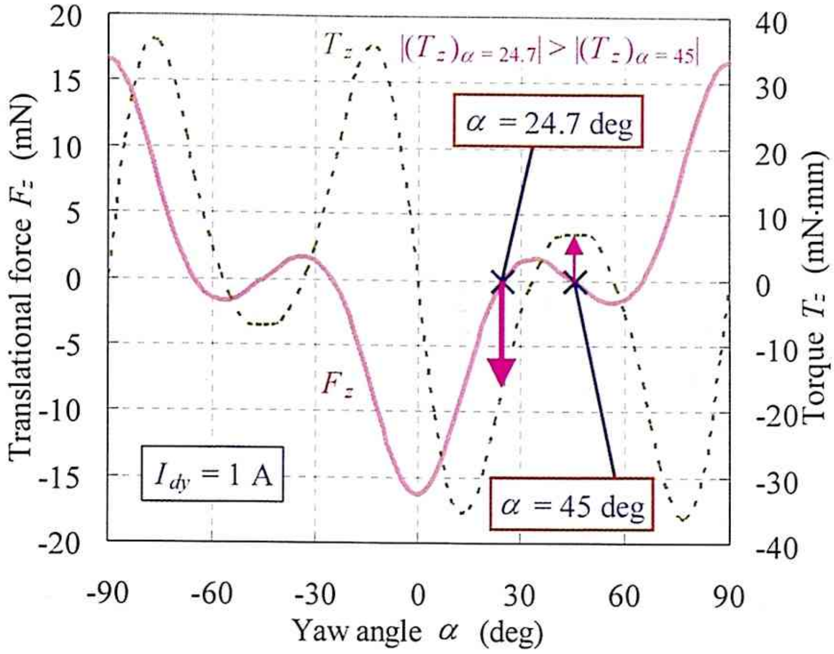

(a) Driving forces from the d–axis current for the y–directional drive $I_{dy} = 1$ A.

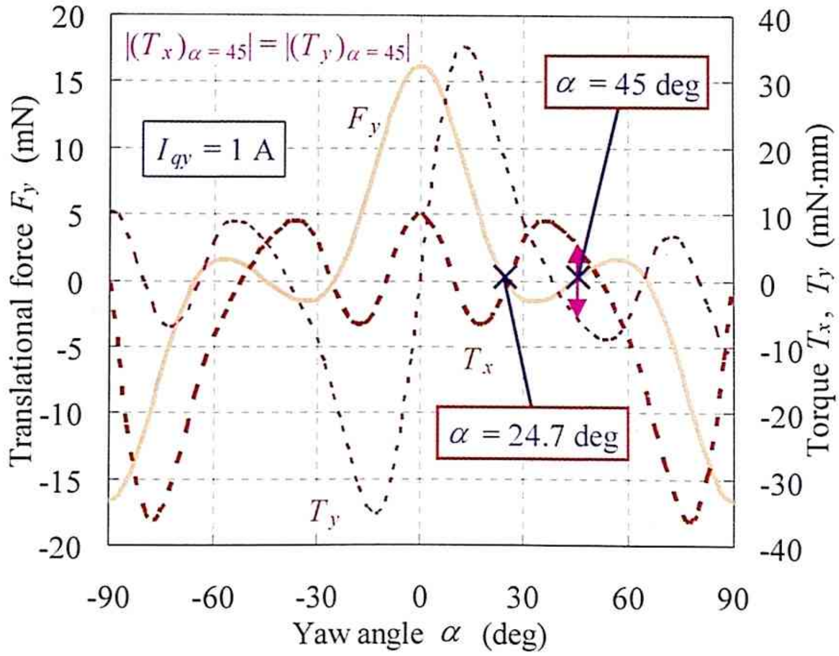

(b) Driving forces from the q–axis current for the y–directional drive $I_{qy} = 1$ A.

Fig. 6.1.2-4: Driving forces for yaw angle α at pitch and roll angles $\beta = \gamma = 0$ deg when the armature currents for the y–directional drive are supplied.

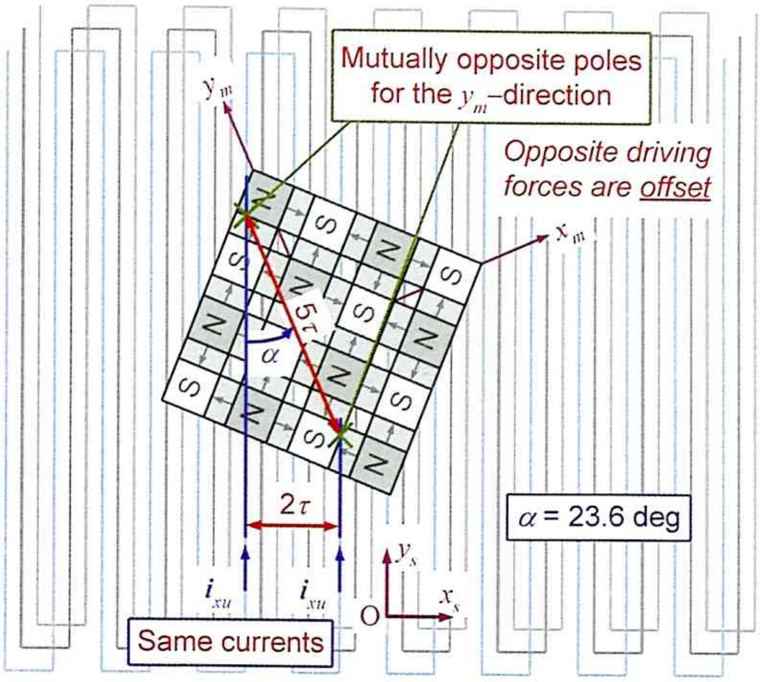

Fig. 6.1.2-5: Relation between pitch lengths of the meander shape and magnetic pole when the yaw angle $\alpha = 23.6$ deg.

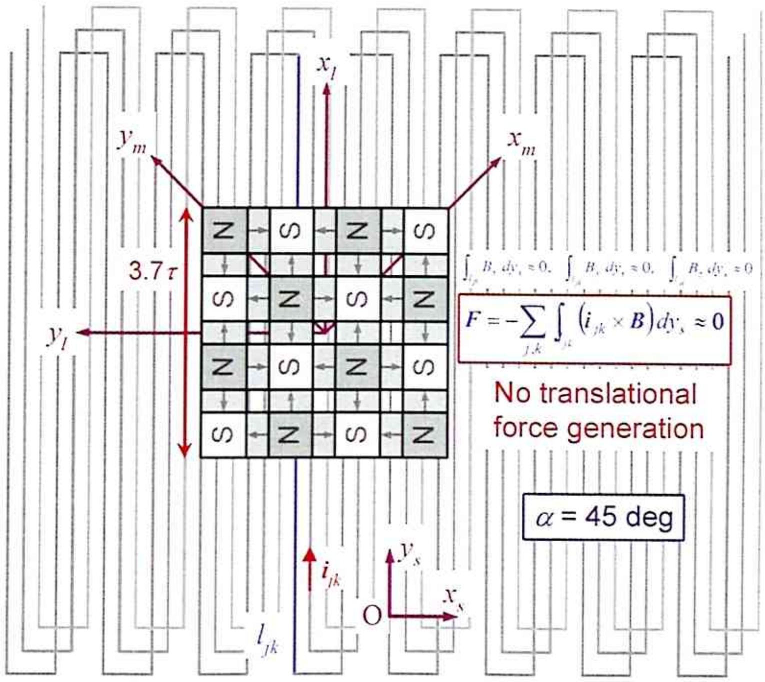

Fig. 6.1.2-6: Integration of flux density B_z along a line l_{jk} in armature conductors when the yaw angle $\alpha = 45$ deg.

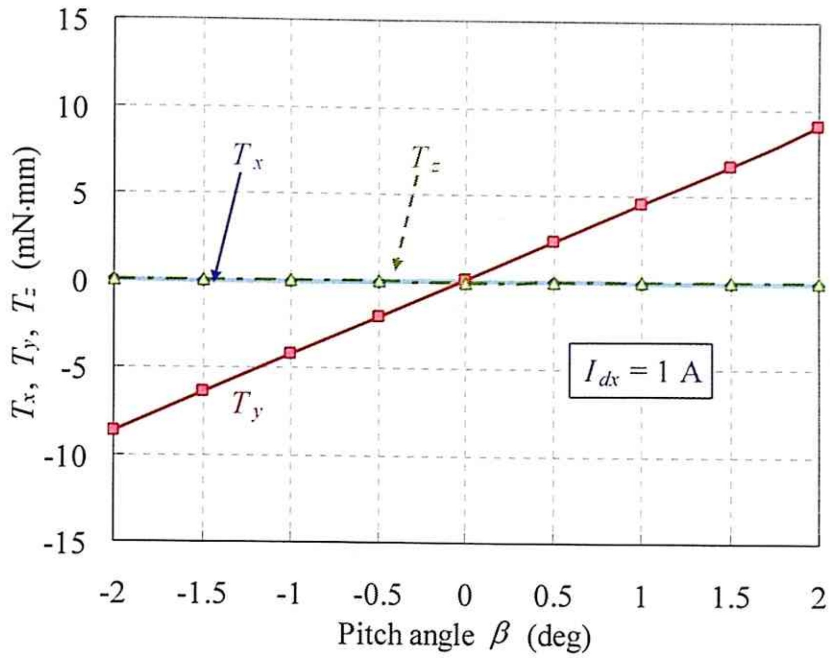

(a) Driving forces due to the d–axis current for the x–directional drive I_{dx} = 1 A.

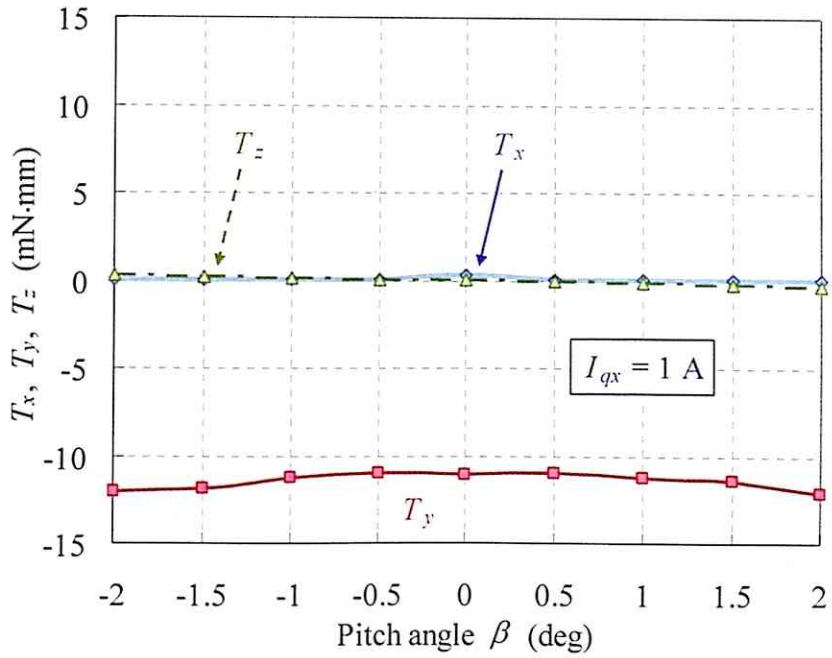

(b) Driving forces due to the q–axis current for the x–directional drive I_{qx} = 1 A.

Fig. 6.1.2-7: Driving forces for pitch angle β at yaw and roll angles $\alpha = \gamma = 0$ deg when the armature currents for the x–directional drive are supplied.

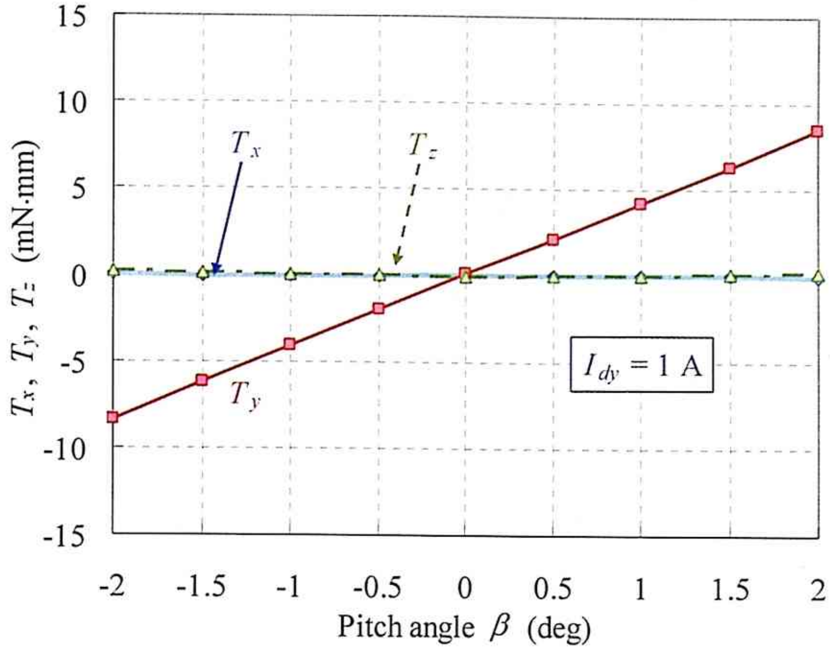

(a) Driving forces due to the d–axis current for the y–directional drive I_{dy} = 1 A.

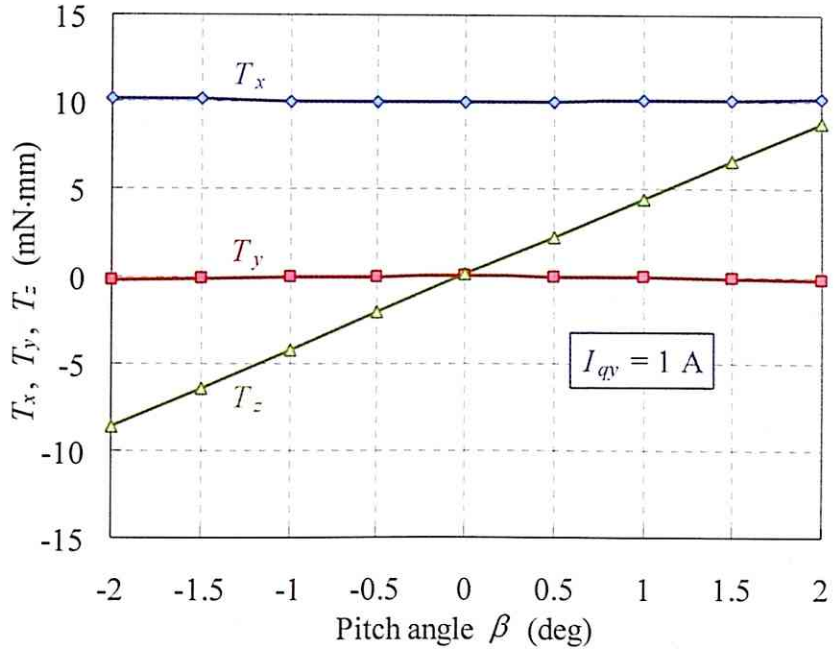

(b) Driving forces due to the q–axis current for the y–directional drive I_{qy} = 1 A.

Fig. 6.1.2-8: Driving forces for pitch angle β at yaw and roll angles $\alpha = \gamma = 0$ deg when the armature currents for the y–directional drive are supplied.

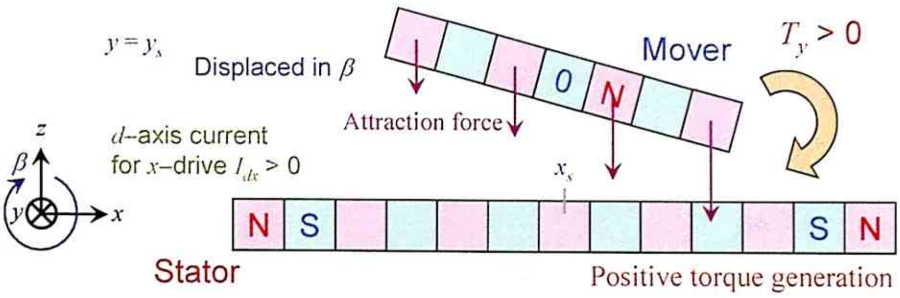

(a) Generated torques T_y from the d–axis current for the x–directional drive.

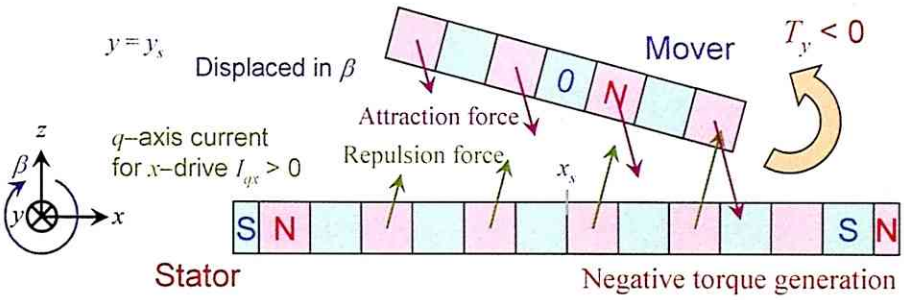

(b) Generated torques T_y from the q–axis current for the x–directional drive.

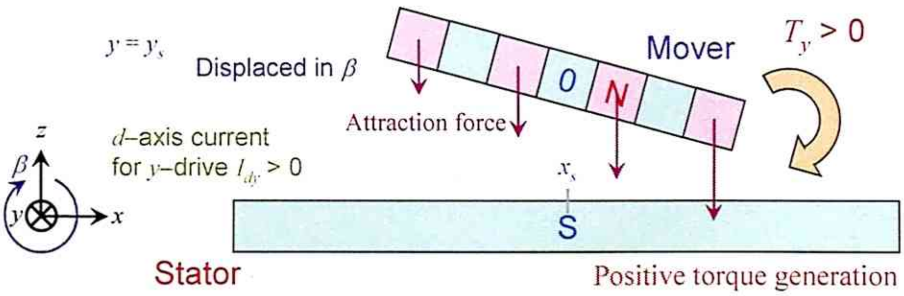

(c) Generated torques T_y from the d–axis current for the y–directional drive.

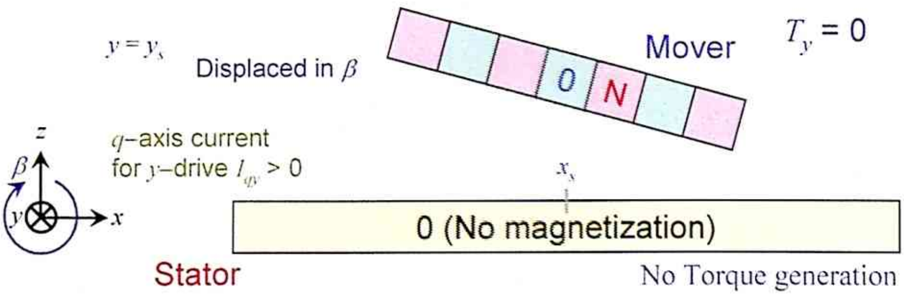

(d) Generated torques T_y from the q–axis current for the y–directional drive.

Fig. 6.1.2-9: Schematic views of generation of torques T_y.

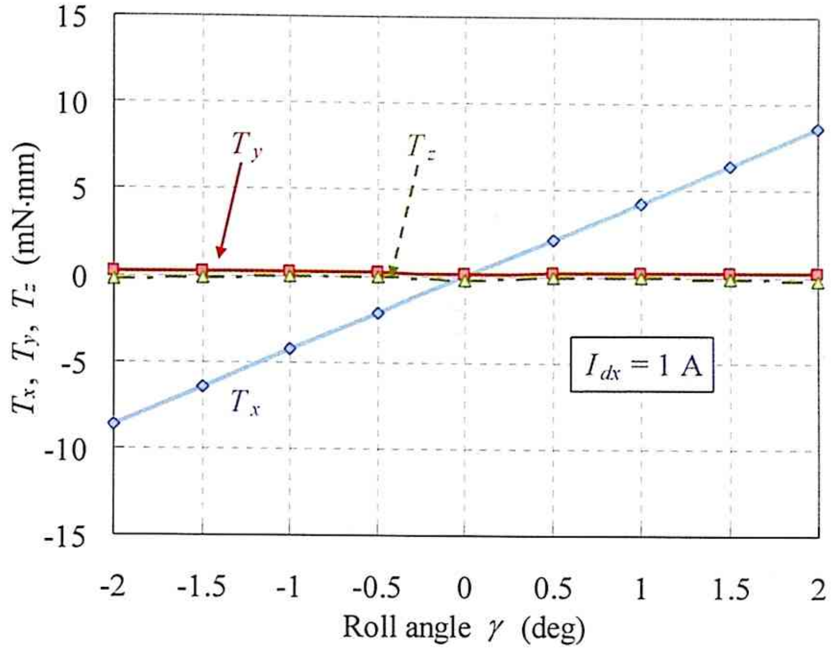

(a) Driving forces due to the d–axis current for the x–directional drive I_{dx} = 1 A.

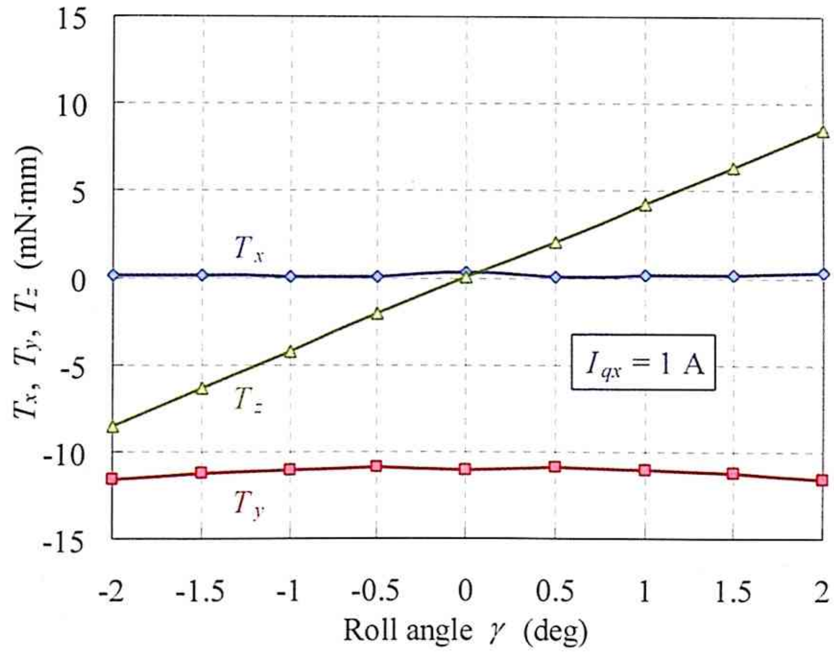

(b) Driving forces due to the q–axis current for the x–directional drive I_{qx} = 1 A.

Fig. 6.1.2-10: Driving forces for roll angle γ at yaw and pitch angles $\alpha = \beta = 0$ deg when the armature currents for the x–directional drive are supplied.

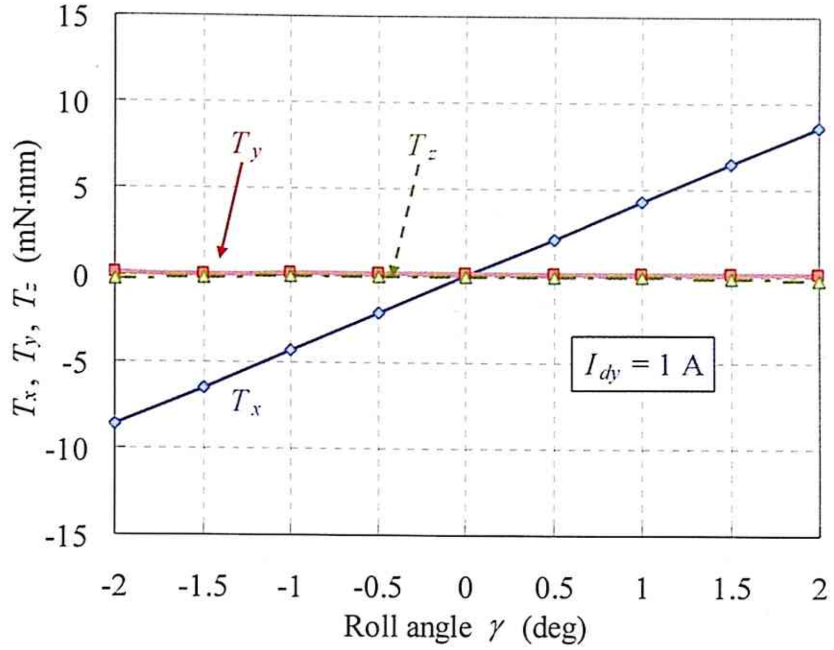

(a) Driving forces due to the d–axis current for the y–directional drive I_{dy} = 1 A.

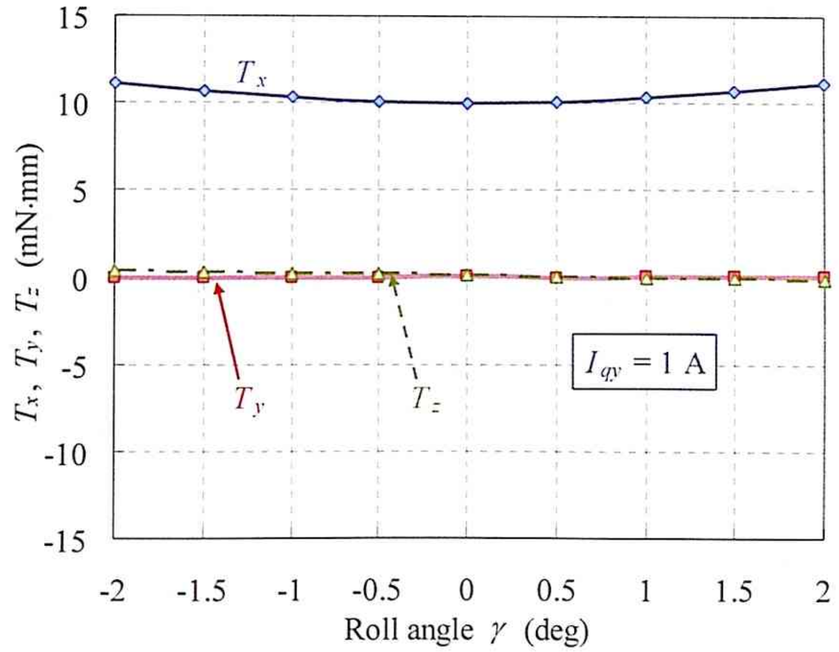

(b) Driving forces due to the q–axis current for the y–directional drive I_{qy} = 1 A.

Fig. 6.1.2-11: Driving forces for roll angle γ at yaw and pitch angles $\alpha = \beta = 0$ deg when the armature currents for the y–directional drive are supplied.

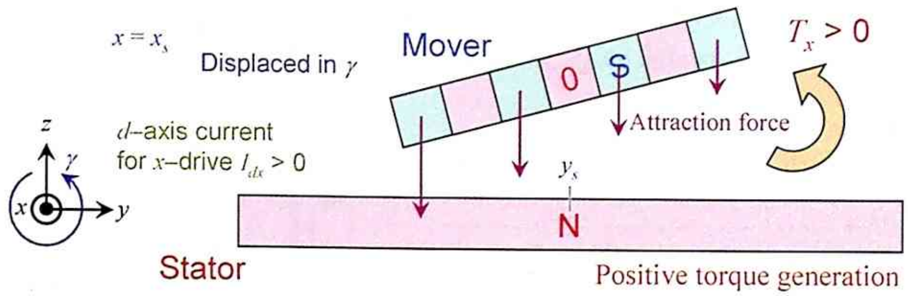

(a) Generated torques T_x due to the d–axis current for the x–directional drive.

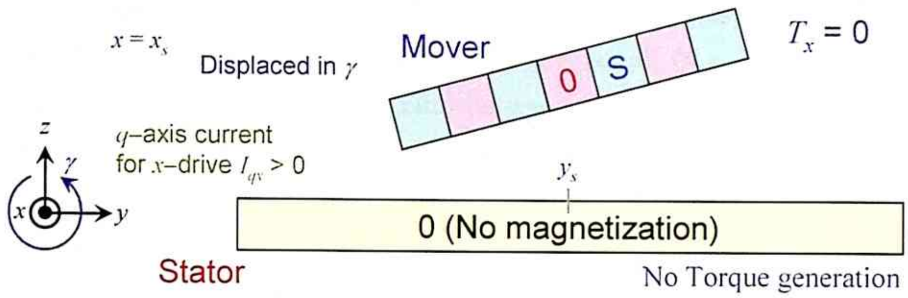

(b) Generated torques T_x due to the q–axis current for the x–directional drive.

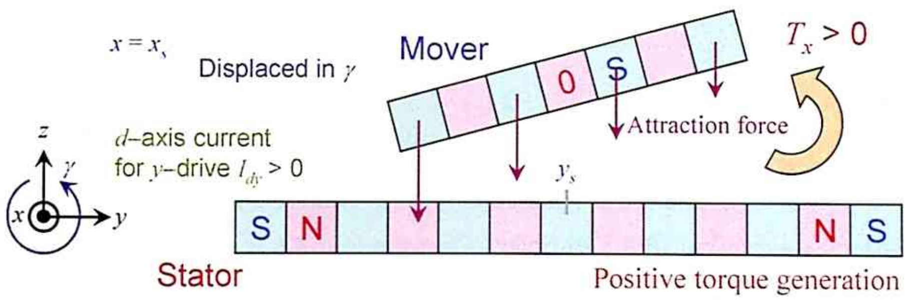

(c) Generated torques T_x due to the d–axis current for the y–directional drive.

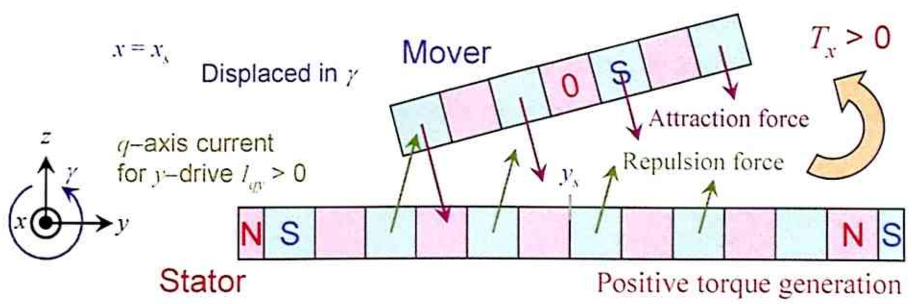

(d) Generated torques T_x due to the q–axis current for the y–directional drive.

Fig. 6.1.2-12: Schematic views of generation of torques T_x.

As the analysis results above show, the driving forces F_x, F_y, F_z, T_x, T_y, T_z can be expressed from the d– and q–axis currents I_{dx}, I_{qx}, I_{dy}, I_{qy} as follows:

$$\begin{bmatrix} F_x \\ F_y \\ F_z \\ T_x \\ T_y \\ T_z \end{bmatrix} = \begin{bmatrix} \boldsymbol{K}_{FT}(\alpha, \beta, \gamma) \\ 6 \times 4 \text{ matrix} \end{bmatrix} \begin{bmatrix} I_{dx} \\ I_{qx} \\ I_{dy} \\ I_{qy} \end{bmatrix} \quad \cdots\cdots (6.1.2\text{-}7)$$

where $\boldsymbol{K}_{FT}$ is a 6 × 4 matrix and all elements of the matrix nonlinearly depend on the yaw angle α, pitch angle β, and roll angle γ. In this study, the pitch and roll displacements of the mover are assumed to be very small ($\beta \approx 0$ deg and $\gamma \approx 0$ deg) because of small air gap (less than 1 mm) between the mover and stator, and in the range, all elements of $\boldsymbol{K}_{FT}$ almost linearly depend on the pitch and roll displacements. Furthermore, if the yaw displacements are assumed also to be very small ($\alpha \approx 0$ deg), all elements of $\boldsymbol{K}_{FT}$ almost linearly depend on the yaw displacements, and the system-constant matrix $\boldsymbol{K}_{FT}$ is expressed approximately as follows:

$$\begin{bmatrix} F_x \\ F_y \\ F_z \\ T_x \\ T_y \\ T_z \end{bmatrix} = \begin{bmatrix} 0 & K_{FC} & 0 & 0 \\ 0 & 0 & 0 & K_{FC} \\ -K_{FC} & 0 & -K_{FC} & 0 \\ K_{TP}\gamma & K_{TP}\alpha & K_{TP}\gamma & K_{TC} \\ K_{TP}\beta & -K_{TC} & K_{TP}\beta & K_{TP}\alpha \\ -K_{TP}\alpha & K_{TP}\gamma & -K_{TP}\alpha & K_{TP}\beta \end{bmatrix} \begin{bmatrix} I_{dx} \\ I_{qx} \\ I_{dy} \\ I_{qy} \end{bmatrix} \quad \cdots\cdots (6.1.2\text{-}8)$$

where K_{FC}, K_{TC}, and K_{TP} are constant (in this analysis, for a 0.5-mm air gap, $K_{FC} \approx 17$ mN, $K_{TC} \approx 12$ mN·mm, and $K_{TP} \approx 4.5$ mN·mm). Equation (6.1.2-8) indicates that the driving forces due to the d–axis currents I_{dx} and I_{dy} are equal because of the symmetry of the actuator. Therefore, even if the two currents I_{dx} and I_{dy} are controlled, only 1-DOF driving forces can be controlled in the range within $\alpha \approx 0$ deg, $\beta \approx 0$ deg, and $\gamma \approx 0$ deg. Therefore, controlling the four armature currents in the dq–frame controls the 3-DOF motions of the mover (for instance, x–, y– and z–motions, or x–, y–, and α–motions). In order to realize both 3-DOF motion controls on a plane and magnetic suspension, the planar actuator needs to be redesigned.

6.1.3. Conceptual Design of Fundamental Structure

In order to suspend the mover, suspension forces that balance the force of gravity need to be generated. Equation (6.1.2-3) indicates that negative d–axis currents (I_{dx}, I_{dy} < 0) generate suspension forces (F_z > 0). Figure 6.1.3-1 shows schematic views of when the d–axis currents are supplied. Negative d–axis currents to actively control levitation forces (F_z > 0) always generate restoring torques against the β– and γ– displacements. The restoring torques stabilize the β– and γ–motions of the mover.

Equation (6.1.2-3) also shows that the q–axis currents I_{qx}, I_{qy} generate the translational forces F_x, F_y on a plane without vertical forces F_z. Therefore, the d– and q–axis currents I_{dx}, I_{qx}, I_{dy}, I_{qy} :

- independently control the translational forces F_x, F_y, F_z
- stabilize the pitch and roll motions.

However, the d–axis currents utilized to control the suspension forces F_z, generate yaw-directional torques proportional to the yaw angle α, that is, they generate instable yaw motions. Therefore, in order to realize both 3-DOF motion controls on a plane and magnetic suspension, a stabilization mechanism for the yaw motions is needed.

Then, we can consider the following two methods toward addition of the stabilization mechanism; redesign of structures of the permanent-magnet mover or stationary armature conductors. Fabricating the permanent-magnet mover is difficult in bonding each permanent-magnet component. On the other hand, the armature conductors can be flexibly and easily manufactured by means of multilayered printed circuits. In this study, the armature conductors are redesigned to offer stable yaw motion with less interference to the translational, pitch, and roll motions.

The torques acting on the mover depend on the relative yaw, pitch, and roll distances between the mover and the armature conductors, but relative pitch and roll distances should be always nearly equal to 0 deg in order to maintain a small air gap. The torques also depend on pitch lengths of the armature conductors, which determine an allowable maximum width of those as shown in Fig. 6.1.3-2. The width of the armature conductors also determines an allowable maximum current of those, and so design of the armature conductors including pitch lengths as a parameter tends to become complicate.

In this study, new armature conductors with different relative distances in the yaw direction from the armature conductors for the x– and y–directional drives are introduced to control the yaw motion as shown in Fig. 6.1.3-3.

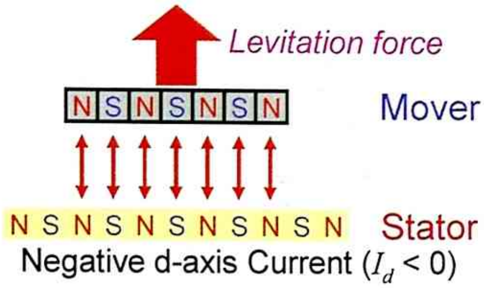

(a) Generation of the levitation forces F_z.

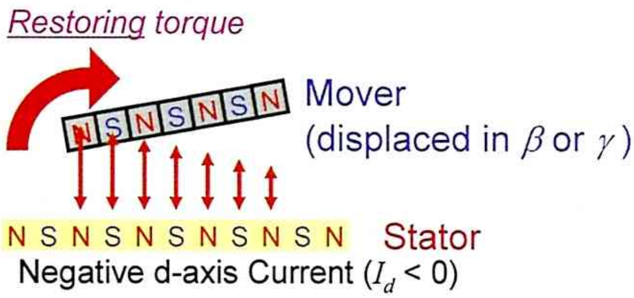

(b) Generation of the restoring torques T_y and T_x.

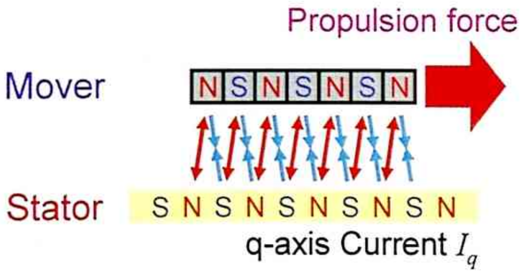

(c) Generation of the propulsion forces F_x and F_y.

Fig. 6.1.3-1: Conceptual design of a magnetically levitated planar actuator.

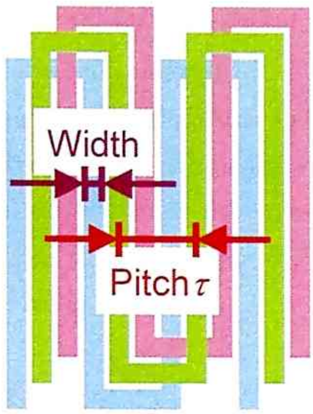

Fig. 6.1.3-2: Allowable maximum width of the armature conductors determined by pitch length of those.

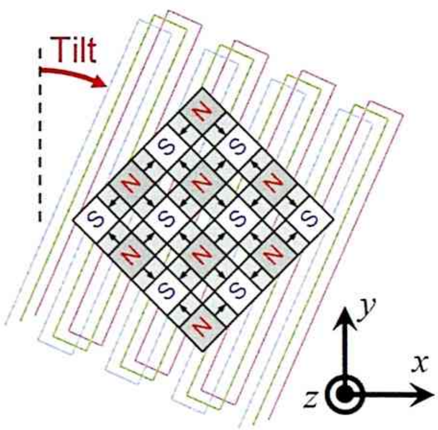

Fig. 6.1.3-3: New introduced armature conductors tilted in the yaw direction.

Figures 6.1.2-3 and 6.1.2-4 indicates that the d–axis current generates translational forces F_z and torques T_z, and the q–axis current generates translational forces F_x, F_y and torques T_x, T_y when the pitch and roll positions are not displaced ($\beta = \gamma = 0$ deg). So, at least four kinds of the q–axis currents, that is, four pairs of polyphase currents are needed to actively control 6-DOF motions.

Furthermore, Figs. 6.1.2-3 and 6.1.2-4 indicate that the d– and q–axis currents generate only torques without translational forces when the relative yaw distance is 24.7 deg or 45 deg. As mentioned in Subsection 6.1.2, a magnitude of torque T_z resulting from the mover tiled by 24.7 deg is larger than that by 45 deg. Therefore in this study, the armature conductors are tilted by 24.7 deg in the yaw direction from the armature conductors for the x–directional drive, I term this arrangement "armature conductors for the α–directional drive." When the yaw angle of the mover α = 0 deg, the d–axis currents for the α–directional drive $I_{d\alpha}$:

- generate only torques T_z
- without vertical forces F_z.

Therefore, the d–axis currents $I_{d\alpha}$ can separate the generation of the vertical forces F_z and torques T_z, and stabilize the yaw motion. To date, the d– and q–axis currents are generated by three-phase currents, but they can be also be generated by two-phase currents. In this study, a magnetically levitated planar actuator with three pairs of two-phase armature conductors is organized as shown in Fig. 6.1.3-4. Tables 6.1.3-1 and 6.1.3-2 show the specifications of the miniaturized permanent-magnet mover and a triple-layered printed circuit board mounting armature conductors, respectively.

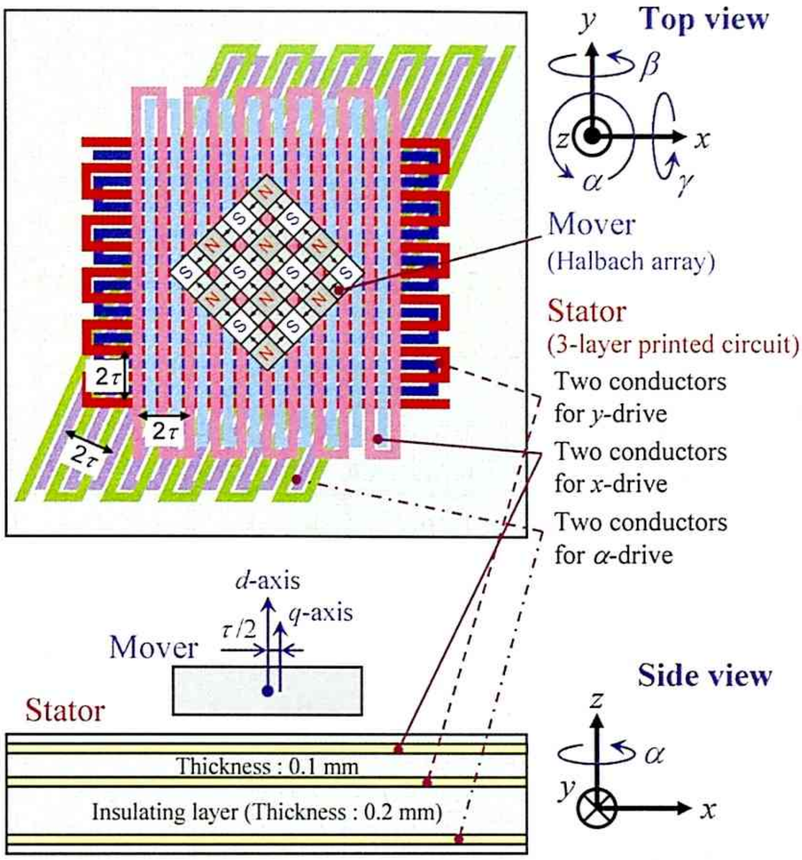

(a) Fundamental structure.

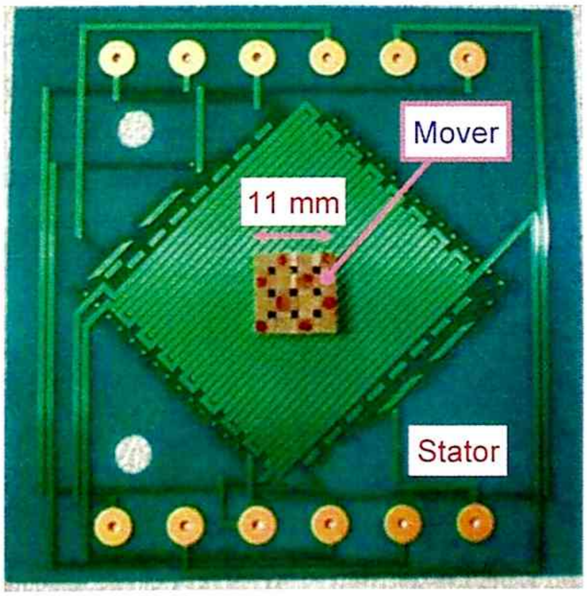

(b) Manufactured stator and mover.

Fig. 6.1.3-4: Magnetically levitated planar actuator.

Table 6.1.3-1: Specifications of miniaturized permanent-magnet mover.

Material	NdFeB (Shin-Etsu Chemical Co., Ltd.)
Residual flux density B_r	1.35 – 1.41 T
Overall dimension	11 mm × 11 mm × 2 mm
PM component	2 mm × 2 mm × 2 mm, or 2 mm × 1 mm × 2 mm
Total mass	1.8 g

Table 6.1.3-2: Specifications of triple-layered printed circuit board.

Number of conductor layers	3
Pitch of meander pattern, τ	2.1 mm
Number of turns of meander pattern	16
Width of conductors	0.8 mm
Thickness of conductors	30 – 35 μm
Thickness of insulating layer	0.1, or 0.2 mm
Resistance of each conductor	1.0 Ω

6.2. Dynamic Behavior of Mover

The mover has 3-DOF translational and rotational motions because there is no mechanical suspension mechanism. When the physical quantities of the mover motion are represented, it is extremely important what coordinates are respected. The translational motions are often represented with respect to the stationary coordinate, and the rotational motions are often represented with respect to the mover coordinate. This section introduces an equation for the 6-DOF motions of the mover that describes the dynamic behavior.

6.2.1. Mass and Inertia Tensor

The mass M and inertia tensor $\boldsymbol{J}_m'$ of the mover are determined by mass density and dimensions. The mass M was measured using an electronic scale (LIBROR, EB-3200B, Shimadzu Corp.) that has a 0.1-g resolution. The scale indicated that mass M = 1.8 g, which agreed with the theoretical value calculated from mass density ρ = 7.60 × 10^3 kg/m^3 and volume V = 224 mm^3. The inertia tensor $\boldsymbol{J}_m'$ with respect to the mover-coordinate axes $x_m y_m z_m$ with an origin at O', corresponding to the center of mass of the mover shown in Fig. 6.2.1-1, can be represented as a 3 × 3 matrix as follows:

$$\boldsymbol{J}_m' = \begin{bmatrix} J_{xx}' & J_{xy}' & J_{xz}' \\ J_{yx}' & J_{yy}' & J_{yz}' \\ J_{zx}' & J_{zy}' & J_{zz}' \end{bmatrix} \quad \text{(6.2.1-1)}$$

where the diagonal elements J_{xx}', J_{yy}', and J_{zz}' are the moments of the inertia about the x_m–, y_m–, and z_m–axes passing through the center of mass of the mover, respectively, and the off-diagonal elements J_{xy}', J_{yx}', J_{yz}', J_{zy}', J_{zx}', and J_{xz}' are the products of the inertia. These elements can be defined as the following equation:

$$J_{jk}' = \int_V \rho(\boldsymbol{r})\left(r^2 \delta_{jk} - r_j r_k\right) dV \quad \text{(6.2.1-2)}$$

where ρ is mass density, $\boldsymbol{r} = [r_1 \quad r_2 \quad r_3]^T$ is a position vector from rotation center with respect to the mover-coordinate axes $x_m y_m z_m$, r_j and r_k (j, k = 1, 2, 3) are elements of the position vector $\boldsymbol{r}$, and δ_{jk} is Kronecker delta. An inertia tensor $\boldsymbol{J}_O'$ of a rectangular prism, which has uniform mass density ρ, with respect to the coordinate axes $x_s y_s z_s$ with the origin at O can be represented as follows:

$$J_{O}'=\begin{bmatrix} \frac{1}{12}M\left(l_y^2+l_z^2\right) & 0 & 0 \\ 0 & \frac{1}{12}M\left(l_z^2+l_x^2\right) & 0 \\ 0 & 0 & \frac{1}{12}M\left(l_x^2+l_y^2\right) \end{bmatrix} \quad \text{(6.2.1-3)}$$

where l_x, l_y, and l_z are the lengths of the edges of the prism as shown in Fig. 6.2.1-2. Next, we can easily calculate the inertia tensor J_{O_t}' of the same prism with respect to the coordinate axes $x_ty_tz_t$ with the origin at O_t parallel to the coordinate $x_sy_sz_s$ with each other as follows:

$$J_{O_t}'=J_{O}'+M\begin{bmatrix} b^2+c^2 & -ab & -ac \\ -ba & c^2+a^2 & -bc \\ -ca & -cb & a^2+b^2 \end{bmatrix} \quad \text{(6.2.1-4)}$$

where $\boldsymbol{d}_t = [a \quad b \quad c]^T$ is the displacement vector from the origin O to the origin O_t. The inertia tensor $\boldsymbol{J}_m'$ of the mover with respect to the coordinate axes $x_sy_sz_s$ $\boldsymbol{J}_s'$ can be calculated from Eqs. (6.2.1-3) and (6.2.1-4) as follows:

$$\boldsymbol{J}_s'=\begin{bmatrix} 0.1828 & 0 & 0 \\ 0 & 0.1828 & 0 \\ 0 & 0 & 0.3543 \end{bmatrix}\times 10^{-7} \ \text{kg·m}^2. \quad \text{(6.2.1-5)}$$

As we can see, the inertia tensor $\boldsymbol{J}_s'$ is a diagonal matrix. The diagonal elements of the inertia tensor $\boldsymbol{J}_s'$ and the coordinate axes $x_sy_sz_s$ are referred to the principal moments of inertia and the principal axes, respectively. Once the principal moments and their axes of the mover are known, the inertia tensor $\boldsymbol{J}_m$, with respect to any other axes passing through the center of mass, can be found by a similarity transformation defined by the Euler angles relating the two coordinates. If the transformation matrix is given as $\boldsymbol{R}$, the inertia tensor $\boldsymbol{J}_m'$ can be represented as follows:

$$\boldsymbol{J}_m'=\boldsymbol{R}\boldsymbol{J}_s'\boldsymbol{R}^T \quad \text{(6.2.1-6)}$$

The transformation matrix $\boldsymbol{R}$ from the stationary-coordinate axes $x_sy_sz_s$ to the mover-coordinate axes $x_my_mz_m$ shown in Fig. 6.2.1-1 is given as follows:

$$\boldsymbol{R}=\begin{bmatrix} \cos(\pi/4) & -\sin(\pi/4) & 0 \\ \sin(\pi/4) & \cos(\pi/4) & 0 \\ 0 & 0 & 1 \end{bmatrix} \quad \text{(6.2.1-7)}$$

Therefore, we can calculate the inertia tensor $\boldsymbol{J}_m'$ of the mover with respect to the mover-coordinate axes $x_my_mz_m$ as follows:

$$\boldsymbol{J}_m'=\begin{bmatrix} 0.1828 & 0 & 0 \\ 0 & 0.1828 & 0 \\ 0 & 0 & 0.3543 \end{bmatrix}\times 10^{-7} \ \text{kg·m}^2. \quad \text{(6.2.1-8)}$$

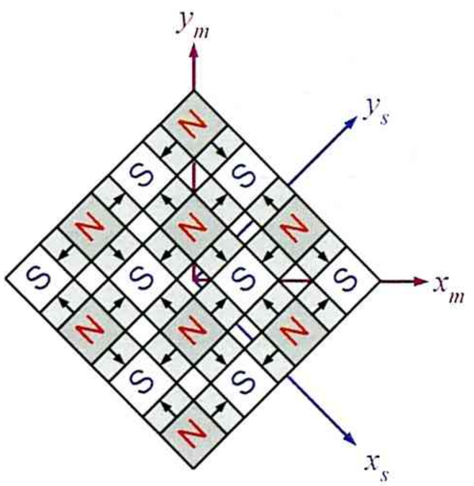

Fig. 6.2.1-1: Mover with mover-coordinate axes $x_m y_m z_m$ and stationary-coordinate axes $x_s y_s z_s$.

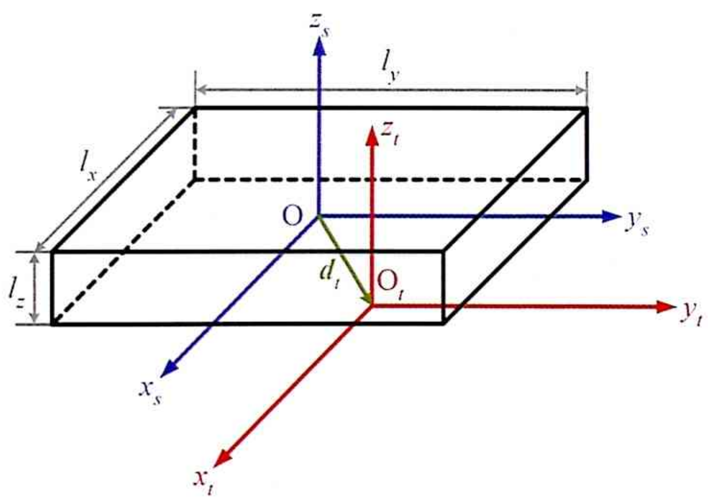

Fig. 6.2.1-2: Rectangular prism with two mutually-parallel coordinate axes.

6.2.2. Euler Angle and Angular Velocity

In order to define the 3-DOF rotational orientation of the mover, the Euler angle needs to be defined [Gol01, Taj06]. In this study, Euler angle $\boldsymbol{\phi} = [\alpha \quad \beta \quad \gamma]^T$ is defined from α, β and γ as orderly counterclockwise rotations around the stationary z_s–, y_s– and x_s–axes passing through the center of mass of the mover, respectively, as shown in Fig. 6.2.2-1. At first, an immediate coordinate $x_1y_1z_1$ is defined to be rotated from the stationary coordinate $x_sy_sz_s$ by α around the z_s–axis. Then, an immediate coordinate $x_2y_2z_2$ is defined to be rotated from the coordinate $x_1y_1z_1$ by β around the y_s–axis. Finally, the mover coordinate $x_my_mz_m$ is defined to be rotated from the coordinate $x_2y_2z_2$ by γ around the x_s–axis.

Next, the orientation of the mover coordinate $x_my_mz_m$ with respect to the stationary coordinate $x_sy_sz_s$, $\boldsymbol{R}_{sm}$, is introduced from the Euler angle $\boldsymbol{\phi}$. When a body is rotated counterclockwise by ψ around an arbitrary vector $\boldsymbol{\lambda} = [\lambda_1 \quad \lambda_2 \quad \lambda_3]^T$, the rotation matrix $\boldsymbol{R}_\psi$ can be represented as follows:

$$\boldsymbol{R}_\psi = \boldsymbol{E}\cos\psi + (\lambda_1\boldsymbol{M}_1 + \lambda_2\boldsymbol{M}_2 + \lambda_3\boldsymbol{M}_3)\sin\psi + \boldsymbol{\lambda\lambda}^T(1-\cos\psi) \quad \text{(6.2.2-1)}$$

where $\boldsymbol{E}$ is a 3×3 unit matrix and $\boldsymbol{M}_i$ (i = 1, 2 or 3) is an infinitesimal rotation generator, which can be represented by the following equations:

$$\boldsymbol{E} = \begin{bmatrix} 1 & 0 & 0 \\ 0 & 1 & 0 \\ 0 & 0 & 1 \end{bmatrix} \quad \text{(6.2.2-2)}$$

$$\boldsymbol{M}_1 = \begin{bmatrix} 0 & 0 & 0 \\ 0 & 0 & -1 \\ 0 & 1 & 0 \end{bmatrix}, \quad \boldsymbol{M}_2 = \begin{bmatrix} 0 & 0 & 1 \\ 0 & 0 & 0 \\ -1 & 0 & 0 \end{bmatrix}, \quad \boldsymbol{M}_3 = \begin{bmatrix} 0 & -1 & 0 \\ 1 & 0 & 0 \\ 0 & 0 & 0 \end{bmatrix} \quad \text{(6.2.2-3)}$$

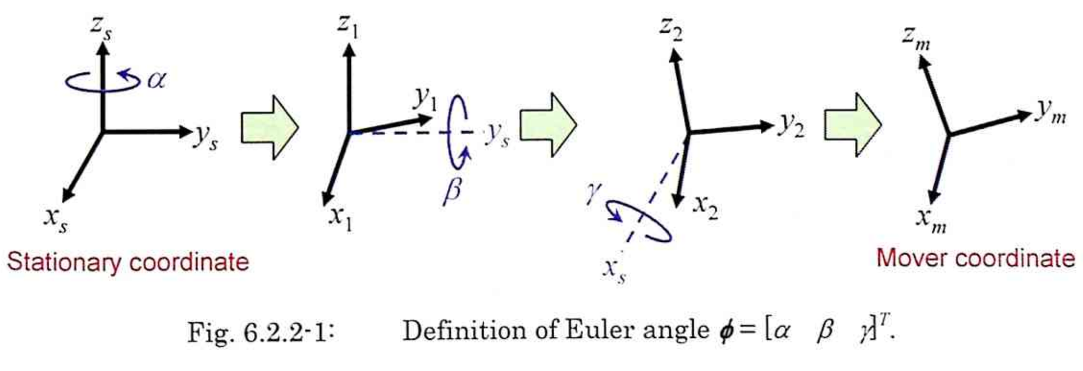

Fig. 6.2.2-1: Definition of Euler angle $\boldsymbol{\phi} = [\alpha \quad \beta \quad \gamma]^T$.

At first, a rotation matrix to rotate counterclockwise by α around the z_s–axis, $\boldsymbol{R}_{s1}$ can be calculated from Eqs. (6.2.2-1)–(6.2.2-3). Because the unit vector of the z_s–axis with respect to the stationary coordinate $x_s y_s z_s$ is represented as $\boldsymbol{\lambda}_{1s} = [0 \quad 0 \quad 1]^T$, the rotation matrix $\boldsymbol{R}_{s1}$ can be represented as follows:

$$\boldsymbol{R}_{s1} = \begin{bmatrix} \cos\alpha & -\sin\alpha & 0 \\ \sin\alpha & \cos\alpha & 0 \\ 0 & 0 & 1 \end{bmatrix} \qquad (6.2.2\text{-}4)$$

Then, the unit vector of the y_s–axis with respect to the coordinate $x_1 y_1 z_1$, $\boldsymbol{\lambda}_{2s}$ is represented as follows:

$$\boldsymbol{\lambda}_{2s} = \boldsymbol{R}_{s1}^{-1} \begin{bmatrix} 0 \\ 1 \\ 0 \end{bmatrix} = \begin{bmatrix} \sin\alpha \\ \cos\alpha \\ 0 \end{bmatrix}. \qquad (6.2.2\text{-}5)$$

Therefore, a rotation matrix to rotate counterclockwise by β around the y_s–axis, $\boldsymbol{R}_{12}$ can be calculated as follows:

$$\boldsymbol{R}_{12} = \begin{bmatrix} \cos\beta + \sin^2\alpha \cdot (1-\cos\beta) & \cos\alpha \cdot \sin\alpha \cdot (1-\cos\beta) & \cos\alpha \cdot \sin\beta \\ \cos\alpha \cdot \sin\alpha \cdot (1-\cos\beta) & \cos\beta + \cos^2\alpha \cdot (1-\cos\beta) & -\sin\alpha \cdot \sin\beta \\ -\cos\alpha \cdot \sin\beta & \sin\alpha \cdot \sin\beta & \cos\beta \end{bmatrix}. \qquad (6.2.2\text{-}6)$$

Finally, the unit vector of the x_s–axis with respect to the coordinate $x_2 y_2 z_2$, $\boldsymbol{\lambda}_{ms}$ is represented as follows:

$$\boldsymbol{\lambda}_{ms} = \boldsymbol{R}_{12}^{-1} \boldsymbol{R}_{s1}^{-1} \begin{bmatrix} 1 \\ 0 \\ 0 \end{bmatrix} = \begin{bmatrix} \cos\alpha \cdot \cos\beta \\ -\sin\alpha \cdot \cos\beta \\ \sin\beta \end{bmatrix}. \qquad (6.2.2\text{-}7)$$

Therefore, a rotation matrix to rotate counterclockwise by γ around the x_s–axis, $\boldsymbol{R}_{2m}$ can be calculated as follows:

$$\boldsymbol{R}_{2m} = [\boldsymbol{R}_{2m1} \quad \boldsymbol{R}_{2m2} \quad \boldsymbol{R}_{2m3}] \qquad (6.2.2\text{-}8)$$

$$\boldsymbol{R}_{2m1} = \begin{bmatrix} \cos\gamma + \cos^2\alpha \cdot \cos^2\beta \cdot (1-\cos\gamma) \\ \sin\beta \cdot \sin\gamma - \cos\alpha \cdot \sin\alpha \cdot \cos^2\beta \cdot (1-\cos\gamma) \\ \sin\alpha \cdot \cos\beta \cdot \sin\gamma + \cos\alpha \cdot \cos\beta \cdot \sin\beta \cdot (1-\cos\gamma) \end{bmatrix} \qquad (6.2.2\text{-}9)$$

$$\boldsymbol{R}_{2m2} = \begin{bmatrix} -\sin\beta \cdot \sin\gamma - \cos\alpha \cdot \sin\alpha \cdot \cos^2\beta \cdot (1-\cos\gamma) \\ \cos\gamma + \sin^2\alpha \cdot \cos^2\beta \cdot (1-\cos\gamma) \\ \cos\alpha \cdot \cos\beta \cdot \sin\gamma - \sin\alpha \cdot \cos\beta \cdot \sin\beta \cdot (1-\cos\gamma) \end{bmatrix} \qquad (6.2.2\text{-}10)$$

$$\boldsymbol{R}_{2m3} = \begin{bmatrix} -\sin\alpha \cdot \cos\beta \cdot \sin\gamma + \cos\alpha \cdot \cos\beta \cdot \sin\beta \cdot (1-\cos\gamma) \\ -\cos\alpha \cdot \cos\beta \cdot \sin\gamma - \sin\alpha \cdot \cos\beta \cdot \sin\beta \cdot (1-\cos\gamma) \\ \cos\gamma + \sin^2\beta \cdot (1-\cos\gamma) \end{bmatrix} \qquad (6.2.2\text{-}11)$$

The rotation matrix of the mover coordinate $x_m y_m z_m$ with respect to the stationary coordinate $x_s y_s z_s$, $\boldsymbol{R}_{sm}$, can be calculated from the rotation matrices $\boldsymbol{R}_{s1}$, $\boldsymbol{R}_{12}$, $\boldsymbol{R}_{2m}$ as follows:

$$R_{sm} = R_{s1}R_{12}R_{2m}$$
$$= \begin{bmatrix} \cos\alpha\cdot\cos\beta & -\sin\alpha\cdot\cos\beta & \sin\beta \\ \sin\alpha\cdot\cos\gamma+\cos\alpha\cdot\sin\beta\cdot\sin\gamma & \cos\alpha\cdot\cos\gamma-\sin\alpha\cdot\sin\beta\cdot\sin\gamma & -\cos\beta\cdot\sin\gamma \\ \sin\alpha\cdot\sin\gamma-\cos\alpha\cdot\sin\beta\cdot\cos\gamma & \cos\alpha\cdot\sin\gamma+\sin\alpha\cdot\sin\beta\cdot\cos\gamma & \cos\beta\cdot\cos\gamma \end{bmatrix}.$$

....................................(6.2.2-12)

The rotation matrix of the stationary coordinate $x_sy_sz_s$ with respect to the mover coordinate $x_my_mz_m$, R_{ms}, can be calculated as follows:

$$R_{ms} = R_{sm}^{-1} = R_{sm}^{T}$$
$$= \begin{bmatrix} \cos\alpha\cdot\cos\beta & \sin\alpha\cdot\cos\gamma+\cos\alpha\cdot\sin\beta\cdot\sin\gamma & \sin\alpha\cdot\sin\gamma-\cos\alpha\cdot\sin\beta\cdot\cos\gamma \\ -\sin\alpha\cdot\cos\beta & \cos\alpha\cdot\cos\gamma-\sin\alpha\cdot\sin\beta\cdot\sin\gamma & \cos\alpha\cdot\sin\gamma+\sin\alpha\cdot\sin\beta\cdot\cos\gamma \\ \sin\beta & -\cos\beta\cdot\sin\gamma & \cos\beta\cdot\cos\gamma \end{bmatrix}.$$

....................................(6.2.2-13)

We can convert positions with respect to the mover coordinate $x_my_mz_m$ into those with respect to the stationary coordinate $x_sy_sz_s$ as follows from Eq. (6.2.2-13).

The angular velocity of the mover with respect to the mover coordinate $x_my_mz_m$, as shown in Fig. 6.2.2-2, $\omega_{sm}' = [\omega_x' \quad \omega_y' \quad \omega_z']^T$ can be calculated as follows:

$$\omega_{sm}' = R_{2m}^{-1}R_{12}^{-1}\omega_{s1}' + R_{2m}^{-1}\omega_{12}' + \omega_{2m}'$$
$$= R_{\omega\phi}(\phi)\frac{d\phi}{dt} \qquad \text{..(6.2.2-14)}$$

$$R_{\omega\phi} = \begin{bmatrix} \sin\alpha\cdot\sin\gamma-\cos\alpha\cdot\sin\beta\cdot\cos\gamma & \sin\alpha\cdot\cos\gamma+\cos\alpha\cdot\sin\beta\cdot\sin\gamma & \cos\alpha\cdot\cos\beta \\ \cos\alpha\cdot\sin\gamma+\sin\alpha\cdot\sin\beta\cdot\cos\gamma & \cos\alpha\cdot\cos\gamma-\sin\alpha\cdot\sin\beta\cdot\sin\gamma & -\sin\alpha\cdot\cos\beta \\ \cos\beta\cdot\cos\gamma & -\cos\beta\cdot\sin\gamma & \sin\beta \end{bmatrix}.$$

....................................(6.2.2-15)

where ω_{s1}', ω_{12}', and ω_{2m}' are angular velocities of the mover about the z_s–axis with respect to the immediate coordinate $x_1y_1z_1$, the y_s–axis with respect to the immediate coordinate $x_2y_2z_2$, and the x_s–axis with respect to the mover coordinate $x_my_mz_m$, respectively. The angular velocities ω_{s1}', ω_{12}', and ω_{2m}' can be calculated from the unit vectors λ_{1s}, λ_{2s}, λ_{ms} and Euler angle $\phi = [\alpha \quad \beta \quad \gamma]^T$ as follows:

$$\omega_{s1}' = \lambda_{1s}\frac{d\alpha}{dt}, \quad \omega_{12}' = \lambda_{2s}\frac{d\beta}{dt}, \quad \omega_{2m}' = \lambda_{ms}\frac{d\gamma}{dt}. \qquad \text{...(6.2.2-16)}$$

Then, we can calculate the differential of the Euler angle ($d\phi/dt$) from Eqs. (6.2.2-14) and (6.2.2-15) as follows:

$$\frac{d\phi}{dt} = R_{\omega\phi}(\phi)^{-1}\omega_{sm}' \qquad \text{...(6.2.2-17)}$$

$$
\boldsymbol{R}_{\phi\omega}{}^{-1} = \frac{1}{\cos(2\alpha)} \times \begin{bmatrix} \sin\alpha\cdot\sin\gamma - \cos\alpha\cdot\sin\beta\cdot\cos\gamma & \cos\alpha\cdot\sin\gamma + \sin\alpha\cdot\sin\beta\cdot\cos\gamma & \cos\beta\cdot\cos\gamma \\ \sin\alpha\cdot\cos\gamma + \cos\alpha\cdot\sin\beta\cdot\sin\gamma & \cos\alpha\cdot\cos\gamma - \sin\alpha\cdot\sin\beta\cdot\sin\gamma & -\cos\beta\cdot\sin\gamma \\ \cos\alpha\cdot\cos\beta & -\sin\alpha\cdot\cos\beta & \sin\beta \end{bmatrix}.
$$

....................................(6.2.2-18)

Equation (6.2.2-18) indicates that the matrix $\boldsymbol{R}_{\omega\phi}{}^{-1}$ cannot be defined, and therefore the Euler angle $\boldsymbol{\phi}$ cannot be uniquely determined from this equation when the Euler angle α = ±45, or ±135 deg. The orientation of the mover is often called a "singular posture." However, in this study, it is assumed that the mover is driven in the range within the Euler angle $\alpha \approx 0$ deg. Therefore, a singular posture cannot occur, and the differential of the Euler angle ($d\boldsymbol{\phi} / dt$) can be calculated from Eqs. (6.2.2-17) and (6.2.2-18).

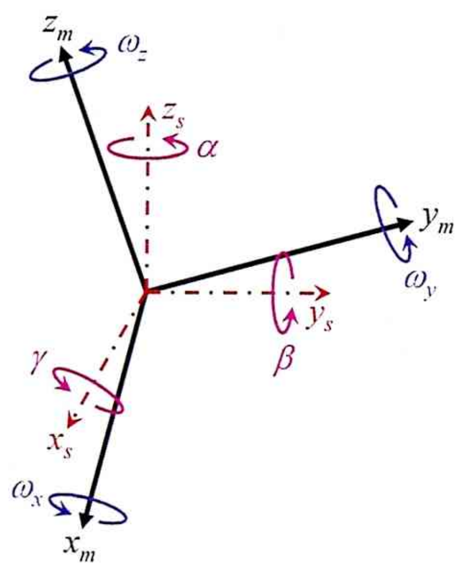

Fig. 6.2.2-2: Angular velocity $\boldsymbol{\omega}_{sm}' = [\omega_x \quad \omega_y \quad \omega_z]^T$ and Euler angle $\boldsymbol{\phi} = [\alpha \quad \beta \quad \gamma]^T$.

6.2.3. Equation of Motion

The equation of the motion of the mover can be represented by the translational forces acting on the mover $F_{sm} = [F_x \quad F_y \quad F_z]^T$ and torques around the mover center O' $T_{sm}' = [T_x' \quad T_y' \quad T_z']^T$ as follows:

$$M\frac{d\boldsymbol{v}_{sm}}{dt} = \boldsymbol{F}_{sm} + \boldsymbol{F}_g \quad \text{(6.2.3-1)}$$

$$\boldsymbol{J}_m'\frac{d\boldsymbol{\omega}_{sm}'}{dt} = \boldsymbol{T}_{sm}' - \boldsymbol{\omega}_{sm}' \times \left(\boldsymbol{J}_m' \boldsymbol{\omega}_{sm}'\right) \quad \text{(6.2.3-2)}$$

where $\boldsymbol{v}_{sm} = [v_x \quad v_y \quad v_z]^T$ and $\boldsymbol{F}_g = [0 \quad 0 \quad -Mg]^T$ are velocity of the mover and the force of gravity acting on the mover, respectively.

Equations (6.2.3-1) and (6.2.3-2) represent 3-DOF translational and rotational motion equations of the mover, respectively. All variables in the translational and rotational motion equations are represented with respect to the stationary coordinate $x_s y_s z_s$ and mover coordinate $x_m y_m z_m$, respectively. The position $\boldsymbol{r}_{sm}$ and Euler angle $\boldsymbol{\phi}$ of the mover can be represented by the velocity $\boldsymbol{v}_{sm}$ and angular velocity $\boldsymbol{\omega}_{sm}'$, respectively, as follows:

$$\frac{d\boldsymbol{r}_{sm}}{dt} = \boldsymbol{v}_{sm} \quad \text{(6.2.3-3)}$$

$$\frac{d\boldsymbol{\phi}}{dt} = \boldsymbol{R}_{\omega\phi}(\boldsymbol{\phi})^{-1}\, \boldsymbol{\omega}_{sm}'. \quad \text{(6.2.3-4)}$$

Equations (6.2.3-1)–(6.2.3-4) can represent dynamic behaviors of the mover with 6 DOF.

6.3. Planar Motion Control with Stable Magnetic Levitation

This section discusses six-current controls to stably levitate the mover and actively control the x–, y–, z–, and α–motions. There are two important things for the motion controls:

- to generate independent translational forces F_x, F_y, and F_z with stable torques in the γ– and β–directions.
- to generate torques in the α–direction with less interference to translational forces F_x, F_y, and F_z.

This section first presents driving forces resulting from three pairs of two-phase armature currents, and then the driving force-control system.

6.3.1. Translational Motion Control

In this study, three pairs of two-phase currents $\boldsymbol{i}_j = [I_{1j} \quad I_{2j}]^T$ ($j = x$, y, or α), as shown in Fig. 6.3.1-1, are assumed to be supplied to the three pairs of two-phase armature conductors as shown in the following equations:

$$I_{1j} = -I_j \cos(\theta_{sj}) \quad \text{(6.3.1-1)}$$

$$I_{2j} = I_j \sin(\theta_{sj}) \quad \text{(6.3.1-2)}$$

Figure 6.3.1-2 shows phasor diagrams for the relation between the dq–frame and $\alpha'\beta'$–frame. The currents I_{1x} and I_{1y} generate the opposite-phase magnetic field to that resulting from the permanent-magnet mover when the mover position in the x– and y–directions $(x, y) = (x_s, y_s)$ and the Euler angle $\boldsymbol{\phi} = (0, 0, 0)$. The α'–axis are aligned to the opposite side of the current I_{1j} axis, and the β'–axis leads the α'–axis by 90 deg. The current $I_{1\alpha}$ generates a magnetic field that is tilted by $\varphi = -24.7$ deg around the α–direction from that caused by current I_{1x}. Bearing this in mind, the armature currents in the dq–frame I_{dj} and I_{qj} can be represented by the currents I_{1j} and I_{2j} as follows:

$$\begin{bmatrix} I_{dx} \\ I_{qx} \end{bmatrix} = \begin{bmatrix} \cos(\pi x_s/\tau) & -\sin(\pi x_s/\tau) \\ \sin(\pi x_s/\tau) & \cos(\pi x_s/\tau) \end{bmatrix} \begin{bmatrix} I_{2x} \\ I_{1x} \end{bmatrix} \quad \text{(6.3.1-3)}$$

$$\begin{bmatrix} I_{dy} \\ I_{qy} \end{bmatrix} = \begin{bmatrix} \cos(\pi y_s/\tau) & -\sin(\pi y_s/\tau) \\ \sin(\pi y_s/\tau) & \cos(\pi y_s/\tau) \end{bmatrix} \begin{bmatrix} I_{2y} \\ I_{1y} \end{bmatrix} \quad \text{(6.3.1-4)}$$

$$\begin{bmatrix} I_{d\alpha} \\ I_{q\alpha} \end{bmatrix} = \begin{bmatrix} \cos(\pi \alpha_s/\tau) & -\sin(\pi \alpha_s/\tau) \\ \sin(\pi \alpha_s/\tau) & \cos(\pi \alpha_s/\tau) \end{bmatrix} \begin{bmatrix} I_{2\alpha} \\ I_{1\alpha} \end{bmatrix} \quad \text{(6.3.1-5)}$$

$$\alpha_s = x_s \cos\varphi - y_s \sin\varphi\,. \quad \text{(6.3.1-6)}$$

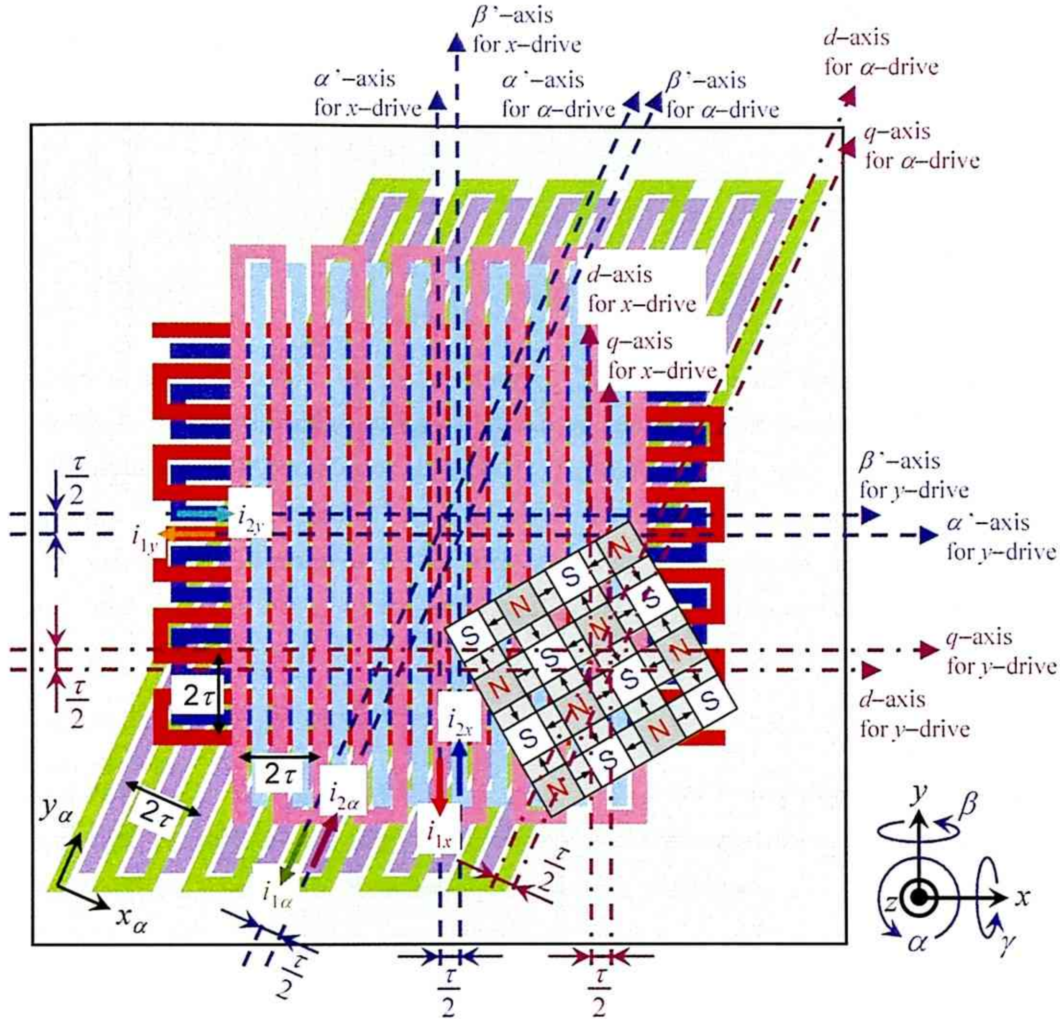

Fig. 6.3.1-1: *dq*–frame and $\alpha'\beta'$–frame for the *x*–, *y*–, and α–directional drives.

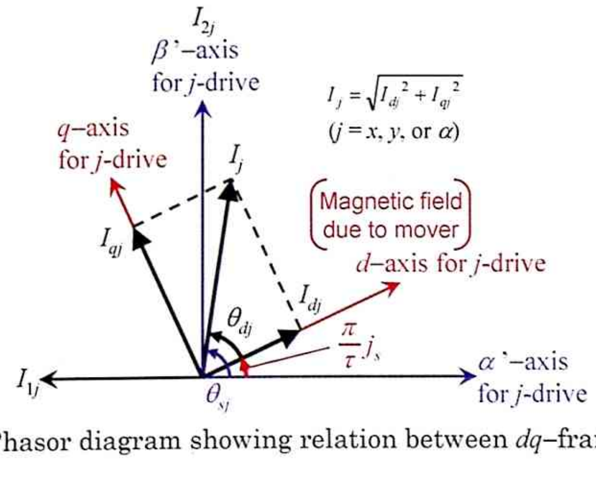

Fig. 6.3.1-2: Phasor diagram showing relation between *dq*–frame and $\alpha'\beta'$–frame.

These pairs of d– and q–axis currents generate the translational forces $\boldsymbol{F}_{sm}$ and torques $\boldsymbol{T}_{sm}'$ as follows:

$$\begin{bmatrix} F_x \\ F_y \\ F_z \\ T_x' \\ T_y' \\ T_z' \end{bmatrix} = \begin{bmatrix} \boldsymbol{K}(\boldsymbol{r}_{sm}, \boldsymbol{\phi}) \\ 6 \times 6 \text{ matrix} \end{bmatrix} \begin{bmatrix} I_{dx} \\ I_{qx} \\ I_{dy} \\ I_{qy} \\ I_{d\alpha} \\ I_{q\alpha} \end{bmatrix} \quad \cdots\cdots (6.3.1\text{-}7)$$

where $\boldsymbol{K}$ is a 6 × 6 matrix, and all elements of $\boldsymbol{K}$ depend on the mover position $\boldsymbol{r}_{sm}$ and Euler angle $\boldsymbol{\phi}$. Where Euler angle $\boldsymbol{\phi} \approx \boldsymbol{0}$, $\boldsymbol{K}$ can be approximated as shown in Fig. 6.3.1-3, and therefore 3-DOF translational forces F_x, F_y, and F_z can be independently controlled by two-phase currents $\boldsymbol{i}_x$ and $\boldsymbol{i}_y$.

In this study, references of the translational forces $F_{sm}^* = [F_x^* \quad F_y^* \quad F_z^*]^T$ are determined from the mover positions $\boldsymbol{r}_{sm} = [x \quad y \quad z]^T$ and position references $\boldsymbol{r}_{sm}^* = [x^* \quad y^* \quad z^*]^T$ by three PID controls.

$$\boldsymbol{F}_{sm}^* = \boldsymbol{P}_F\left(\boldsymbol{r}_{sm}^* - \boldsymbol{r}_{sm}\right) - \boldsymbol{D}_F \frac{d\boldsymbol{r}_{sm}}{dt} \quad \cdots\cdots (6.3.1\text{-}8)$$

where $\boldsymbol{P}_F = [P_{Fx} \quad P_{Fy} \quad P_{Fz}]$ and $\boldsymbol{D}_F = [D_{Fx} \quad D_{Fy} \quad D_{Fz}]$ are proportional and differential parameters, respectively. In this study, references of the armature currents $\boldsymbol{i}_x^*$ and $\boldsymbol{i}_y^*$ are calculated from those of the translational forces $\boldsymbol{F}_{sm}^*$ as follows:

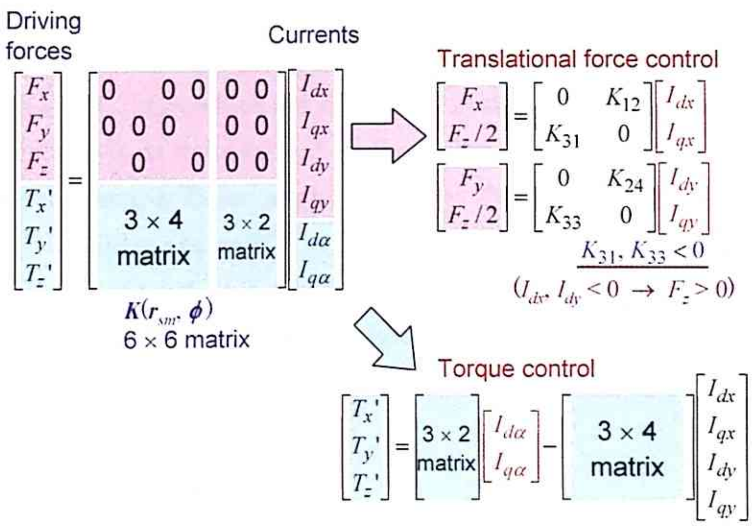

Fig. 6.3.1-3: Control method for driving forces.

$$\begin{bmatrix} I_{dx}^{*} \\ I_{qx}^{*} \end{bmatrix} = \begin{bmatrix} K_{11} & K_{12} \\ K_{31} & K_{32} \end{bmatrix}^{-1} \begin{bmatrix} F_x^{*} \\ F_z^{*}/2 \end{bmatrix} \quad \cdots\cdots (6.3.1\text{-}9)$$

$$\begin{bmatrix} I_{dy}^{*} \\ I_{qy}^{*} \end{bmatrix} = \begin{bmatrix} K_{23} & K_{24} \\ K_{33} & K_{34} \end{bmatrix}^{-1} \begin{bmatrix} F_y^{*} \\ F_z^{*}/2 \end{bmatrix} \quad \cdots\cdots (6.3.1\text{-}10)$$

Supplying the armature currents $\boldsymbol{i_x}$ and $\boldsymbol{i_y}$ equal to the references $\boldsymbol{i_x}^*$ and $\boldsymbol{i_y}^*$ generates the translational forces $\boldsymbol{F_{sm}}$ equal to the references $\boldsymbol{F_{sm}}^*$.

6.3.2. Torque Characteristics and Rotational Motion Control

The armature currents $\boldsymbol{i_x}$ and $\boldsymbol{i_y}$ generate not only the translational forces $\boldsymbol{F_{sm}}$, but also the torques $\boldsymbol{T_{sm}}'$. Therefore, it is extremely important to investigate how the torques $\boldsymbol{T_{sm}}'$ resulting from the armature currents $\boldsymbol{i_x}$ and $\boldsymbol{i_y}$ influence the rotational motions of the mover. When the Euler angle $\boldsymbol{\phi} \approx \mathbf{0}$, the torques T_z', T_y', and T_x' are dominant on the Euler angle α, β, and γ, respectively. Next I performed a numerical analysis of the torque characteristics due to the armature currents for the x–directional drive when rotational motions with more than 2 DOF occur in the range within -2 deg < α, β, and γ < 2 deg.

Figure 6.3.2-1 shows the system constants K_{61} $(= T_z' / I_{dx})$ and K_{62} $(= T_z' / I_{qx})$, which are dominant on the α–motion, for the Euler angle α. The system constant K_{61} is independent on the Euler angles β and γ, and the system constant K_{62} is almost independent on the Euler angles α and β. Figure 6.3.2-2 shows the system constants K_{51} $(= T_y' / I_{dx})$ and K_{52} $(= T_y' / I_{qx})$, which are dominant on the β–motion, for the Euler angle β. The system constant K_{51} is independent on the Euler angle γ, and the differential $(\partial K_{51} / \partial \beta)$ is independent on the Euler angles α and γ. The system constant K_{52} is almost independent on the Euler angles α, β, and γ. Figure 6.3.2-3 shows the system constants K_{41} $(= T_x' / I_{dx})$ and K_{42} $(= T_x' / I_{qx})$, which are dominant on the γ–motion, for the Euler angle γ. The system constant K_{41} is independent on the Euler angles α and β, and the system constant K_{42} is almost independent on the Euler angles β and γ.

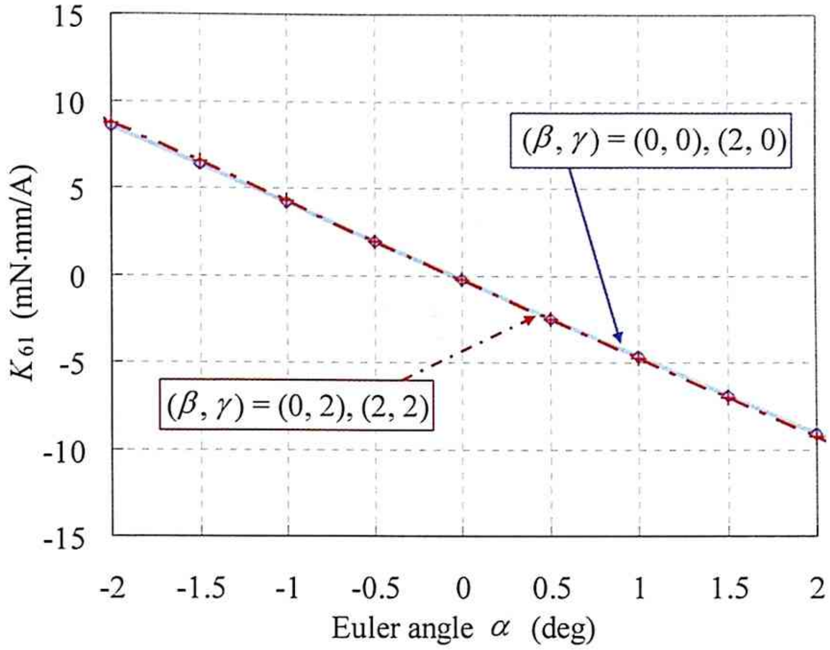

(a) K_{61} (= T_z' / I_{dx}) at (β, γ) = (0, 0), (2, 0), (0, 2), and (2, 2).

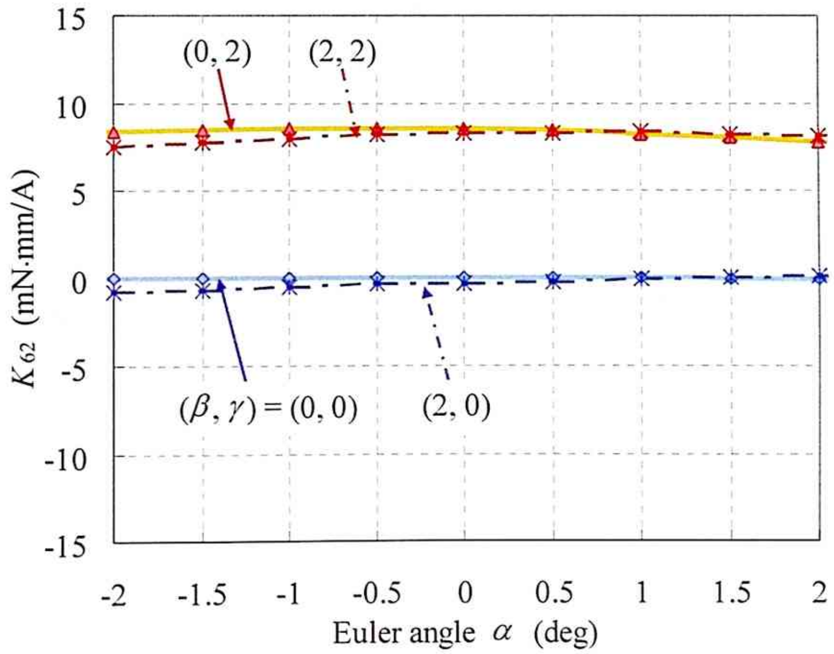

(b) K_{62} (= T_z' / I_{qx}) at (β, γ) = (0, 0), (2, 0), (0, 2), and (2, 2).

Fig. 6.3.2-1: Analysis result of torque T_z' due to the armature currents for the x–directional drive for the Euler angle α.

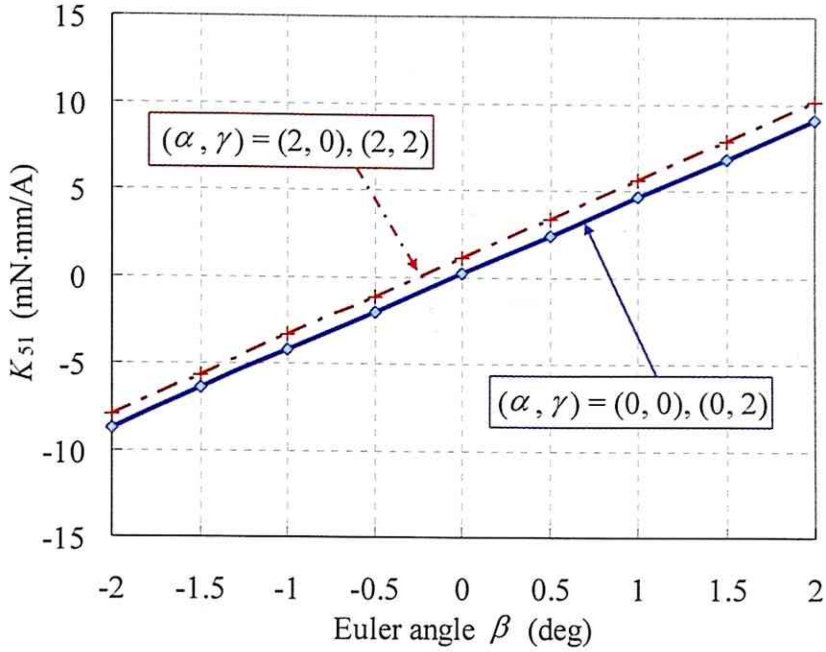

(a) K_{51} (= T_y' / I_{dx}) at (α, γ) = (0, 0), (2, 0), (0, 2), and (2, 2).

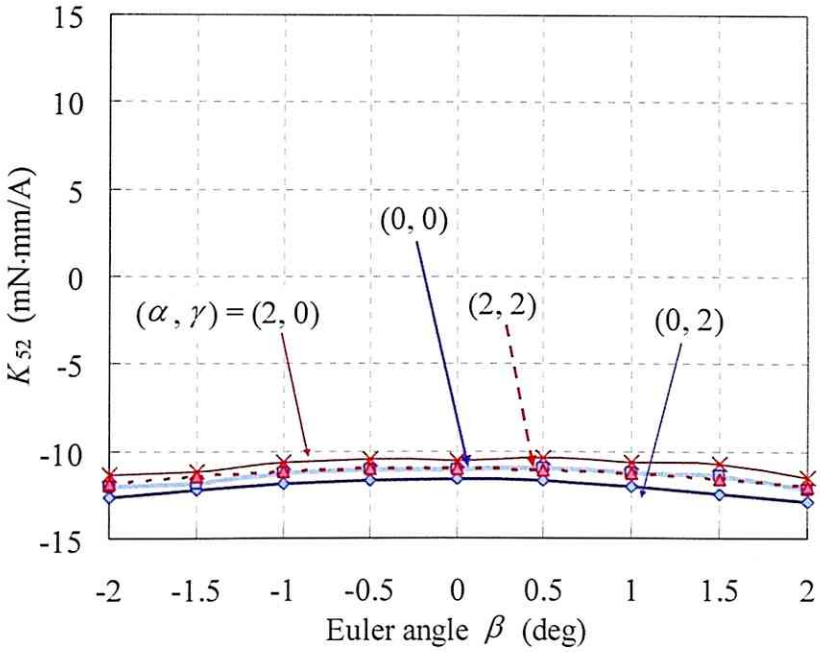

(b) K_{52} (= T_y' / I_{qx}) at (α, γ) = (0, 0), (2, 0), (0, 2), and (2, 2).

Fig. 6.3.2-2: Analysis result of torque T_y' due to the armature currents for the x–directional drive for the Euler angle β.

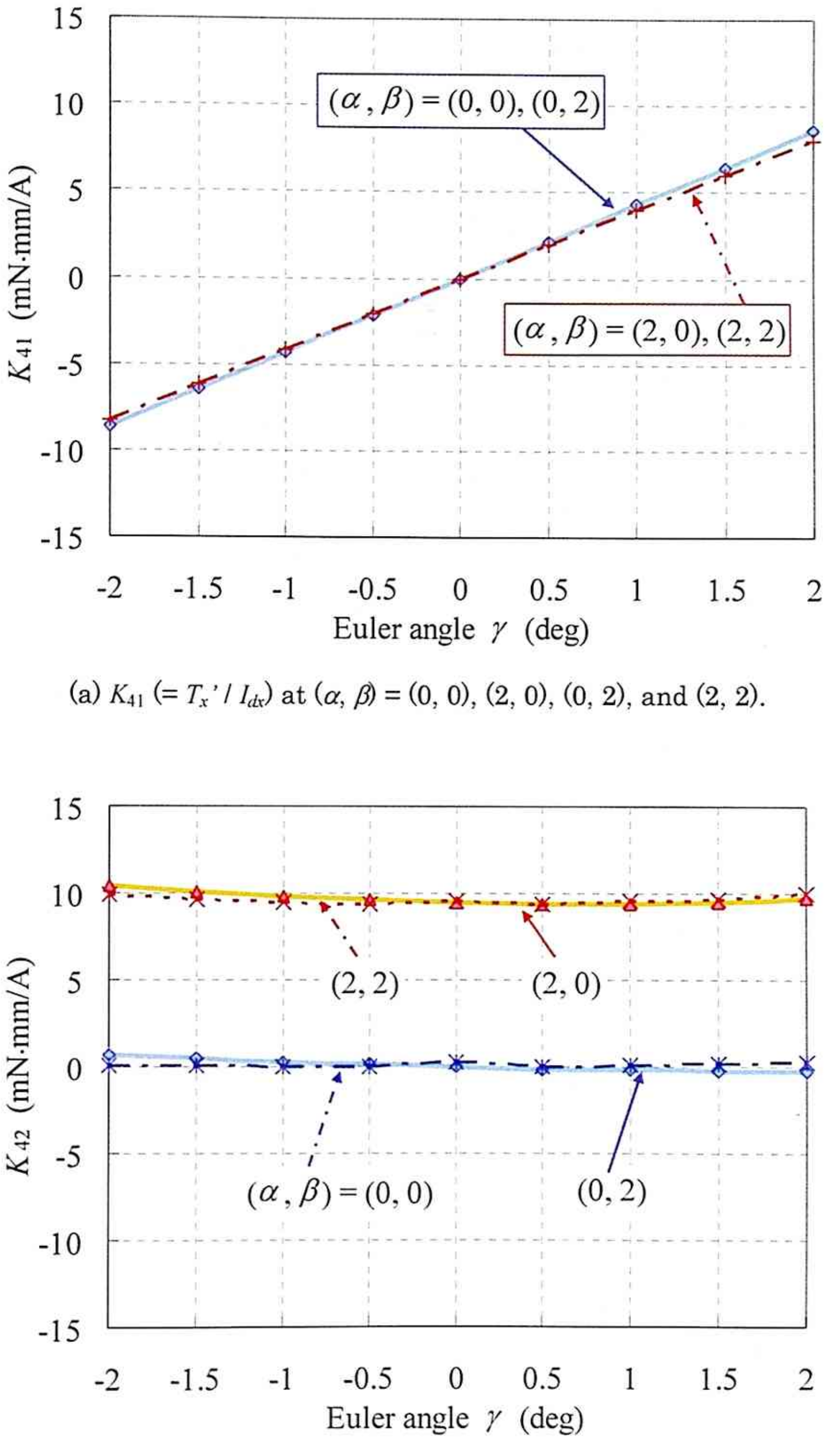

(a) K_{41} (= T_x' / I_{dx}) at (α, β) = (0, 0), (2, 0), (0, 2), and (2, 2).

(b) K_{42} (= T_x' / I_{qx}) at (α, β) = (0, 0), (2, 0), (0, 2), and (2, 2).

Fig. 6.3.2-3: Analysis result of torque T_x' due to the armature currents for the x–directional drive for the Euler angle γ.

From these results, when rotational motions with more than 2 DOF occur, $\boldsymbol{K}$ is almost in agreement with K_{FT} in Eq. (6.1.2-3). Therefore, negative d–axis currents I_{dx}, I_{dy} that control the suspension forces F_z generate stable restoring torques T_y', T_x'. However, the q–axis currents that control the translational forces F_x, F_y generate torques T_z', T_y', T_x', which are not stable restoring torques. So next I performed a numerical analysis of the torque characteristics due to the armature currents for the α–directional drive.

Figure 6.3.2-4 shows the torques due to the armature conductors for the α–directional drive at $(\beta, \gamma) = (0, 0)$. When the Euler angles $(\beta, \gamma) = (0, 0)$, the d–axis current $I_{d\alpha}$ generates only the torque T_z' and the q–axis current $I_{q\alpha}$ generates only the torques T_y', T_x'. Therefore, the torques T_y' and T_x' cannot be independently controlled by the armature currents for the α–directional drive.

Figure 6.3.2-5 shows the torques from the armature conductors for the α–directional drive at $(\beta, \gamma) = (2, 2)$. The d– and q–axis currents generates T_z', T_y', T_x', but the torque T_y' is much less than the torques T_z' and T_x'. Therefore in this study, the torques T_z' and T_x' are controlled by the two armature currents for the α–directional drive. When the Euler angle $\boldsymbol{\phi} \approx \mathbf{0}$ and angular velocity $\boldsymbol{\omega}_{ms}' \approx \mathbf{0}$, a linearized equation of the rotational motion can be obtained from Eqs. (6.2.3-2) and (6.2.3-4) as follows:

$$\begin{aligned}\frac{d^2\boldsymbol{\phi}}{dt^2} &= \boldsymbol{R}_{\omega\phi}\left((\boldsymbol{J}_m')^{-1}\left(\boldsymbol{T}_{sm}' - \boldsymbol{\omega}_{sm}' \times (\boldsymbol{J}_m'\boldsymbol{\omega}_{sm}')\right) - \frac{d\boldsymbol{R}_{\omega\phi}^{-1}}{dt}\frac{d\boldsymbol{\phi}}{dt} \right) \\ &\approx \boldsymbol{R}_{\omega\phi}(\boldsymbol{J}_m')^{-1}\boldsymbol{T}_{sm}' = \boldsymbol{T}_E = \begin{bmatrix} T_\alpha & T_\beta & T_\gamma \end{bmatrix}^T\end{aligned} \quad \text{......(6.3.2-1)}$$

In this study, $\boldsymbol{T}_E^*$, which is the reference of $\boldsymbol{T}_E$, is determined by a PD control from the Euler angle α and the reference α^* as follows:

$$T_\alpha^* = P_{T\alpha}(\alpha^* - \alpha) - D_{T\alpha}\frac{d\alpha}{dt} \quad \text{......(6.3.2-2)}$$

where $P_{T\alpha}$ and $D_{T\alpha}$ are proportional and differential parameters, respectively. Then, the references T_β^* and T_γ^* are determined to be zero because of the suppression of the β– and γ–motions. The torque references $T_x'^*$ and $T_z'^*$ can be calculated from the reference $\boldsymbol{T}_E^*$ by Eq. (6.3.2-1). Then, the references of the armature currents for the α–directional drive $I_{d\alpha}^*$ and $I_{q\alpha}^*$ can be calculated for the torque references $T_x'^*$ and $T_z'^*$ as follows:

$$\begin{bmatrix} I_{d\alpha}^* \\ I_{q\alpha}^* \end{bmatrix} = \begin{bmatrix} K_{45} & K_{46} \\ K_{65} & K_{66} \end{bmatrix}^{-1}\left(\begin{bmatrix} T_x'^* \\ T_z'^* \end{bmatrix} - \begin{bmatrix} T_{xa}' \\ T_{za}' \end{bmatrix} \right) \quad \text{......(6.3.2-3)}$$

where T_{xa}' and T_{za}' are torques due to the armature currents $\boldsymbol{i}_x$ and $\boldsymbol{i}_y$, and can be represented as follows:

$$\begin{bmatrix} T_{xa} \\ T_{za} \end{bmatrix} = \begin{bmatrix} K_{41} & K_{42} & K_{43} & K_{44} \\ K_{61} & K_{62} & K_{63} & K_{64} \end{bmatrix} \begin{bmatrix} I_{dx} \\ I_{qx} \\ I_{dy} \\ I_{qy} \end{bmatrix} \quad \text{(6.3.2-4)}$$

Supplying the armature currents $\boldsymbol{i}_\alpha$ equal to the references $\boldsymbol{i}_\alpha^*$ generates $\boldsymbol{T}_E$ nearly equal to $\boldsymbol{T}_E^*$, and controls the rotational motions with less interference to the translational motions.

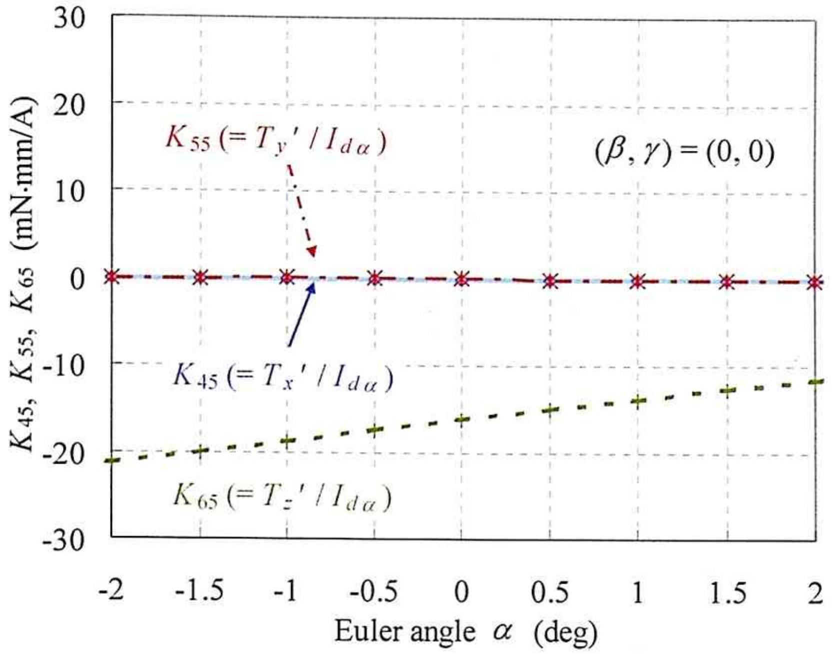

(a) K_{45} (= $T_x' / I_{d\alpha}$), K_{55} (= $T_y' / I_{d\alpha}$), and K_{65} (= $T_z' / I_{d\alpha}$) at (β, γ) = (0, 0).

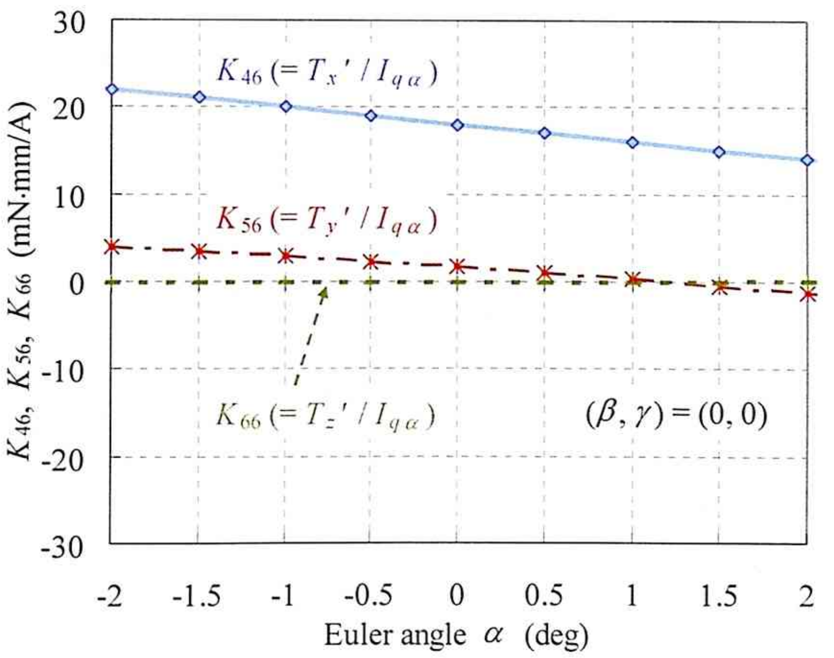

(b) K_{46} (= $T_x' / I_{q\alpha}$), K_{56} (= $T_y' / I_{q\alpha}$), and K_{66} (= $T_z' / I_{q\alpha}$) at (β, γ) = (0, 0).

Fig. 6.3.2-4: Analysis result of the torques from the armature conductors for the α–directional drive for the Euler angle α at (β, γ) = (0, 0).

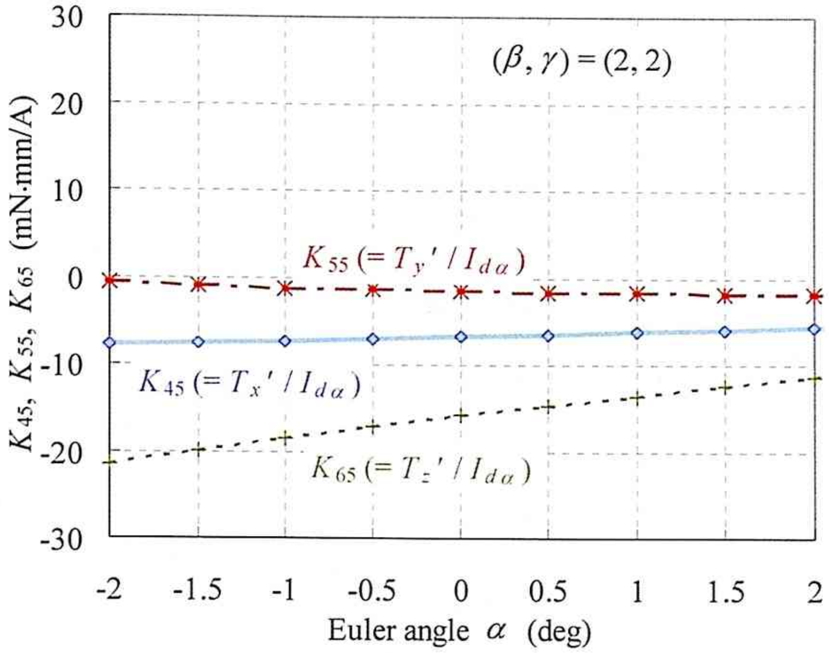

(a) K_{45} (= T_x' / $I_{d\alpha}$), K_{55} (= T_y' / $I_{d\alpha}$), and K_{65} (= T_z' / $I_{d\alpha}$) at (β, γ) = (2, 2).

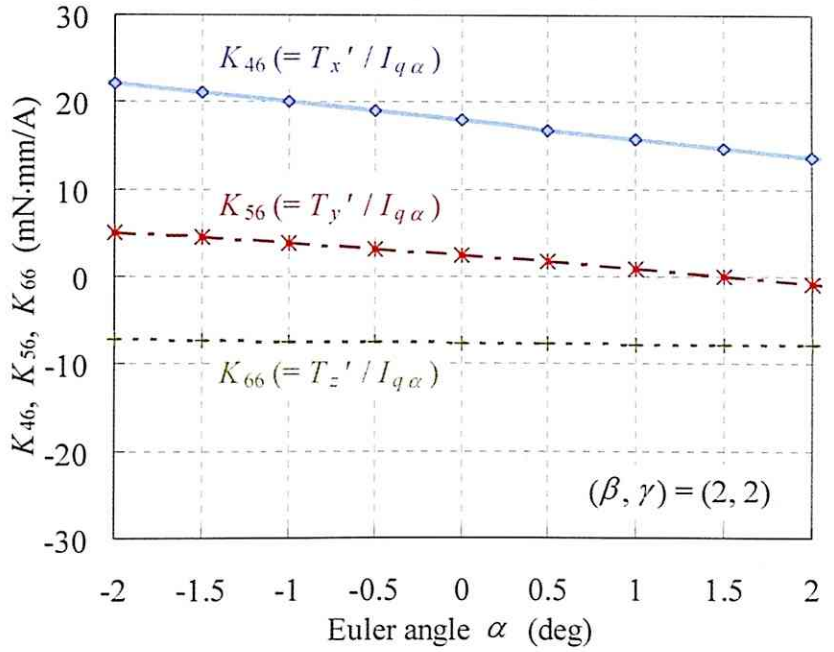

(b) K_{46} (= T_x' / $I_{q\alpha}$), K_{56} (= T_y' / $I_{q\alpha}$), and K_{66} (= T_z' / $I_{q\alpha}$) at (β, γ) = (2, 2).

Fig. 6.3.2-5: Analysis result of the torques from the armature conductors for the α–directional drive for the Euler angle α at (β, γ) = (2, 2).

6.4. Numerical Analysis of Mover Motion

This section presents the analytical conditions of the 6-DOF motions of the mover and the analysis results.

6.4.1. Analytical Model and Conditions

Motion characteristics with 6 DOF can be obtained by solving Eqs. (6.2.3-1)–(6.2.3-4) using the Runge-Kutta method. In order to numerically solve the equations, it is necessary to calculate the driving forces $\boldsymbol{F}_{sm}$ and $\boldsymbol{T}_{sm}'$ at each time step. The calculation at each time step consists of an integration of Lorentz force acting on the line segments as shown in Eqs. (3.3.1-3) and (3.3.1-4), and so requires a lot of computation time. The flux density $\boldsymbol{B}$ acting on the armature conductors greatly depends on the mover position $\boldsymbol{r}_{sm}$ and Euler angle $\boldsymbol{\phi}$. Therefore, the driving forces $\boldsymbol{F}_{sm}$ and $\boldsymbol{T}_{sm}'$ are functions of the mover position $\boldsymbol{r}_{sm}$ and Euler angle $\boldsymbol{\phi}$. In this study, the system-constant matrix $\boldsymbol{K}$ was calculated and the data table of $\boldsymbol{K}$ was made before the motion analysis. Then, the system-constant matrix $\boldsymbol{K}$ is calculated from the mover position $\boldsymbol{r}_{sm}$ and Euler angle $\boldsymbol{\phi}$ by interpolating it with the data table at each time step. Figure 6.4.1-1 shows a flow chart of the motion analysis. The analysis conditions are shown as follows:

- time step $dt = 0.2$ ms
- control period $t_c = 2$ ms
- initial position $\boldsymbol{r}_i = \boldsymbol{0}$
- initial Euler angle $\boldsymbol{\phi}_i = \boldsymbol{0}$.

When the z–position is zero, the mover is assumed to be on the stator. The proportional and differential parameters are determined so that the settling times in the x–, y–, z–, and α–motions are less than 1 s. In this analysis, to investigate the planar motion control and magnetic levitation, the following two position references are given:

(I) Magnetic suspension at specific positions:

In this analysis, the position references are given as follows: the mover position $\boldsymbol{r}_{sm}^* = [0 \quad 0 \quad 0.15]^T$ and Euler angle $\alpha^* = 0$ deg. Therefore, the large q–axis currents I_{qx} and I_{qy} to generate the translational forces F_x and F_y are unnecessary. In this condition, the magnetic levitation of the mover is easy to be stabilized because there are small torques

T_y' and T_x', which are not restoring torques.

(II) Planar motion control with magnetic suspension:

In this analysis, in order to verify the compatibility of both the 3-DOF planar motion control and magnetic suspension, the position references are given as follows:

- $x^* = 2\cos(\pi t)$ mm
- $y^* = 2\sin(\pi t)$ mm
- $z^* = 0.15$ mm
- Euler angle $\alpha^* = 0$ deg.

In this analysis, the q–axis currents I_{qx} and I_{qy} used to generate the translational forces F_x and F_y influence the magnetic suspension characteristics, and this influence was investigated.

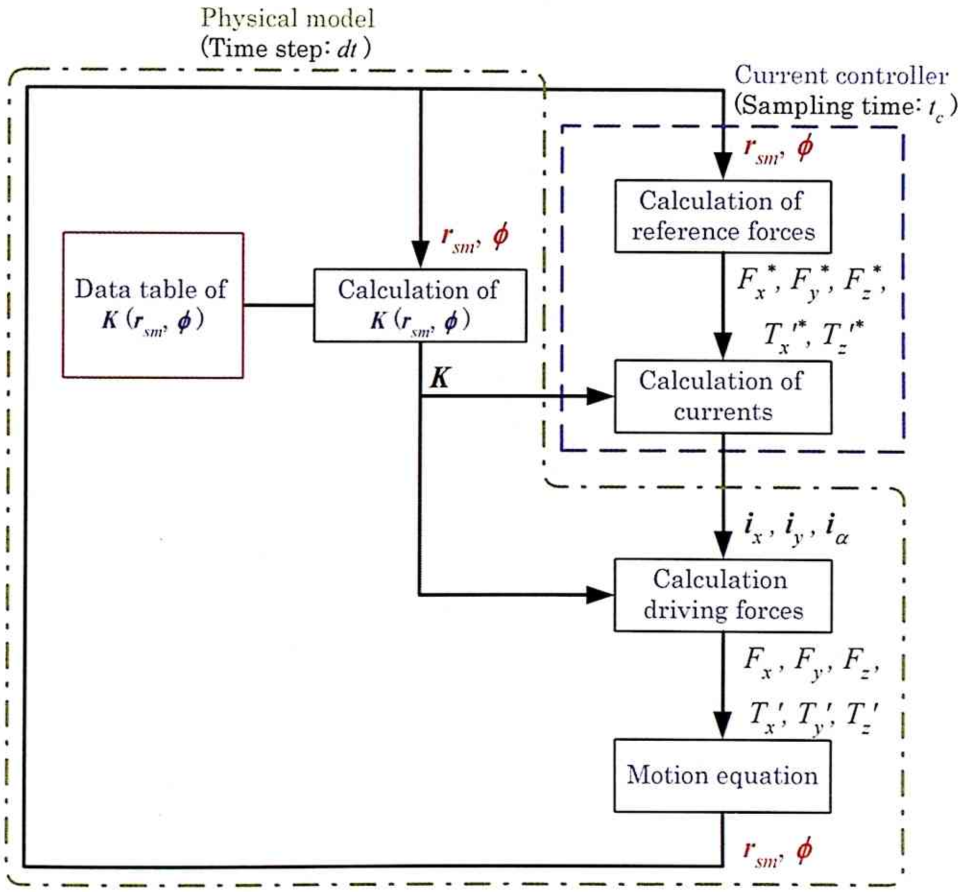

Figure 6.4.1-1: Flow chart of 6-DOF motion analysis.

6.4.2. Numerical Analysis Results

Numerical analysis of the mover motions under the previously mentioned conditions (I) and (II) in Subsection 6.4.1 were performed. These analysis results are shown as follows under each of the above conditions:

(I) Magnetic suspension at specific positions:

Figure 6.4.2-1 shows the analysis result of the mover motions under analysis condition (I). Figure 6.4.2-1 indicates that the mover can be positioned at these reference positions in the x–, y–, z–, and α–directions with less suppressed β– and γ–displacements. Therefore, the mover can be magnetically suspended with stability.

Figure 6.4.2-2 shows the analysis result of the armature currents under analysis condition (I). The d–axis currents I_{dx} and I_{dy} used to generate the suspension forces are absolutely less than 0.36 A and 0.45 A, respectively. The q–axis currents I_{qx} and I_{qy} used to generate the translational forces F_x and F_y are absolutely less than 3 mA, therefore, high-resolution current controls are necessary to control the mover motions. The armature currents for the α–directional drive are absolutely less than 0.04 A.

(II) Planar motion control with magnetic suspension:

Figure 6.4.2-3 shows the analysis result of the mover motions under analysis condition (II). Figure 6.4.2-3 indicates that the mover can track the reference positions in the x– and y–directions, and be positioned in the z– and α–directions with suppression of the β– and γ–displacements. Therefore, mover motions can be controlled with stable magnetic levitation.

Figure 6.4.2-4 shows the analysis result of the armature currents under analysis condition (II). The q–axis currents I_{qx} and I_{qy} are absolutely less than 7 mA, but slightly larger than those in analysis (I). The q–axis currents I_{qx} and I_{qy} used to control the translational forces F_x and F_y also generate simultaneously the torques T_y' and T_x', respectively. Therefore, displacement of the Euler angles β and γ under analysis condition (II) is larger than that in analysis condition (I) due to the greater q–axis currents I_{qx} and I_{qy} for the planar motions.

Therefore, I proposed a planar actuator with a magnetically levitated mover capable of large planar motions over the stator, and demonstrated both 3-DOF planar motion and magnetic levitation controls by applying three pairs (minimum number) of two-phase armature currents control by numerical analysis of the 6-DOF motion.

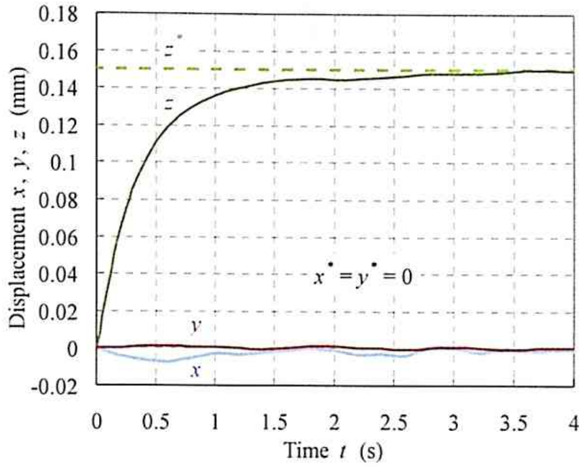

(a) Translational motions x, y, z.

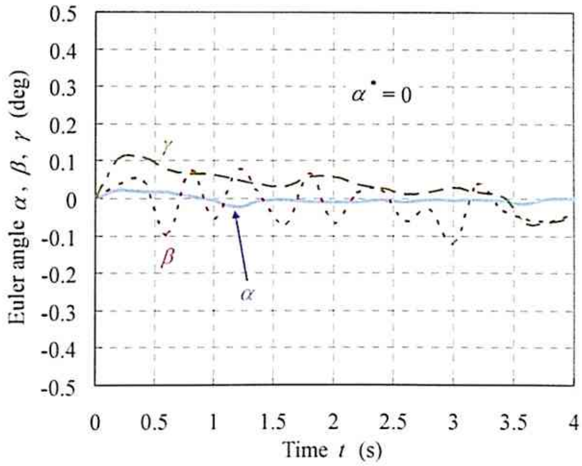

(b) Rotational motions α, β, γ.

Fig. 6.4.2-1: Analytically-obtained mover motions under analysis condition (I).

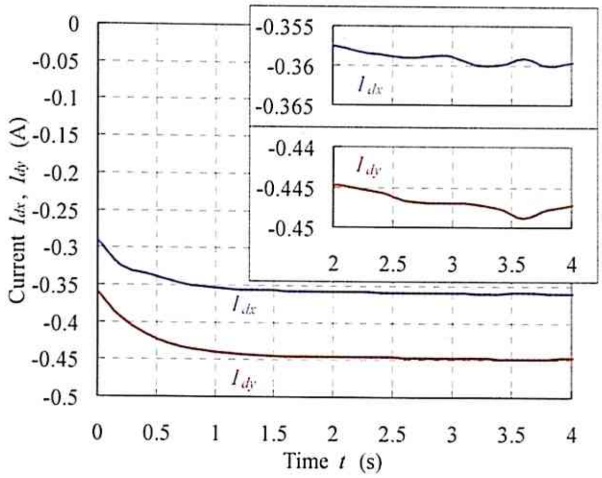

(a) d–axis currents I_{dx} and I_{dy} used to generate suspension forces F_z.

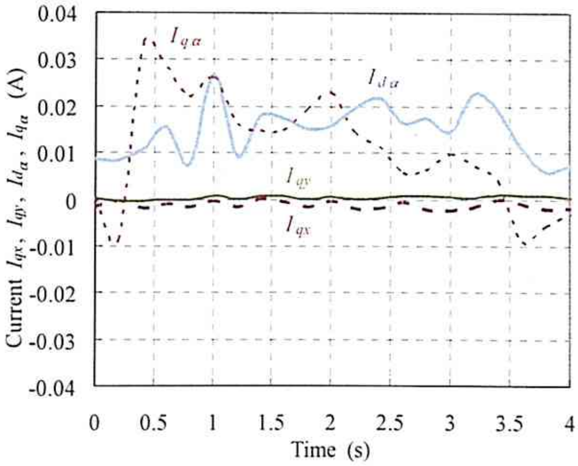

(b) d– and q–axis currents I_{qx}, I_{qy}, $I_{d\alpha}$, and $I_{q\alpha}$ used to control planar motions.

Fig. 6.4.2-2: Analytically-obtained armature currents under analysis condition (I).

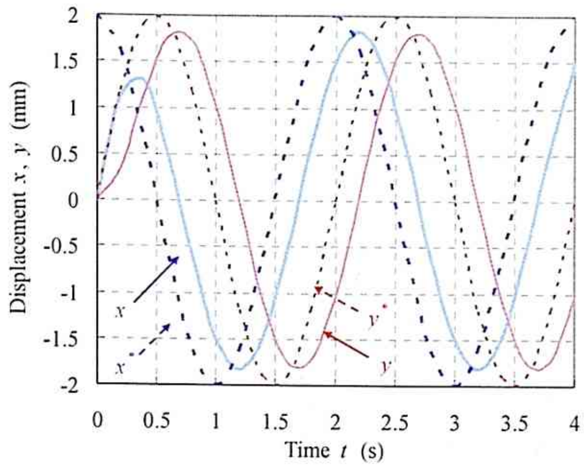

(a) Planar motions x, y.

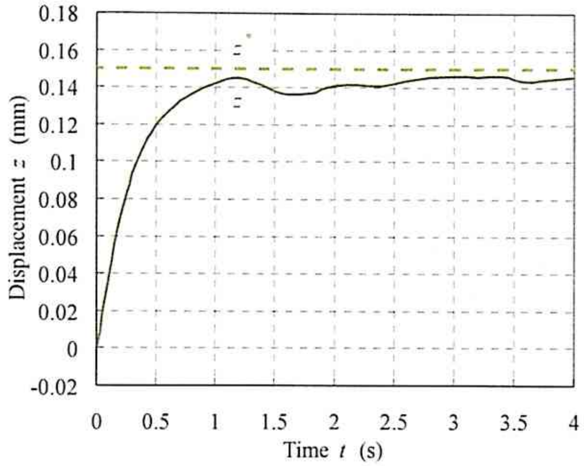

(b) Vertical motion z.

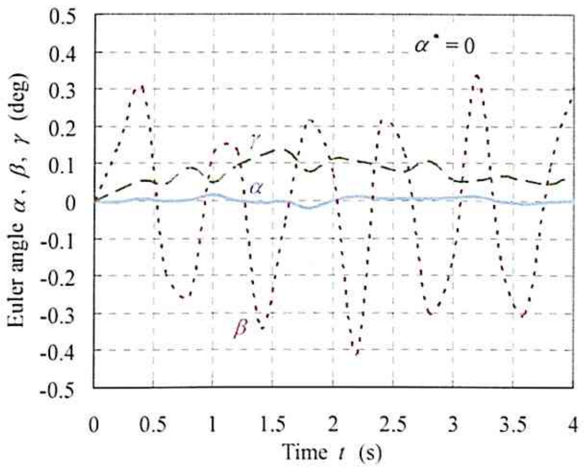

(c) Rotational motions α, β, γ.

Fig. 6.4.2-3: Analytically-obtained mover motions under analysis condition (II).

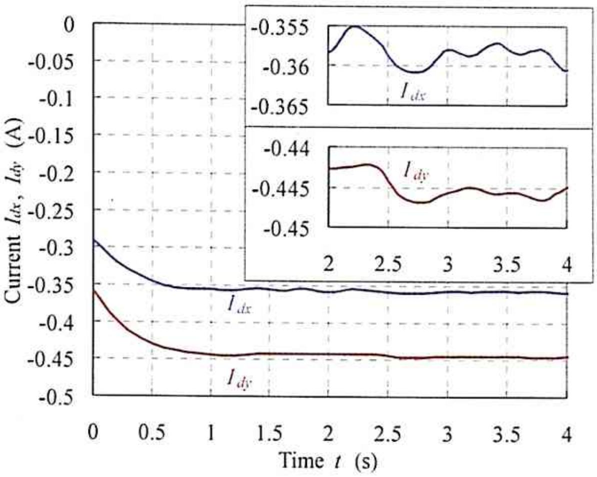

(a) d–axis currents I_{dx} and I_{dy} used to generate the suspension forces F_z.

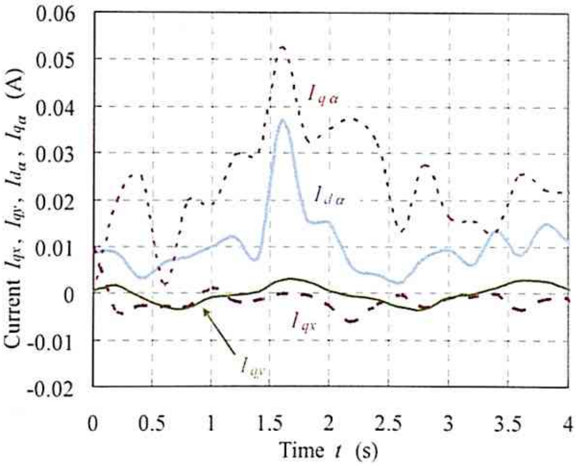

(b) d– and q–axis currents I_{qx}, I_{qy}, $I_{d\alpha}$, and $I_{q\alpha}$ used to control planar motions.

Fig. 6.4.2-4: Analytically-obtained armature currents under analysis condition (II).

6.5. Summary of Chapter 6

This chapter presents a feasibility verification of a planar actuator with both 3-DOF planar motions and magnetic suspension of the mover in order to further improve performance. Then, based on a numerical analysis of the 6-DOF driving forces, a planar actuator having a mover positioned above a plane and magnetically levitated by only six currents and the six-current-control algorithm were conceptually designed. Furthermore, I validated the designed planar actuator by numerical analysis of the 6-DOF motions. The results obtained in this thesis indicate the possibility of the realization of a high-performance MDOF planar actuator:

- decoupled 3-DOF motion control and magnetic levitation on a plane.
- wide movable area by a small number (six) of armature conductors.
- extendible movable area regardless of the number of armature conductors.
- small millimeter-sized mover.
- no problematic wiring to adversely affect drive performance.

As the next step, it is necessary to design an experimental system for the verification of the 6-DOF motion characteristics and conduct experimental tests.

Chapter 7

Conclusions

This chapter concludes this thesis and suggests future work.

7. Conclusions

This chapter presents the accomplishments and technical contributions of this thesis as conclusions, and also makes suggestions for future work.

7.1. Conclusions

In this study, I designed planar actuators that have a small mover capable of traveling over a wide movable area on a plane, and which is driven by a small number of armature conductors. These planar actuators form spatially superimposed magnetic circuits for the MDOF motion controls. Magnetic circuits are the most innovative of all planar actuators and enable the extensions of the movable area regardless of the number of armature conductors. However, there is a disadvantage to magnetic circuits that needs to be solved, which is that realizing decoupled controls among the driving forces in each degree of freedom is difficult. The most important assertion and technical contribution of this thesis is the design of the planar actuators so as to achieve independently control more-degree-of-freedom mover motions by using spatially superimposed magnetic circuits.

Chapter 1 presented an introduction to and applications for MDOF drive systems. Multiple moving-part actuators, consisting of multiple 1-DOF actuators, have been most utilized in MDOF drive systems. However, there are several disadvantages with multiple moving-part actuators that make it difficult to improve the accuracy and response of the mover drive. In order to solve these disadvantages, single moving-part actuators, capable of direct drive with MDOF, have been studied. Chapter 1 then introduced important element technologies, including magnetic materials and circuits, position sensing, and suspension and guide mechanisms. With this in mind, the purpose and technical contributions of this study were detailed. Finally, the structure of this thesis was outlined.

Chapter 2 presented classification of MDOF drive systems and remarks about their features and technical issues. MDOF drive systems can be classified by the number of moving parts, form of driving forces, and drive principle. Synchronous planar actuators, with which this study deals, have especially good controllability of the driving forces in planar actuators. With these technical details in mind, I then summarized the specifications of synchronous planar actuators that had been developed. In synchronous planar actuators, planar actuators with a permanent-magnet mover realize sophisticated motion controls, but have insufficiently wide movable area unless the planar actuators have a large number of armature conductors. The planar actuator that I proposed in this study is aimed at achieving compatibility of both sophisticated motion controls and a wide movable area using just a small number of armature conductors. In Chapter 2, I clarified the orientation of my proposed planar actuator in relation to previous planar actuators.

Chapter 3 presented the fundamental conceptual design of my proposed planar actuator, which aims to resolve the technical issues of previous planar actuators. The drive principle of the planar actuator is based on two-orthogonal linear-synchronous motors. The planar actuator form spatially superimposed magnetic circuits corresponding to the magnetic circuits of the two-orthogonal linear-synchronous motors. There are two polyphase armature conductors, and exciting these armature conductors generates two-directional multipole magnetic field over the stators. Therefore, increasing the length of all the armature conductors easily expands the movable area. Based on the numerical analysis results of the driving forces, I designed a decoupled control algorithm for 2-DOF translational and 1-DOF rotational motions.

Chapter 4 presented a design for an experimental system for an investigation into the drive characteristics of the planar actuator. I implemented a control algorithm into a DSP connected to AD/DA converter boards, and designed a 3-DOF position-sensing system using three laser-displacement sensors, as well as a suspension mechanism for the mover using ball bearings. Then, specifications of these experimental apparatuses were presented.

Chapter 5 presented an experimental verification of the 3-DOF motion controls of the mover on a plane, and the results of the experiment. From these experimental results, I successfully demonstrated that 3-DOF motions could be independently controlled by two pairs of three-phase currents. The movable area in the translational motions can be infinitely extended, and the rotational motions is in the range within the yaw angle = ±26 deg. Furthermore, the driving forces are periodic with a 90-deg period in the yaw direction, and the mover can travel in multiple 90-deg steps in the yaw direction. Therefore, the planar actuator has a wider movable area than previous planar actuators, although it only has two polyphase armature conductors.

Chapter 6 presented a feasibility verification of the magnetic suspension of a mover capable of 3-DOF planar motions in order to eliminate friction forces between the mover and ball bearings, aimed at incremental improvement of the drive performance. Based on a numerical analysis of the 6-DOF driving forces, I designed a planar actuator that has spatially superimposed magnetic circuits formed by only six currents and a permanent-magnet mover, so that the mover motions could be independently controlled in the 3-DOF translations and 1-DOF rotations above a plane. The drive characteristics were validated by a numerical analysis of the 6-DOF motions.

This thesis demonstrated the following significant accomplishments of a novel study:

- experimental verification of the design and control of a long-stroke 3-DOF planar actuator.
- numerical verification of design and control of a planar actuator with a stably and magnetically levitated mover capable of 3-DOF planar motions.

7.2. Future Work

This section discusses future works aimed at incremental improvements in the performance of the planar actuator as follows:

- Improvements to the drive system:
  - realization of decoupled 6-DOF motion controls by redesigning the mover or stator structure.
  - improvements to the specifications of the controller boards (input/output range resolution, sampling time, and so on), that would improve drive characteristics such as positioning precision and response.
  - investigation of a movable area out of plane.
  - consideration of payloads mounted on the mover.

- Improvements to the position-sensing system;
  - realization of 6-DOF position-sensing system, preferably integrated with the mover or stator.
  - calibration of sensor signals against the experimental environment such as temperature and thermal expansion.

In conclusion, this thesis presents high-performance MDOF planar actuators with a permanent-magnet mover capable of traveling over a wide movable area on a plane, with just a small number of stationary armature conductors. The combination of the mover and stator can generate spatially superimposed magnetic fields for the MDOF drive, and therefore increasing the length of the armature conductors can easily expand the movable area regardless of the number of armature conductors. A planar actuator was conceptually designed and fabricated. The fabricated planar actuator can independently control the 3-DOF motions of the mover. Furthermore, in order to eliminate deterioration of the drive characteristics due to friction forces, the planar actuator was redesigned so that the mover could be stably levitated and the 3-DOF motions on a plane could be controlled. Then, the mover motion characteristics were successfully verified by means of a numerical analysis. Next, a small fabrication size was realized by integrating the permanent-magnet array and armature conductors for the MDOF drive. The planar actuator has the first millimeter-sized mover and would provide a significant starting point when used with small electromechanical components in an MDOF drive.

Appendices

A. Fabrication of the Smallest Halbach Permanent-Magnet Mover

B. Structure of Manufactured Printed Circuit Board

C. 6-DOF Position Sensing Utilizing Laser-Displacement Sensors

A. Fabrication of the Smallest Halbach Permanent-Magnet Mover

In this study, I fabricated the smallest 2-D Halbach permanent-magnet array, which measure just 11 mm × 11 mm × 2 mm. The permanent-magnet array consists of one group of 16 permanent magnets and one of 24 permanent magnets, which measure 2 mm × 2 mm × 2 mm, and 2 mm × 2 mm × 1 mm, respectively. Mr. Koji Miyata and Mr. Yuji Doi, Shin-Etsu Chemical Co., Ltd. kindly provided these permanent magnets for this study. In the Halbach permanent-magnet array, adjacent permanent magnets are mutually subjected to repulsion forces. Therefore, I fabricated the permanent-magnet array by bonding the permanent magnets using these excellent adhesives; Araldite standard (Epoxy adhesive) and LOCTITE 326 LVUV (Ultraviolet cure adhesive) combined with LOCTITE 7649 (Primer).

First, I fabricated the permanent-magnet array on a 2-mm iron plate, mounting a square-ruler-shaped 1.2-mm iron plate in order to fix the permanent magnets using the iron plate during bonding between the permanent magnets. For the bond between the permanent magnets, I used LOCTITE, which bonds quickly (less than one minute), and has a relatively high shear strength (18.5 N/mm^2), bonding only the lateral sides of the permanent magnets. So in other words, I fabricated a Halbach permanent-magnet array using only LOCTITE. However, the adhesive strength was not high enough, and the bonded permanent-magnet array often became unglued when the electromagnetic forces for the MDOF drive acted upon the permanent-magnet array.

Next, in order to strengthen the adhesion, I coated the Halbach permanent-magnet array, bonded with LOCTITE, with Araldite, which bonds slowly (more than 12 hours) but has greater shear strength. Araldite is viscous, and keeping a flat coating using Araldite is difficult. So, after the Araldite hardened completely, I removed the unwanted Araldite using sandpaper to flatten the surface of the permanent-magnet array.

Figure A-1 shows the fabrication procedure for the smallest 2-D Halbach permanent-magnet array.

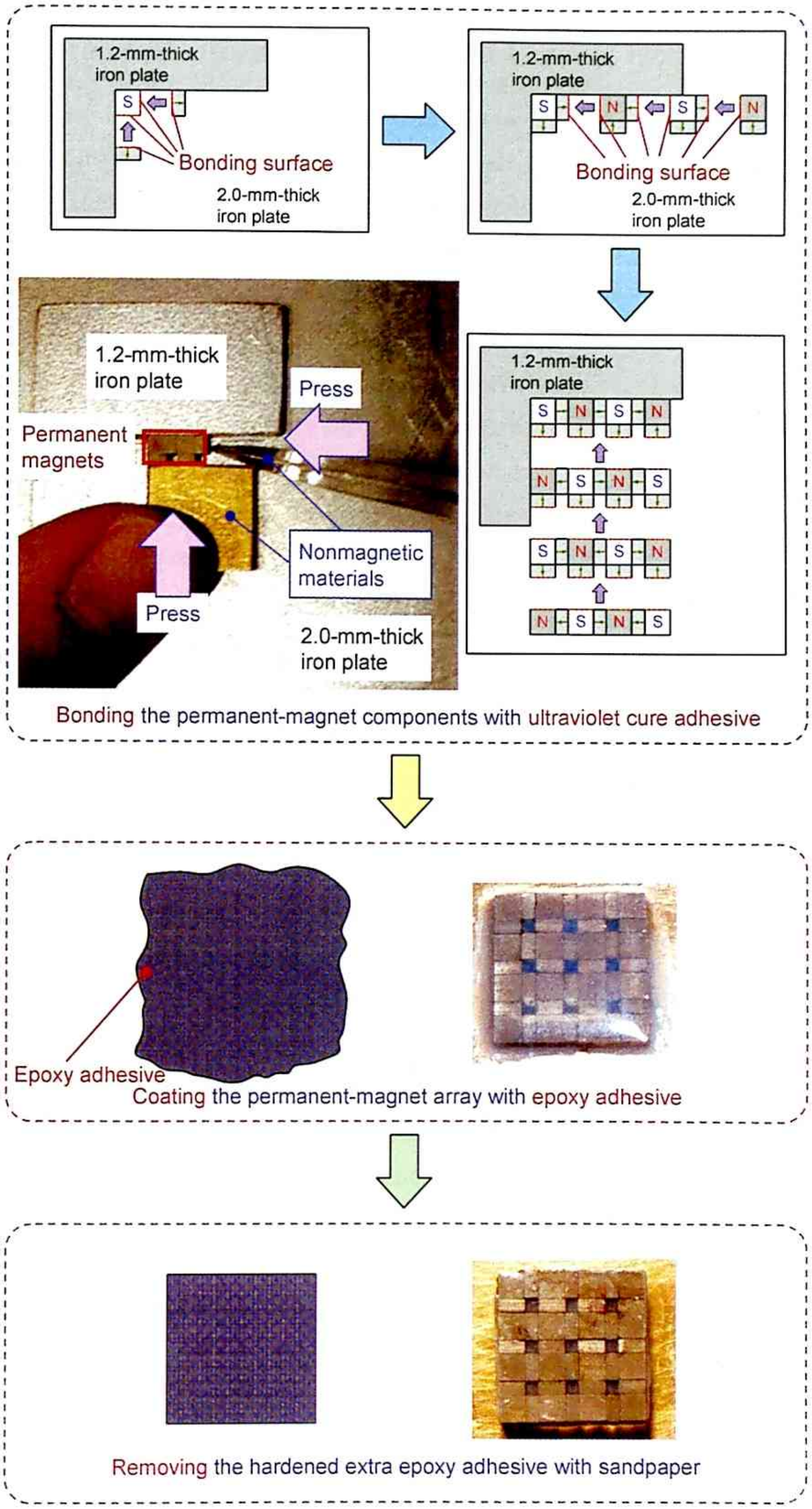

Fig. A-1: Fabrication procedure for the smallest 2-D Halbach permanent-magnet array.

B. Structure of Manufactured Printed Circuit Board

As mentioned in Chapter 3, in the experiments on 3-DOF motion control on a plane, a double-layered printed circuit board was utilized in order to generate a multipole magnetic field that has arbitrary amplitude and phase in the x– and y–directions. The printed circuit board consists of two 35-μm-thick conductor layers and a 100-μm-thick insulating layer sandwiched between the two conductor layers. In each conductor layer, 0.8-mm-wide strips of copper film are aligned at 1.76-mm (corresponding to one-third of the pitch length of the 3-DOF planar actuator) intervals. Three-phase conductors for the x– and y–directional drives are then formed by inserting the external circuits shown by dashed lines in Fig. B-1. The figure shows how exciting two pairs of three-phase conductors generates a multipole magnetic field above the centered 90 mm × 90 mm area of the printed circuit board. The intervals between the strips of copper film near the end of each strip are longer than those near the center in order to secure areas wide enough to solder, and 2.5-mm-diameter lands are aligned at 3.5-mm intervals. Figure B-2 shows the manufactured double-layered printed circuit board.

In Chapter 6, a triple-layered printed circuit board was designed in order to generate a multipole magnetic field that has arbitrary amplitude and phase in the x–, y–, and x_α–directions shown in Fig. 6.3.1-1. A cross-section view of the triple-layered printed circuit board is shown in Fig. B-3. The total thickness of the printed circuit board is 0.425 mm. The first, second, and third conductor layers have two-phase armature conductors for the x–, y–, and α–directional drives as shown in Figs. B-4, B-5, and B-6, respectively. The first and third conductor layers consist of 18-μm-thick copper film and 12-μm-thick through-hole plating, and the second conductor layer consists of 35-μm-thick copper film. The width of all the conductors is 0.8 mm. In the printed circuit board, there are a lot of 0.3-mm-diameter through holes, including 12-μm-thick through-hole plating in order to form mutually insulated three pairs of two-phase printed circuits. There are 15-μm-thick solder-resist layers and 5-mm-diameter lands with 1.4-mm-diameter through holes on the top and bottom surfaces. Figure B-7 shows the manufactured triple-layered printed circuit board.

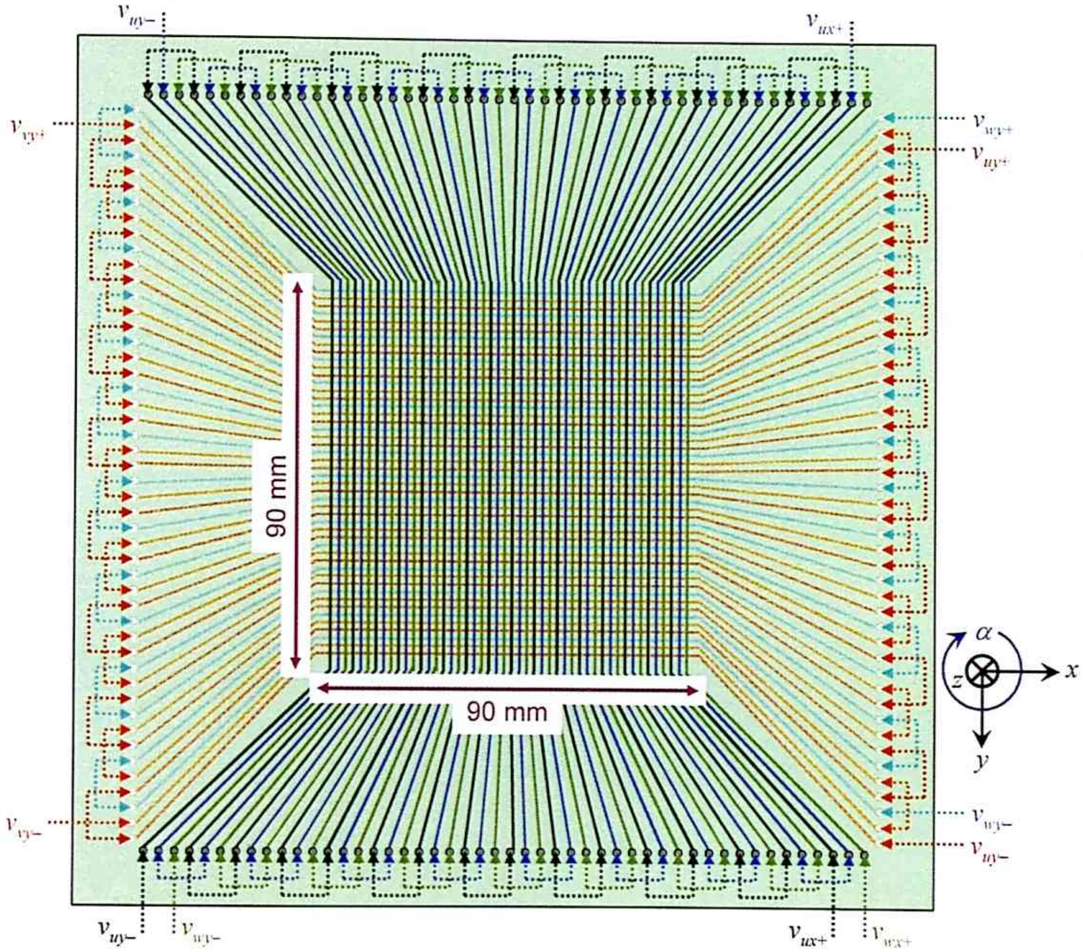

Fig. B-1: Structure of the double-layered printed circuit board. The solid lines represent the copper film and the dashed lines represent external circuits.

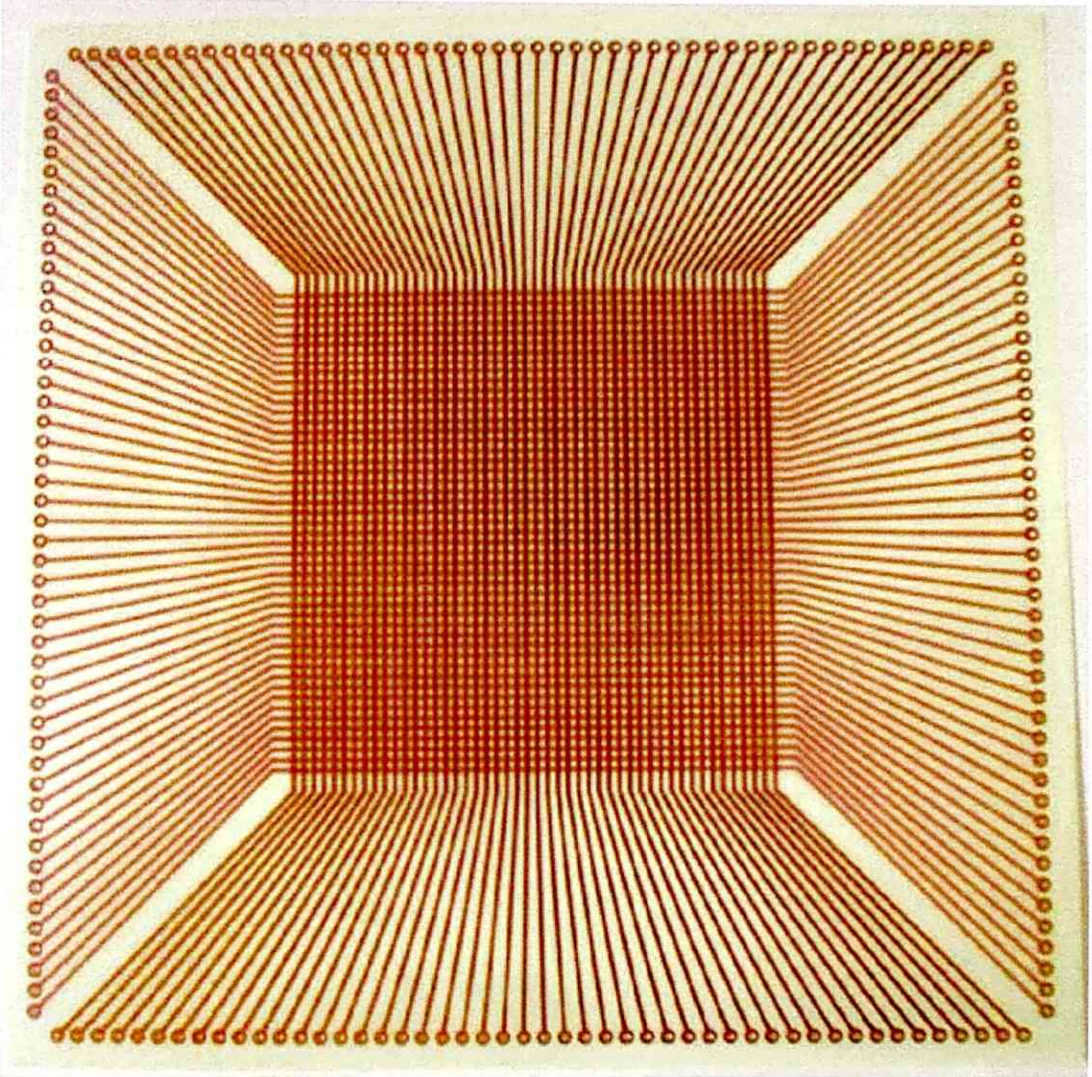

Fig. B-2: Photograph of the manufactured double-layered printed circuit board.

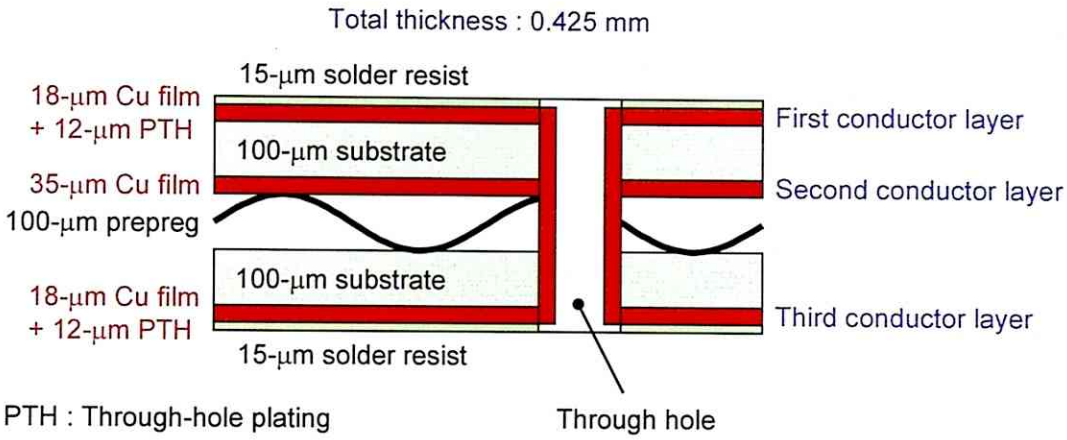

Fig. B-3: Cross-section view of triple-layered printed circuit board.

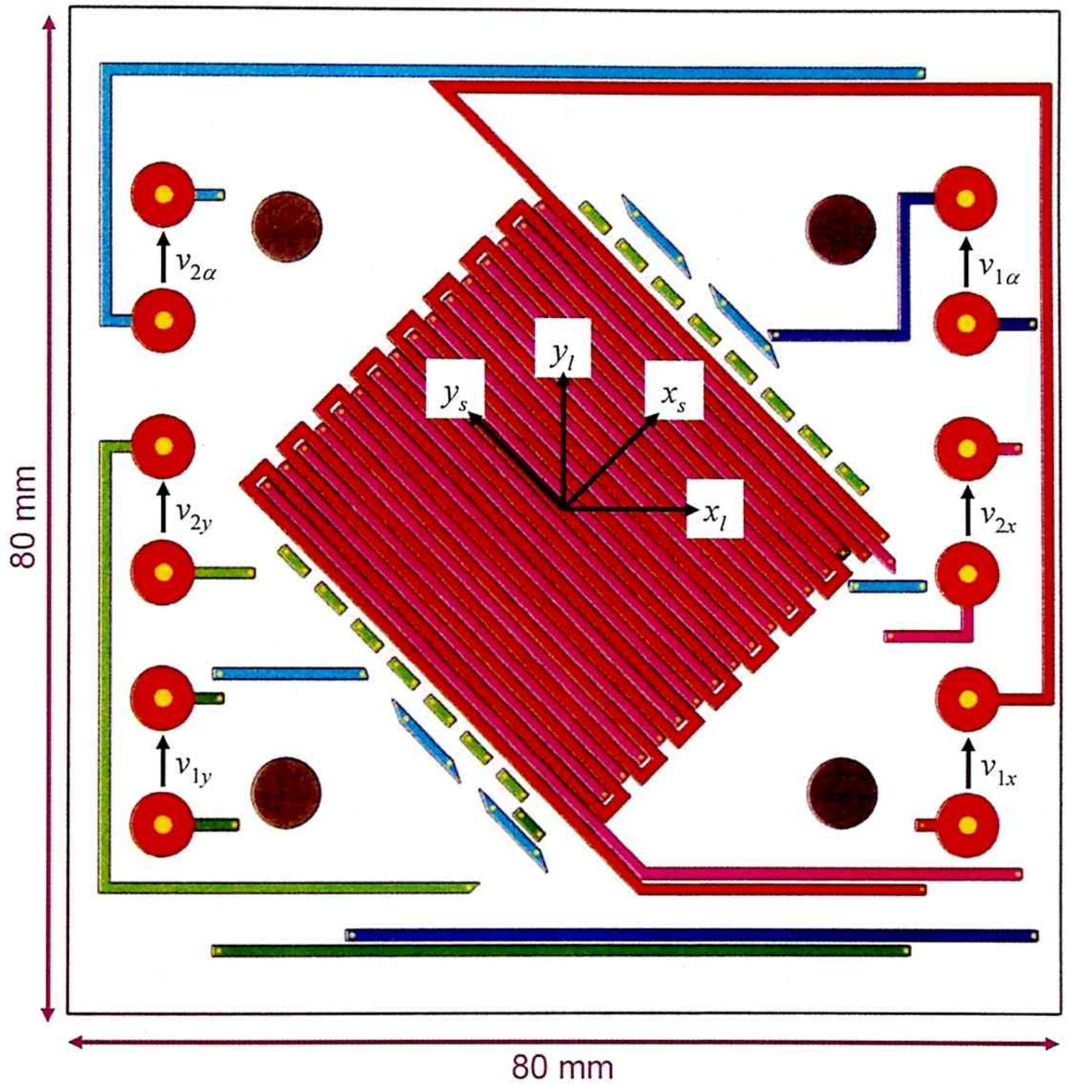

Fig. B-4: Structure of the first conductor layer. Red and pink lines represent the two-phase armature conductors for the x–directional drive; dark and light green lines represent the two-phase armature conductors for the y–directional drive; and dark and light blue lines represent the two-phase armature conductors for the α–directional drive.

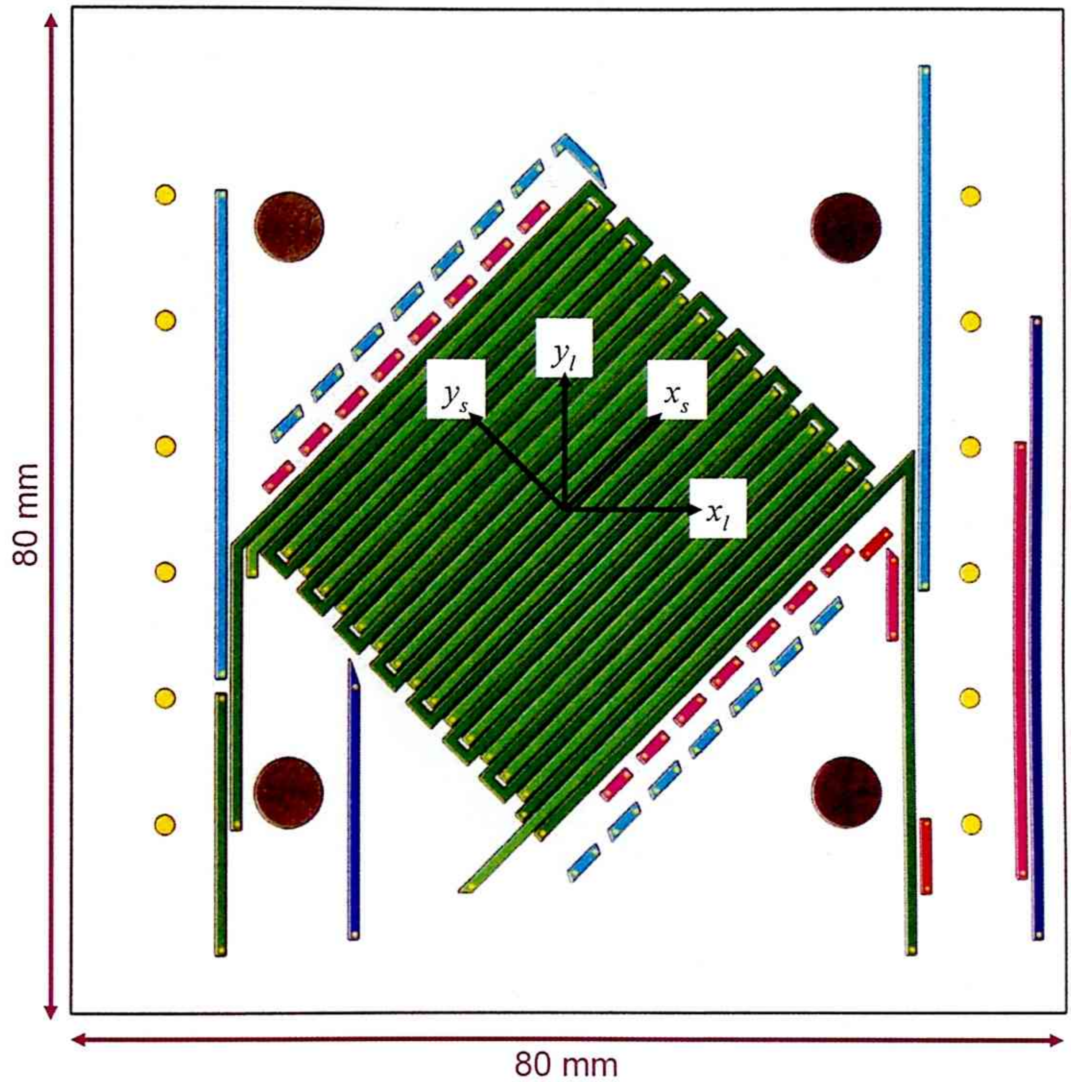

Fig. B-5: Structure of the second conductor layer. Red and pink lines represent the two-phase armature conductors for the x–directional drive; dark and light green lines represent the two-phase armature conductors for the y–directional drive; and dark and light blue lines represent the two-phase armature conductors for the α–directional drive.

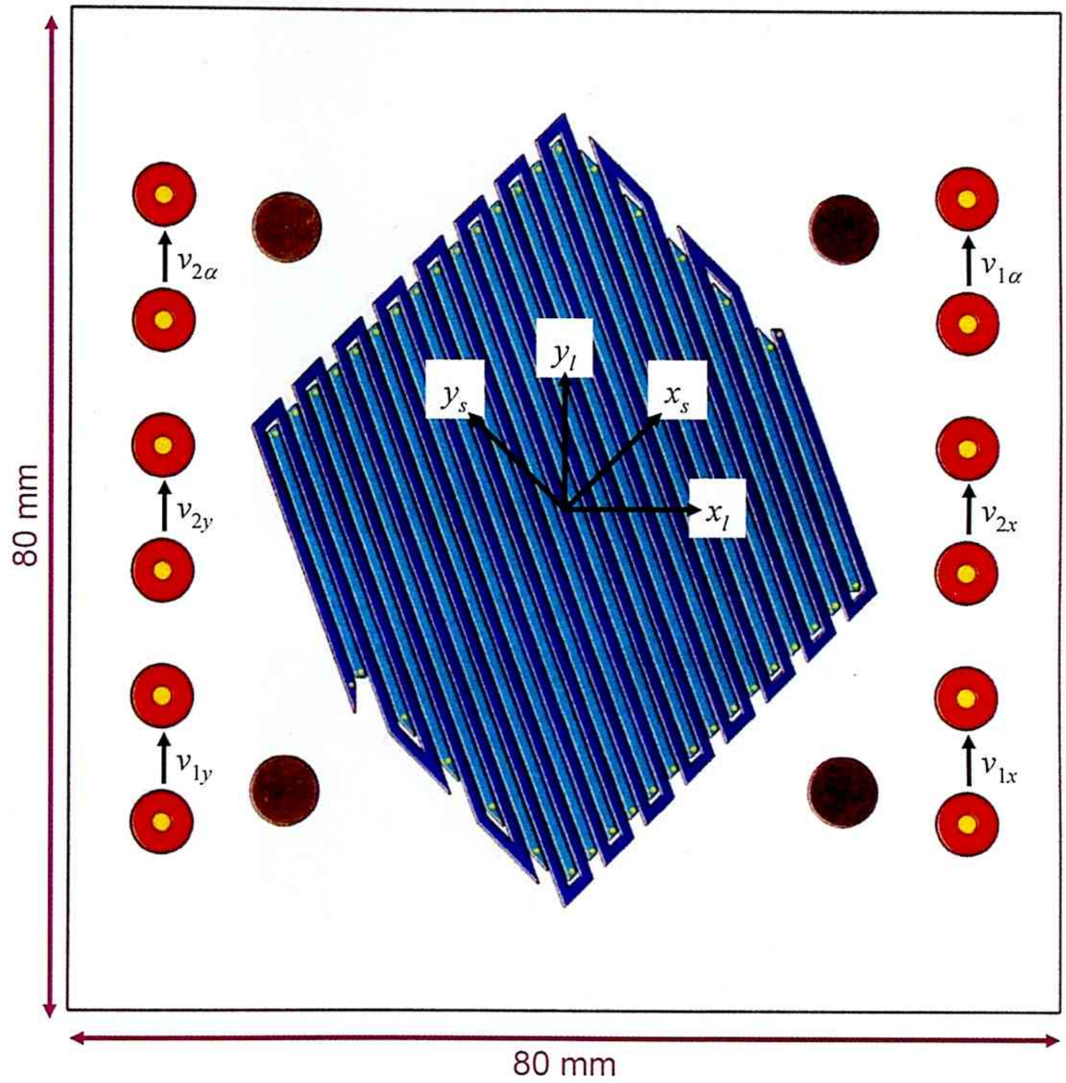

Fig. B-6: Structure of the third conductor layer. Dark and light blue lines represent the two-phase armature conductors for the α–directional drive.

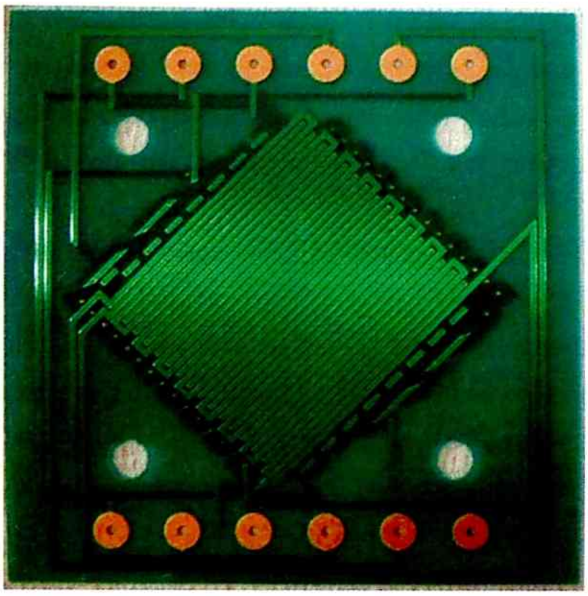

(a) Top view.

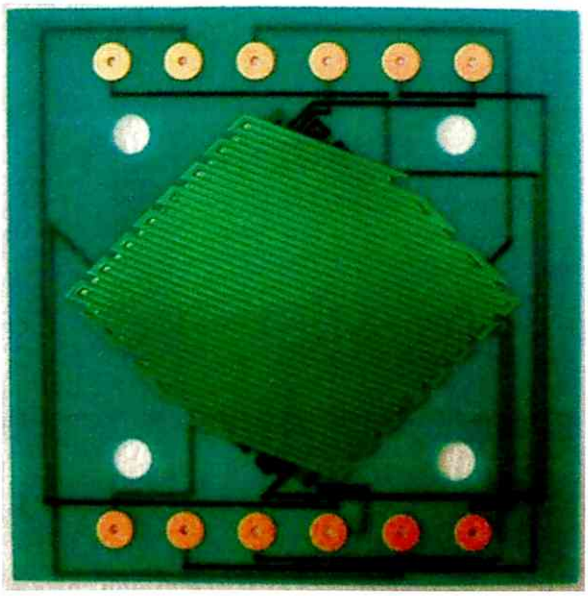

(b) Bottom view.

Fig. B-7: Photographs of the manufactured triple-layered printed circuit board.

C. 6-DOF Position Sensing Utilizing Laser-Displacement Sensors

In order to suspend the mover without mechanical contact, it is extremely important to detect the 6-DOF positions of the mover. In this study, a position-sensing method utilizing six laser-displacement sensors was investigated to precisely detect the position of the extremely small mover, the dimension of which are approximately 11 mm × 11 mm × 2 mm.

The six laser-displacement sensors are arranged as shown in Fig. C-1. As mentioned in Chapter 4, we measure the distance from the sensor head to the surface of an object using the sensors and the principle of laser triangulation. The sensors output a voltage proportional to the magnitude of the displacements from reference distance D. Sensors 1, 2, and 3 irradiate different lateral sides of the mover, and Sensors 4, 5, and 6 irradiate the same top surface of the mover. In this study, a sensor coordinate $x_l y_l z_l$ is defined to be tilted by −45 deg around the z_s–axis to the stationary coordinate $x_s y_s z_s$.

Six laser-displacement sensors are aligned so that path of the laser beam from Sensor i with respect to the sensor coordinate $x_l y_l z_l$, $\boldsymbol{r}_{li}$ (i = 1, 2, 3, 4, 5, or 6) can be represented as follows;

$$\boldsymbol{r}_{l1} = \begin{bmatrix} -D-\frac{w}{2} & 0 & 0 \end{bmatrix}^T + N_1\begin{bmatrix} 1 & 0 & 0 \end{bmatrix}^T \quad \text{(C-1)}$$

$$\boldsymbol{r}_{l2} = \begin{bmatrix} \frac{x_{23}}{2} & -D-\frac{l}{2} & 0 \end{bmatrix}^T + N_2\begin{bmatrix} 0 & 1 & 0 \end{bmatrix}^T \quad \text{(C-2)}$$

$$\boldsymbol{r}_{l3} = \begin{bmatrix} -\frac{x_{23}}{2} & D+\frac{l}{2} & 0 \end{bmatrix}^T + N_3\begin{bmatrix} 0 & -1 & 0 \end{bmatrix}^T \quad \text{(C-3)}$$

$$\boldsymbol{r}_{l4} = \begin{bmatrix} -db_4\sin\theta_4-\frac{x_{45}}{2} & -\frac{y_{56}}{2} & db_4\cos\theta_4+\frac{h}{2} \end{bmatrix}^T + N_4\begin{bmatrix} \sin\theta_4 & 0 & -\cos\theta_4 \end{bmatrix}^T \quad \text{(C-4)}$$

$$\boldsymbol{r}_{l5} = \begin{bmatrix} \frac{x_{45}}{2} & -db_5\sin\theta_5-\frac{y_{56}}{2} & db_5\cos\theta_5+\frac{h}{2} \end{bmatrix}^T + N_5\begin{bmatrix} 0 & \sin\theta_5 & -\cos\theta_5 \end{bmatrix}^T \quad \text{(C-5)}$$

$$\boldsymbol{r}_{l6} = \begin{bmatrix} \frac{x_{45}}{2} & db_6\sin\theta_6+\frac{y_{56}}{2} & db_6\sin\theta_6+\frac{h}{2} \end{bmatrix}^T + N_6\begin{bmatrix} 0 & -\sin\theta_6 & -\cos\theta_6 \end{bmatrix}^T \quad \text{(C-6)}$$

where w, l, and h are width, length, and height of the mover, respectively, x_{ij} and y_{ij} (i, j: 1, 2, 3, 4, 5, or 6) are relative positions between Sensors 1, 2, 3, 4, 5, or 6, and N_i is a positive number. Laser beams from Sensors 4, 5, and 6 are tilted by θ_4, θ_5, and θ_6 to the z_l–axis, respectively. When the mover position with respect to the stationary coordinate $x_s y_s z_s$ $\boldsymbol{r}_{sm} = [0 \quad 0 \quad 0]^T$ and the Euler angle $\boldsymbol{\phi} = [0 \quad 0 \quad 0]^T$, distances between the sensor head and measurement point in Sensors 4, 5, and 6 are db_4, db_5, and db_6, respectively.

The orientation of the mover can be calculated relatively easily by using a new Euler angle $\boldsymbol{\phi}_l = [\alpha_l \quad \beta_l \quad \gamma_l]^T$ that is defined by counterclockwise first α_l–rotation around the z_l–axis, second β_l–rotation around the y_l–axis, and third γ_l–rotation around the x_l–axis. The Euler angle γ_l can be represented by the amount of a displacement in the measurement points of Sensor 5, and 6 (ΔS_5, and ΔS_6, respectively, as shown in Fig. C-2) as follows:

$$\gamma_l = \tan^{-1}\left(\frac{-\Delta S_5 \cos\theta_5 + \Delta S_6 \cos\theta_6}{\Delta S_5 \sin\theta_5 + \Delta S_6 \sin\theta_6 + y_{56}}\right) \quad \text{(C-7)}$$

Next, the Euler angle β_l can be represented by β_l', which is a tilt angle of the mover to the $x_l - y_l$ plane about the y_l–axis, as follows:

$$\tan\beta_l = \tan\beta_l' \cdot \cos\gamma_l \quad \text{(C-8)}$$

Then, the tilt angle β_l' can be represented by the Euler angle γ_l and displacement of the measurement points ΔS_4, ΔS_5, ΔS_6 as follows:

$$\beta_l' = \tan^{-1}\left(\frac{\Delta S_4 \cos\theta_4 - \Delta S_5 \cos\theta_5 - \tan\gamma_l \cdot \Delta S_5 \sin\theta_5}{\Delta S_4 \sin\theta_4 + x_{45}}\right) \quad \text{(C-9)}$$

Therefore, the Euler angle β_l can be obtained by Eqs. (C-8) and (C-9) as shown in the following equation:

$$\beta_l = \tan^{-1}\left(\frac{\Delta S_4 \cos\theta_4 - \Delta S_5 \cos\theta_5 - \tan\gamma_l \cdot \Delta S_5 \sin\theta_5}{\Delta S_4 \sin\theta_4 + x_{45}} \times \cos\gamma_l\right) \quad \text{(C-10)}$$

Next, in order to obtain the Euler angle α_l, output signals of Sensors 2 and 3 are necessary. The y_l–directional positions of the points measured by Sensors 2 and 3, Y_2 and Y_3 as shown in Fig. C-3, can be calculated from the output signals. The y_l–directional distance between the two measurement points ($Y_3 - Y_2$) depends on only the Euler angle $\boldsymbol{\phi}_l = [\alpha_l \quad \beta_l \quad \gamma_l]^T$ and can be represented by the Euler angle as follows:

$$Y_3 - Y_2 = y_{L1} - y_{L2} \quad \text{(C-11)}$$

$$y_{L1} = a\cos\gamma_l + a\sin\gamma_l \tan\gamma_l' \quad \text{(C-12)}$$

$$y_{L2} = x_{23} \tan\alpha_l' \quad \text{(C-13)}$$

where α_l' and γ_l' express tilt angles about the z_l–axis in $x_l - y_l$ plane and about the x_l–axis in cross-section B–B', respectively, and can be represented as follows:

$$\gamma_l' = \tan^{-1}\left(\frac{\sin\alpha_l \sin\beta_l \cos\gamma_l + \cos\alpha_l \sin\gamma_l}{\sin\alpha_l \sin\beta_l \sin\gamma_l - \cos\alpha_l \cos\gamma_l}\right) \quad \text{(C-14)}$$

$$\alpha_l' = \tan^{-1}\left(\frac{\sin\alpha_l \cos\beta_l}{\cos\alpha_l \cos\gamma_l - \sin\alpha_l \sin\beta_l \sin\gamma_l}\right) \quad \text{(C-15)}$$

The Euler angle α_l can be calculated from Eqs. (C-11)–(C-15) and represented as follows;

$$\alpha_l = \sin^{-1}\left(\frac{a}{\sqrt{(x_{23}\cos\beta_l - (Y_3 - Y_2)\sin\beta_l \cdot \sin\gamma_l)^2 + ((Y_3 - Y_2)\cos\gamma_l)^2}}\right) - \tan^{-1}\left(\frac{(Y_3 - Y_2)\cos\gamma_l}{x_{23}\cos\beta_l - (Y_3 - Y_2)\sin\beta_l \cdot \sin\gamma_l}\right) \quad \text{(C-16)}$$

Next, in order to obtain the mover positions, a normal vector of each surface $\boldsymbol{n}_{msi}$ and a position vector of each surface center $\boldsymbol{r}_{msi}$ (i = 1, 2, 3, 4, 5, or 6) with respect to the sensor coordinate $x_l y_l z_l$ are introduced as shown in Fig. C-4. In Fig. C-4, O and O' express origins at the sensor and mover coordinates, respectively, and O_i' expresses center of surface i (i = 1, 2, 3, 4, 5, or 6). When the mover is not displaced from the base position, the normal vector $\boldsymbol{n}_{msi,0}$ and position vector $\boldsymbol{r}_{msi,0}$ can be represented as follows:

$$\begin{aligned} &\boldsymbol{n}_{ms1,0} = [1 \quad 0 \quad 0]^T, \quad \boldsymbol{n}_{ms2,0} = [-1 \quad 0 \quad 0]^T, \\ &\boldsymbol{n}_{ms3,0} = [0 \quad 1 \quad 0]^T, \quad \boldsymbol{n}_{ms4,0} = [0 \quad -1 \quad 0]^T, \\ &\boldsymbol{n}_{ms5,0} = [0 \quad 0 \quad 1]^T, \quad \boldsymbol{n}_{ms6,0} = [0 \quad 0 \quad -1]^T \end{aligned} \quad \text{(C-17)}$$

$$\begin{aligned} &\boldsymbol{r}_{ms1,0} = [w/2 \quad 0 \quad 0]^T, \quad \boldsymbol{r}_{ms2,0} = [-w/2 \quad 0 \quad 0]^T, \\ &\boldsymbol{r}_{ms3,0} = [0 \quad l/2 \quad 0]^T, \quad \boldsymbol{r}_{ms4,0} = [0 \quad -l/2 \quad 0]^T, \\ &\boldsymbol{r}_{ms5,0} = [0 \quad 0 \quad h/2]^T, \quad \boldsymbol{r}_{ms6,0} = [0 \quad 0 \quad -h/2]^T \end{aligned} \quad \text{(C-18)}$$

The normal vector $\boldsymbol{n}_{msi}$ and position vector $\boldsymbol{r}_{msi}$ can be calculated by the normal vector $\boldsymbol{n}_{msi,0}$ and position vector $\boldsymbol{r}_{msi,0}$ (i = 1, 2, 3, 4, 5, or 6) as follows:

$$\boldsymbol{n}_{msi} = \boldsymbol{R}_{lm}\boldsymbol{n}_{msi,0} \quad \text{(C-19)}$$

$$\boldsymbol{r}_{msi} = \boldsymbol{R}_{lm}\boldsymbol{r}_{msi,0} \quad \text{(C-20)}$$

where $\boldsymbol{R}_{lm}$ expresses the orientation of the mover with respect to the laser coordinate $x_l y_l z_l$ and can be represented by the Euler angle $\boldsymbol{\phi}_l$ as follows:

$$\boldsymbol{R}_{lm} = \begin{bmatrix} \cos\alpha_l\cos\beta_l & -\sin\alpha_l\cos\beta_l & \sin\beta_l \\ \sin\alpha_l\cos\gamma_l + \cos\alpha_l\sin\beta_l\sin\gamma_l & \cos\alpha_l\cos\gamma_l - \sin\alpha_l\sin\beta_l\sin\gamma_l & -\cos\beta_l\sin\gamma_l \\ \sin\alpha_l\sin\gamma_l - \cos\alpha_l\sin\beta_l\cos\gamma_l & \cos\alpha_l\sin\gamma_l + \sin\alpha_l\sin\beta_l\cos\gamma_l & \cos\beta_l\cos\gamma_l \end{bmatrix}. \quad \text{(C-21)}$$

A position vector of an arbitrary point on a surface i with respect to the sensor coordinate $x_l y_l z_l$, $\boldsymbol{r}_{lsi}$ (i = 1, 2, 3, 4, 5, or 6) satisfy the following equation:

$$\boldsymbol{n}_{msi}{}^T \cdot (\boldsymbol{r}_{lsi} - \boldsymbol{r}_{lm}) = 0 \quad \text{(C-22)}$$

where $\boldsymbol{r}_{lm}$ expresses the mover position with respect to the laser coordinate $x_l y_l z_l$. The mover position $\boldsymbol{r}_{lm}$ can be calculated from the Euler angle $\boldsymbol{\phi}_l$ by Eqs. (C-17)–(C-22) with respect to the three Surfaces 1, 3 (or 2), 6 (or 4, or 5).

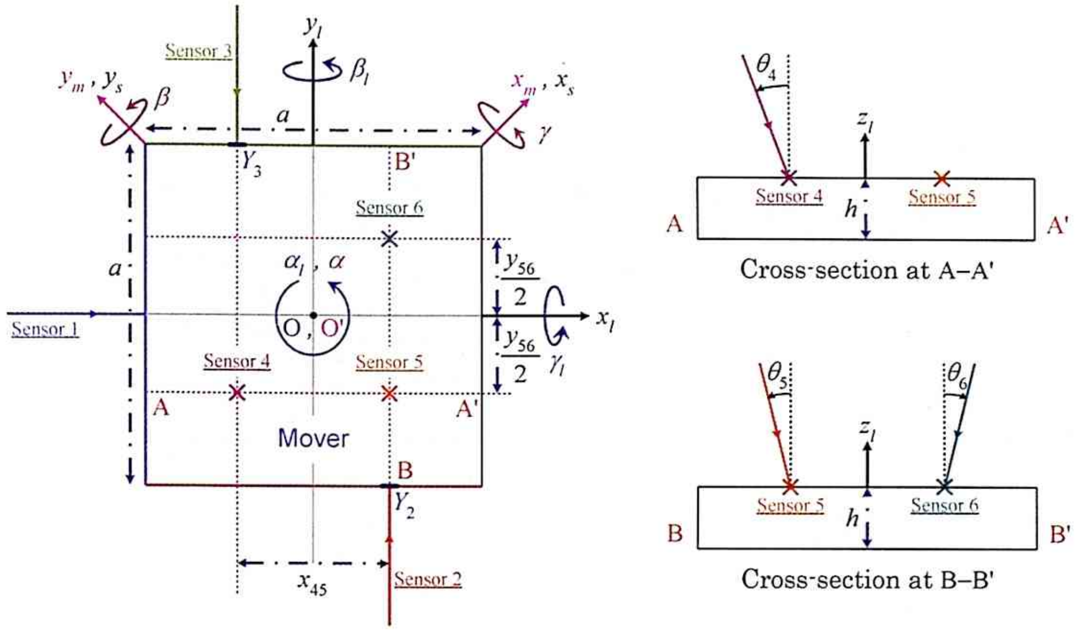

(a) Case in which the mover is not displaced from the base position.

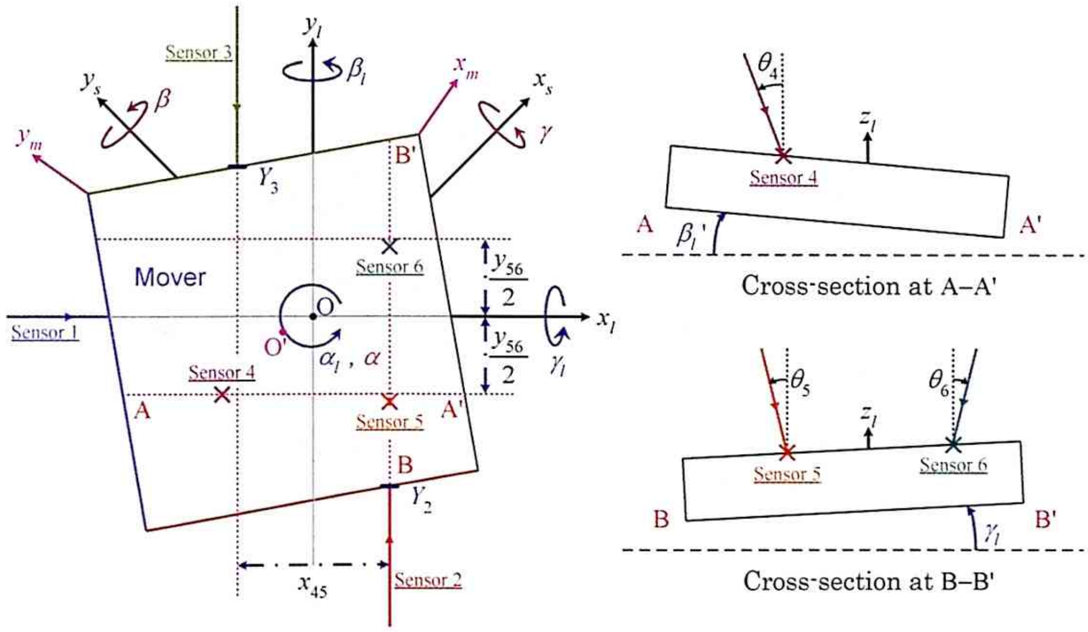

(b) Case in which the mover is displaced from the base position.

Fig. C-1: Position relation among the six laser beams and mover.

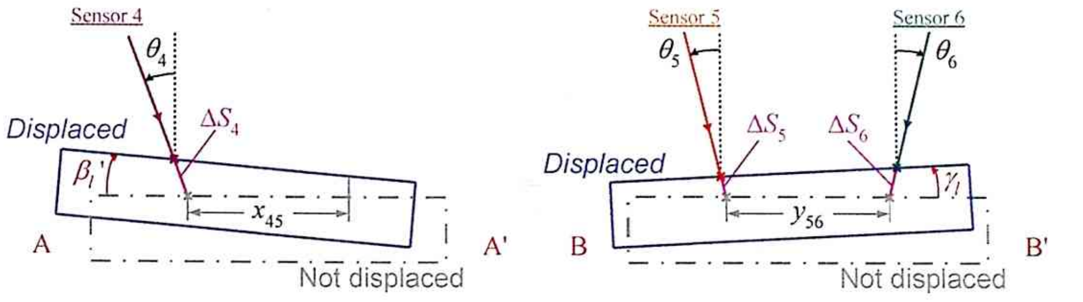

(a) Measurement point of Sensor 4. (b) Measurement points of Sensors 5 and 6.

Fig. C-2: Definition of displacements in the measurement points of Sensors 4, 5, and 6 from the base positions (ΔS_4, ΔS_5, and ΔS_6).

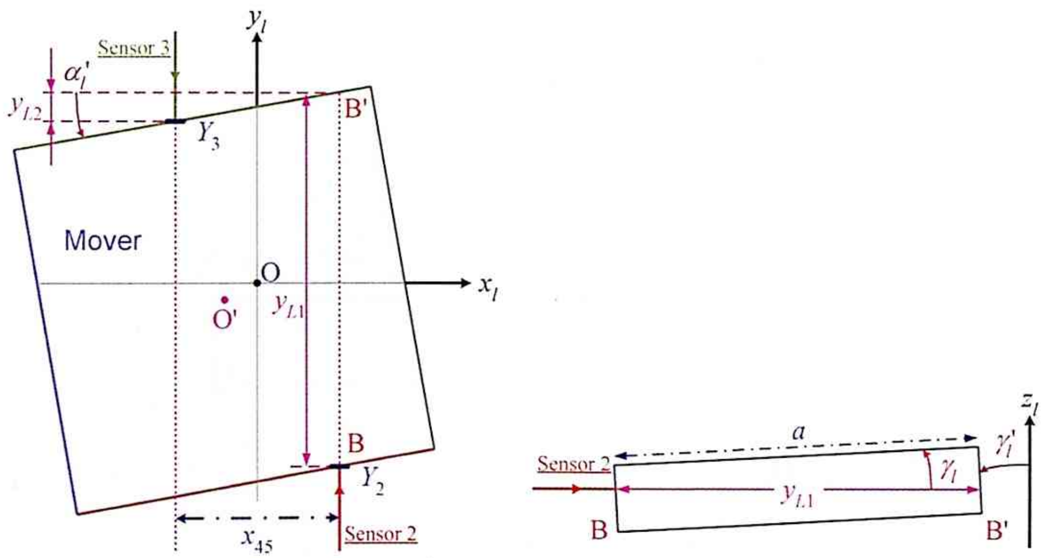

(a) Cross-section view in the $x_l - y_l$ plane. (b) Cross-section view at B–B'.

Fig. C-3: Displacements in the measurement points of Sensors 4, 5, and 6 from the base positions (ΔS_4, ΔS_5, and ΔS_6).

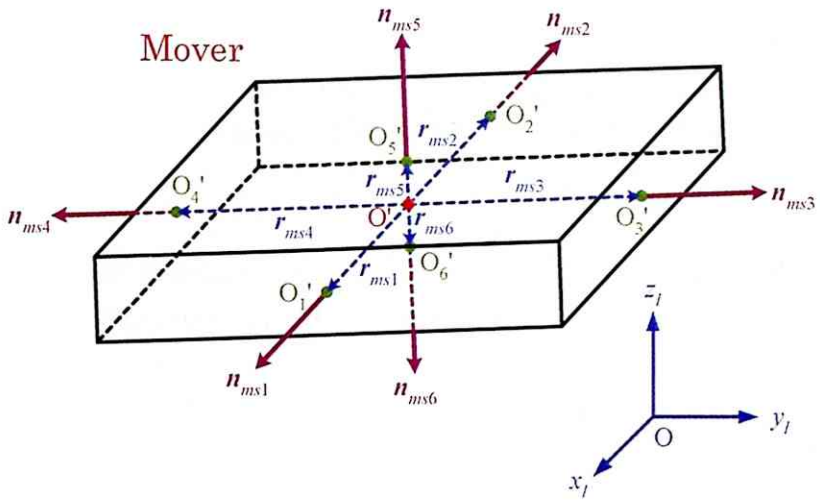

(a) Case in which the mover is not displaced from the base position.

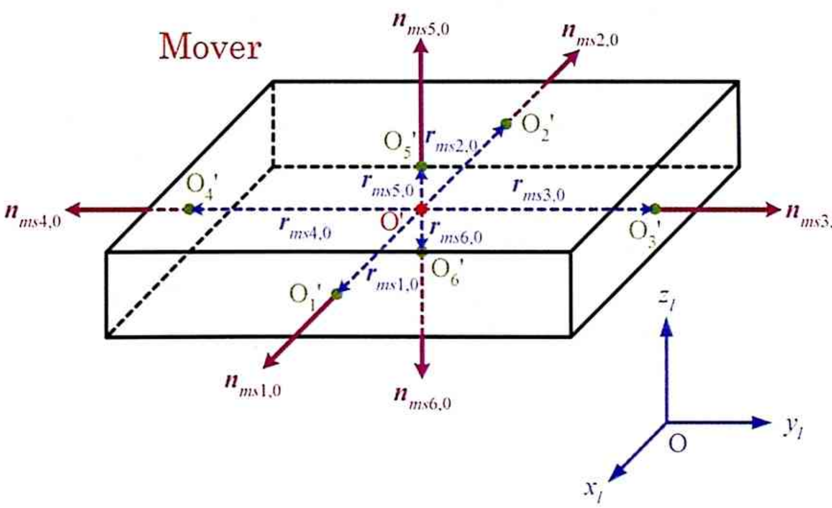

(b) Case in which the mover is displaced from the base position.

Fig. C-4: Definition of the normal vector of each surface $\boldsymbol{n}_{msi}$ and the position vector of each surface center $\boldsymbol{r}_{msi}$ with respect to the sensor coordinate $x_ly_lz_l$.

Next, the mover position $\boldsymbol{r}_{lm}$ and Euler angle $\boldsymbol{\phi}_l$ with respect to the laser coordinate $x_ly_lz_l$ are transformed with respect to the stationary coordinate $x_sy_sz_s$, because the control system of the mover position $\boldsymbol{r}_{sm}$ and Euler angle $\boldsymbol{\phi}$ with respect to the stationary coordinate $x_sy_sz_s$ were designed in Chapter 6.

The laser coordinate $x_ly_lz_l$ are tilted by −45 deg around the z_s–axis from the stationary coordinate $x_sy_sz_s$. Therefore, the mover position $\boldsymbol{r}_{sm}$ with respect to the stationary coordinate $x_sy_sz_s$ can be represented by that $\boldsymbol{r}_{lm}$ the laser coordinate $x_ly_lz_l$ as follows:

$$\boldsymbol{r}_{sm} = \boldsymbol{R}_{sl}\boldsymbol{r}_{lm} \quad \text{(C-23)}$$

where $\boldsymbol{R}_{sl}$ expresses a rotation matrix that generates a −45 deg counterclockwise rotation around the z_s–axis and can be represented as follows:

$$\boldsymbol{R}_{sl} = \begin{bmatrix} \cos(45°) & \sin(45°) & 0 \\ -\sin(45°) & \cos(45°) & 0 \\ 0 & 0 & 1 \end{bmatrix}. \quad \text{(C-24)}$$

The orientation $\boldsymbol{R}_{lm}$, defined by the Euler angle $\boldsymbol{\phi}_l = [\alpha_l \quad \beta_l \quad \gamma_l]^T$ based on rotations around the z_l–, y_l–, and x_l–axes as shown in Eq. (C-21), can also be represented by the Euler angle $\boldsymbol{\phi} = [\alpha \quad \beta \quad \gamma]^T$ based on rotations around the z_s–, y_s–, and x_s–axes. Vectors of the y_s– and x_s–axes with respect to the laser coordinate $x_ly_lz_l$, $\boldsymbol{\lambda}_{ly}$ and $\boldsymbol{\lambda}_{lx}$, are represented as follows:

$$\boldsymbol{\lambda}_{ly} = \boldsymbol{R}_{sl}^{-1}\begin{bmatrix} 0 \\ 1 \\ 0 \end{bmatrix} = \begin{bmatrix} -1/\sqrt{2} \\ 1/\sqrt{2} \\ 0 \end{bmatrix} \quad \text{(C-25)}$$

$$\boldsymbol{\lambda}_{lx} = \boldsymbol{R}_{sl}^{-1}\begin{bmatrix} 1 \\ 0 \\ 0 \end{bmatrix} = \begin{bmatrix} 1/\sqrt{2} \\ 1/\sqrt{2} \\ 0 \end{bmatrix}. \quad \text{(C-26)}$$

From Eqs. (6.2.2-1)–(6.2.2-3) and (C-25)–(C-26), the orientation $\boldsymbol{R}_{lm}$ can also be represented by utilizing the Euler angle $\boldsymbol{\phi}$ as follows;

$$\boldsymbol{R}_{lm} = [\boldsymbol{R}_{lm1} \quad \boldsymbol{R}_{lm2} \quad \boldsymbol{R}_{lm3}]. \quad \text{(C-27)}$$

where $\boldsymbol{R}_{lm1}$, $\boldsymbol{R}_{lm2}$, and $\boldsymbol{R}_{lm3}$ can be represented as follows:

$$\boldsymbol{R}_{lm1} = \frac{1}{2}\begin{bmatrix} \sin\alpha\cdot(-\sin\beta\cdot\sin\gamma+\cos\beta-\cos\gamma)+\cos\alpha\cdot(-\sin\beta\cdot\sin\gamma+\cos\beta+\cos\gamma) \\ \sin\alpha\cdot(\sin\beta\cdot\sin\gamma+\cos\beta+\cos\gamma)+\cos\alpha\cdot(\sin\beta\cdot\sin\gamma+\cos\beta-\cos\gamma) \\ \sqrt{2}(\sin\alpha\cdot(-\sin\beta\cdot\cos\gamma+\sin\gamma)+\cos\alpha\cdot(-\sin\beta\cdot\cos\gamma-\sin\gamma)) \end{bmatrix} \quad \text{(C-28)}$$

$$\boldsymbol{R}_{lm2} = \frac{1}{2}\begin{bmatrix} \sin\alpha\cdot(\sin\beta\cdot\sin\gamma-\cos\beta-\cos\gamma)+\cos\alpha\cdot(-\sin\beta\cdot\sin\gamma+\cos\beta-\cos\gamma) \\ \sin\alpha\cdot(-\sin\beta\cdot\sin\gamma-\cos\beta+\cos\gamma)+\cos\alpha\cdot(\sin\beta\cdot\sin\gamma+\cos\beta+\cos\gamma) \\ \sqrt{2}(\sin\alpha\cdot(\sin\beta\cdot\cos\gamma+\sin\gamma)+\cos\alpha\cdot(-\sin\beta\cdot\cos\gamma+\sin\gamma)) \end{bmatrix}$$

.... (C-29)

$$\boldsymbol{R}_{lm3} = \frac{1}{\sqrt{2}}\begin{bmatrix} \sin\beta+\cos\beta\cdot\sin\gamma \\ \sin\beta-\cos\beta\cdot\sin\gamma \\ \sqrt{2}\cos\beta\cdot\cos\gamma \end{bmatrix} \quad \text{(C-30)}$$

From Eqs. (C-21) and (C-27)–(C-30), the Euler angle $\boldsymbol{\phi}$ can be represented by the different Euler angle $\boldsymbol{\phi}_l$ as follows:

$$\alpha = \sin^{-1}\left(\frac{(\sin\alpha_l+\cos\alpha_l)(\sin\beta_l\sin\gamma_l+\cos\beta_l)+(\sin\alpha_l-\cos\alpha_l)\cos\gamma_l}{2\cos\beta}\right) \quad \text{(C-31)}$$

$$\beta = \sin^{-1}\left(\frac{\sin\beta_l-\cos\beta_l\sin\gamma_l}{\sqrt{2}}\right) \quad \text{(C-32)}$$

$$\gamma = \sin^{-1}\left(\frac{\sqrt{2}\sin\beta_l-\sin\beta}{\cos\beta}\right) \quad \text{(C-33)}$$

As mentioned above, the 6-DOF mover position can be detected by using the six laser-displacement sensors. Figure C-5 shows the calculation procedure of the 6-DOF position from the output signals of the six laser-displacement sensors.

Next, I fabricated the position-sensing system shown in Fig. C-6, and then investigated the characteristics. The specifications of the fabricated position-sensing system are shown as follows:

- Sensors 1, 2, and 3: LK-080 [Key01]
- Sensors 4, 5, and 6: LK-G080 [Key02]
- tilted angles of laser beams from Sensors 4, 5, and 6 to z_l-axis: θ_4 = 25 deg, θ_5 = 15 deg, and θ_6 = 15 deg
- distances between sensor head and measurement point in Sensors 4, 5, and 6: db_4 = 70 mm, db_5 = 68 mm, and db_6 = 68 mm.

The results show there are important problems to be resolved; the detected positions include errors caused by dimension and placement errors of each piece of experimental apparatuses, property variations of the sensors and power amplifiers due to temperature variations, electrical noise, and so on. Furthermore, these errors can induce identification errors in the system-constant matrix $\boldsymbol{K}$ in the motion-control algorithm, and deteriorate the motion-control characteristics. Therefore, calibrating the position sensing system is an extremely important issue.

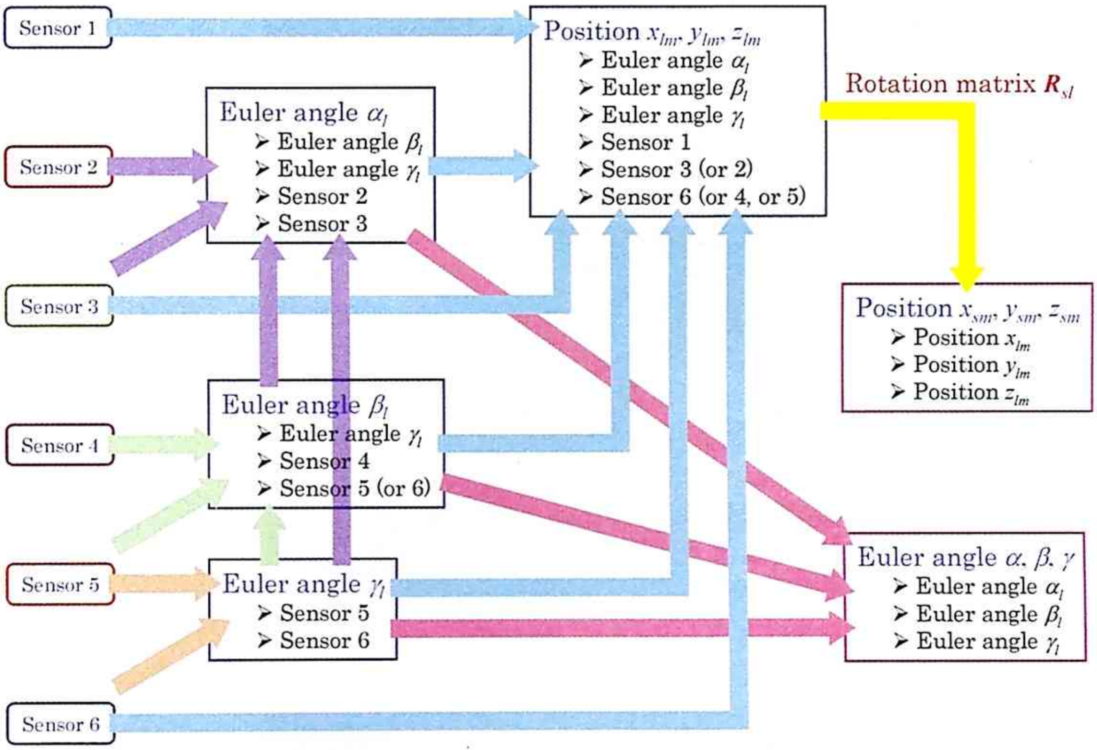

Fig. C-5: Calculation procedure for the 6-DOF position from the output signals of the six laser-displacement sensors.

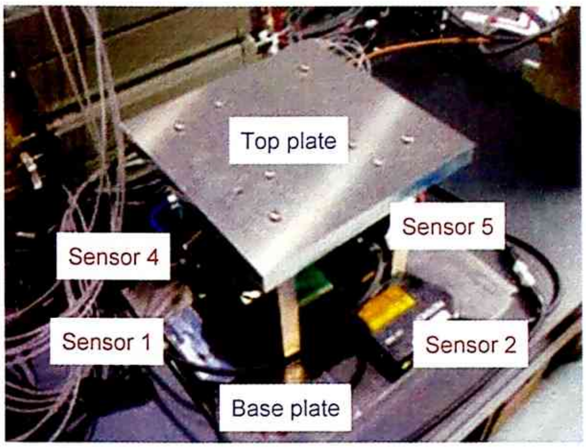

(a) Top view.

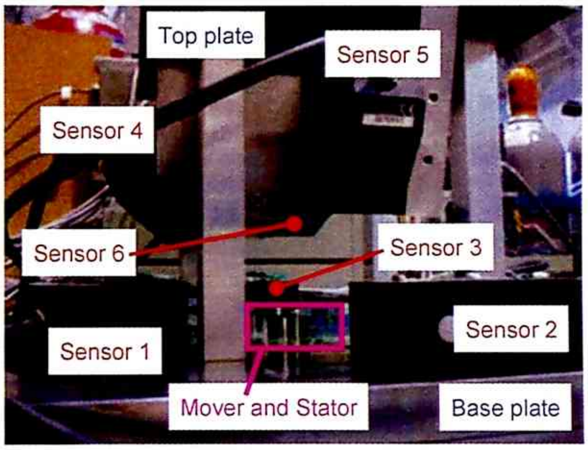

(b) Side view.

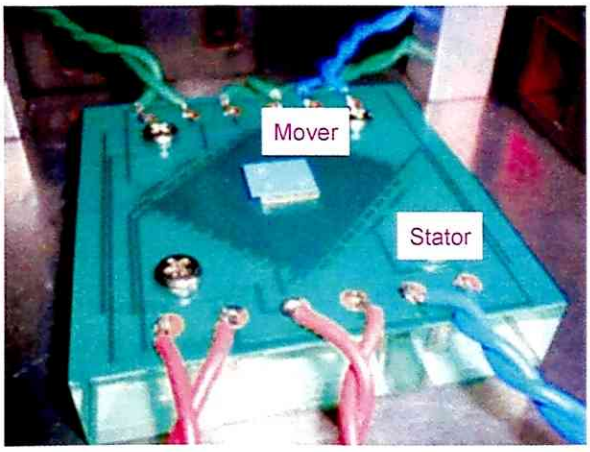

(c) Mover and stator.

Fig. C-6: Fabrication of position-sensing system with 6 DOF.

Bibliography

[ACh98] A. Chitayat, "Two-Axis Motor with High Density Magnetic Platen," *U.S. Patent* 5 777 402, July 7, 1998.

[Act04] Technical Committee on Actuator Systems, "Actuator Engineering," *Yokendo*, December 2004 (in Japanese).
アクチュエータシステム技術企画委員会,「アクチュエータ工学」, 養賢堂, 2004 年 12 月.

[Aoy03] T. Nakajima, M. Aoyagi, Y. Tomikawa, and T. Takano, "Examination of High-Power Disk-Type Multi-Degree-of-Freedom Ultrasonic Motor," *IEICE Technical Report, Ultrasonics*, Vol.103, No.340, pp.49-54, September 2003 (in Japanese).
中島俊典, 青柳学, 富川義朗, 高野剛浩,「円環型多自由度超音波モータの高出力化の検討」, 電子情報通信学会 技術研究報告, 超音波, Vol.103, No.340, pp.49-54, 2003 年 9 月.

[Aoy04] M. Aoyagi, T. Nakajima, Y. Tomikawa, and T. Takano, "Examination of Disk-Type Multi-Degree-of-Freedom Ultrasonic Motor," *Japanese Journal of Applied Physics*, Vol.43, No.5B, pp.2884-2890, May 2004.

[Asa85] T. Asakawa, "Two-Dimensional Precise Positioning Device for Use in a Semiconductor Manufacturing Apparatus," *U.S. Patent* 4 535 278, August 13, 1985.

[Bin03a] M. Binnard, "System and Method to Control Planar Motors," *U.S. Patent* 6 650 079, November 18, 2003.

[Bin03b] M. Binnard, "Six Degree of Freedom Control of Planar Motors," *U.S. Patent Application Publication* 2003/0085676, May 8, 2003.

[Buc89] J.D. Buckley, D.N. Galburt, and C. Karatzas, "Step-and-Scan Lithography Using Reduction Optics," *Journal of Vacuum Science and Technology B*, Vol.7, No.6, pp.1607-1612, November 1989.

[Chi99] G.S. Chirikjian and D. Stein, "Kinematic Design and Commutation of a Spherical Stepper Motor," *IEEE/ASME Transactions on Mechatronics*, Vol.4, No.4, pp.342-353, December 1999.

[Com03] J.C. Compter, "A Planar Motor with Electro-Dynamic Propulsion and Levitation under 6-DOF Control," *The International Symposium on Linear Drives for Industry Applications (LDIA2003)*, MA-01, pp.149-152, Birmingham, UK, September 2003.

[Com04] J.C. Compter, "Electro-Dynamic Planar Motor," *Precision Engineering*, Vol.28, No.2, pp.171-180, April 2004.

[Com07] J.C. Compter, "Towards Planar Drives for Lithography," *The International Symposium on Linear Drives for Industry Applications (LDIA2007)*, KS2.1, Lille, France, September 2007.

[Cyb01] Cybernet Systems, "MATLAB User's Manual".

[Don00] K. Kahlen and R.W. De Doncker, "Current Regulators for Multi-Phase Permanent Magnet Spherical Machines," *The 35th IEEE-IAS Annual Meeting*, Vol.3, pp.2011-2016, Rome, Italy, October 2000.

[Don02] K. Kahlen, I. Voss, and R.W. De Doncker, "Control of Multi-Dimensional Drives with Variable Pole Pitch," *The 37th IEEE-IAS Annual Meeting*, Vol.4, pp.2366-2370, Pennsylvania, USA, October 2002.

[Ebi02] A. Tanaka, M. Watada, S. Torii, and D. Ebihara, "Proposal and Design of Multi-Degree-of-Freedom Spherical Actuator," *Magnetodynamics Conference (MAGDA11)*, pp.169-172, Tokyo, March 2002 (in Japanese).
田中飛鳥，和多田雅哉，鳥居粛，海老原大樹，「多自由度アクチュエータの提案と設計」，第11回MAGDAコンファレンス講演論文集, pp.169-172, 東京, 2002年3月.

[Ebi03] S. Torii, H. Nakano, T. Yamaguchi, D. Ebihara, Y. Hasegawa, and K. Hirata, "Characteristics of the Two-Dimensional Oscillatory Actuator with Attractive Force of Driving Source," *The International Symposium on Linear Drives for Industry Applications (LDIA2003)*, pp.101-104, Birmingham, UK, September 2003.

[Ebi05] Y. Honda, S. Torii, D. Ebihara, Y. Hasegawa, and K. Hirata, "Development of Cylindrical Two-Dimensional Linear Oscillatory Actuator," *The International Symposium on Linear Drives for Industry Applications (LDIA2005)*, pp.266-269, Awaji, Japan, September 2005.

[Ebi89] D. Ebihara and M. Watada, "Study of a Basic Structure of Surface Actuator," *IEEE Transaction on Magnetics*, Vol.25, No.5, pp.3916-3918, September 1989.

[Ebi91] D. Ebihara, M. Watada, and H. Higashino, "Basic Structure of Four-Phase PM-Type Stepping Surface Motor and the Driving Method," *IEEJ Transaction on Industry Applications*, Vol.111, No.8, pp.654-660, August 1991 (in Japanese).
海老原大樹, 和多田雅哉, 東野浩幸, 「四相 PM 型ステッピングサーフェースモータの基本構造とその駆動方式」, 電気学会 論文誌 D, Vol.111, No.8, pp.654-660, 1991 年 8 月.

[Edw01] E.P. Furlani, "Permanent magnet and electromechanical devices : materials, analysis, and applications," *San Diego : Academic Press*, 2001.

[Fit90] A.E. Fitzgerald, C. Kingsley, Jr., and S. Umans, "Electric Machinery," *Mc-Graw Hill, Inc.*, Sixth Edition, 2003.

[Fon03] Antoine Ferreira and Jean-Guy Fontaine, "Dynamic Modeling and Control of a Conveyance Microrobotic System Using Active Friction Drive," *IEEE/ASME Transactions on Mechatronics*, Vol.8, No.2, pp.188- 202, June 2003.

[Fuj02] N. Fujii and K. Okinaga, "X-Y Linear Synchronous Motors without Force Ripple and Core Loss for Precision Two-Dimensional Drives," *IEEE Transaction on Magnetics*, Vol.38, No.5, pp.3273-3275, September 2002.

[Fuj99] N. Fujii and M. Fujitake, "Two-Dimensional Drive Characteristics by Circular-Shaped Motor," *IEEE Transaction on Industry Applications*, Vol.35, No.4, pp.803-809, July 1999.

[Fuk04] H. Fukunaga, "The Present State of High-Performance Magnets," *IEEJ Journal*, Vol.124, No.11, p.694, November 2004 (in Japanese).
福永博俊, 「高性能永久磁石の現状」, 電気学会誌, Vol.124, No.11, p.694, 2004 年 11 月.

[Gal85] D. Galburt, "Electro-Magnetic Apparatus," *U.S. Patent* 4 506 204, March 19, 1985.

[GKi01] J. Tsuchiya and G. Kimura, "Mover Structure and Thrust Characteristic of Moving-Magnet-Type Surface Motor," *The 27th Annual Conference of the IEEE Industrial Electronics Society (IECON'01)*, pp.1469-1474, Colorado, USA, November 2001.

[GKi94] K. Yamazaki, T. Shimizu, and G. Kimura, “The Motion Characteristics of a New Surface Actuator,” *IEEJ Annual Meeting on Industry Applications*, pp.910-913, Matsuyama, August 1994 (in Japanese).
山崎憲一, 清水敏久, 木村軍司, 「3 自由度を持つサーフェスアクチュエータの移動特性解析」, 平成 6 年 電気学会 産業応用部門大会, pp.910-913, 松山, 1994 年 8 月.

[Gol80] H. Goldstein, “Classical Mechanics,” *Addison-Wesley Publishing Co., Inc.*, Third Edition, 2001.

[Hal86] K. Halbach, “Concepts for Insertion Devices that will Produce High-Quality Synchrotron Radiation,” *Nuclear Instruments and Methods in Physics Research Section A*, Vol.246, No.1-3, pp.77-81, May 1986.

[Has01] S. Hashida, F. Kaiho, Y. Koizumi, and T. Tamura, “Surface Servo Motor “PLANESERV”,” Yokogawa Technical Report, Vol.45, No.2, pp.83-86, 2001 (in Japanese).
橋田茂, 海保文雄, 小泉豊, 田村哲司, 「平面サーボモータ PLANESERV とその要素技術」, 横河技報, Vol.45, No.2, pp.83-86, 2001 年.

[Hig04] A. Yamamoto, K. Mori, H. Yoshioka, and T. Higuchi, “2-DOF Electrostatic Surface Actuator Using Mesh-Type Printed Electrodes,” *The 2004 JSPE Autumn Technical Meeting*, B19, pp.117-118, shimane, September 2004 (in Japanese).
山本晃生, 森孝太, 吉岡久智, 樋口俊郎, 「メッシュ状印刷電極を用いた 2 自由度平面静電アクチュエータ」, 2004 年度 精密工学会 秋季大会 学術講演会, B19, pp.117-118, 島根, 2004 年 9 月.

[Hig06] T. Higuchi, “Electrostatic Motors,” *Symposium materials on Motor Technologies in TECHNO–FRONTIER 2006*, Makuhari, April 2006 (in Japanese).
樋口俊郎, 「静電モータ」, TECHNO–FRONTIER 2006 モータ技術シンポジウム資料, 幕張, 2006 年 4 月.

[Hig07] T. Ueno, E. Summers, M. Wun-Fogle, and T. Higuchi, “Micro Magnetostrictive Vibrator using Iron-Gallium Alloy (Galfenol),” *Journal of Magnetics Society of Japan*, Vol.31, No.4, pp.372-375, July 2007 (in Japanese).
上野敏幸, エリック・サマーズ, マリリン・ウンフォーグル, 樋口俊郎, 「Fe-Ga 合金(Galfenol)を用いたマイクロ磁歪振動子」, 日本応用磁気学会誌, Vol.31, No.4, pp.372-375, 2007 年 7 月.

[Hig08a] T. Ueno, E. Summers, and T. Higuchi, "Machining of Iron–Gallium Alloy for Microactuator," *Sensors and Actuators A: Physical*, Vol.137, No.1, pp.134-140, June 2007.

[Hig08b] T. Ueno, T. Higuchi, C. Saito, and N. Imaizumi, "Micro Spherical Motor using Iron-Gallium Alloy (Galfenol)," *The 20th Symposium on Electromagnetics and Dynamics (sead20)*, 23A2-4, pp.597-600, Beppu, May 2008 (in Japanese).
上野敏幸, 樋口俊郎, 斉藤千尋, 今泉伸夫, 「Fe-Ga 合金(Galfenol)を用いたマイクロ球面モータ」, 第 20 回「電磁力関連のダイナミクス」シンポジウム, 23A2-4, pp.597-600, 別府, 2008 年 5 月.

[Hig89] T. Higuchi and H. Kawakatsu, "Development of a Magnetically Suspended Stepping Motor for Clean-Room Transportation and Sample Handling," *The International Conference on Magnetically Levitated Systems and Linear Drives (Maglev'89)*, pp.363-368, Yokohama, Japan, July 1989.

[Hig90] T. Higuchi, A. Horikoshi, and T. Komori, "Development of an Actuator for Super Clean Rooms and Ultra High Vacua," *The 2nd International Symposium on Magnetic Bearings*, pp.115-122, Tokyo, Japan, July 1990.

[Hin87] W.E. Hinds, "Single Plane Orthogonally Movable Drive System," *U.S. Patent* 4 654 571, March 31, 1987.

[Hir04] Y. Kawase, T. Yamaguchi, H. Naito, M. Tanaka, K. Hirata, and Y. Hasegawa, "3D FEM Coupled with the Rotation and Linear Motion Equation," *IEEJ Tech. Meeting on Static Apparatus and Rotating Machinery*, SA-04-24/RM-04-24, pp.63-66, Chiba, January 2004 (in Japanese).
河瀬順洋, 山口忠, 内藤裕彰, 田中雅和, 平田勝弘, 長谷川祐也, 「2 自由度駆動アクチュエータの回転運動と直線運動の連成」, 電気学会 静止器／回転機合同研究会, SA-04-24/RM-04-24, pp.63-66, 千葉, 2004 年 1 月.

[Hir05] Y. Hasegawa and K. Hirata, "A Study on Electromagnetic Actuator with Two-Degree-of-Freedom," *IEEJ Transactions on Industry Applications*, Vol.125, No.5, pp.519-523, May 2005 (in Japanese).
長谷川 祐也, 平田 勝弘, 「2 自由度電磁アクチュエータの研究」, 電気学会論文誌 D, Vol.125, No.5, pp.519-523, 2005 年 5 月.

[Hir08] Y. Hasegawa, K. Hirata, T. Yamamoto, Y. Mitsutake. and T. Ota, "New Spherical Resonant Actuator," *IEEJ Transactions on Industry Applications*, Vol.127-8, No.5, pp.642-647, May 2008.

[HNa04] H. Nakamura, "Magnetic Properties of Miniature Nd-Fe-B Sintered Magnets," *IEEJ Journal*, Vol.124, No.11, pp.699-702, November 2004 (in Japanese).
中村元, 「超微小に加工された Nd-Fe-B 系焼結磁石」, 電気学会誌, 電気学会誌, Vol.124, No.11, pp.699-702, 2004 年 11 月.

[HOh07] J.W. Jeon, M. Caraiani, Y.J. Kim, H.S. Oh, and S.S. Kim, "Development of Magnetic Levitated Stage for Wide Area Movements," *The International Conference on Electrical Machines and Systems (ICEMS2007)*, pp.1486-1491, Seoul, Korea, October, 2007.

[Hol98] Z.J. Butler, A.A. Rizzi, and R.L. Hollis, "Integrated Precision 3-DOF Position Sensor for Planar Linear Motors," *IEEE International Conference on Robotics and Automation*, pp.3109-3114, Leuven, Belgium, May 1998.

[How01] Z.O. Zhu and D. Howe, "Halbach Permanent Magnet Machines and Applications: A Review," *IEE Proceedings-Electric Power Applications*, Vol.148, No.4, pp.299-308, July 2001.

[Ish97] J. Ish-Shalom, "Modeling of Sawyer Planar Sensor and Motor Dependence on Planar Yaw Angle Rotation," *IEEE International Conference on Robotics and Automation*, Albuquerque, pp.3499-3504, New Mexico, April 1997.

[Jan07] J.W. Jansen, "Magnetically Levitated Planar Actuator with Moving Magnets: Electromechanical Analysis and Design," *PhD thesis, Eindhoven University of Technology*, November 2007.

[Jun02] H.S. Cho and H.K. Jung, "Analysis and Design of Synchronous Permanent-Magnet Planar Motors," *IEEE Transactions on Energy Conversion*, Vol.17, No.4, pp.492-499, December 2002.

[Joh97] J. Ormerod and S. Constantinides, "Bonded permanent magnets: Current status and future opportunities," *Journal of Applied Physics*, Vol.81, No.8, pp.4816-4820, April 1997.

[Kan04] Y. Kaneko, "Toward the Theoretical Value of Nd-Fe-B Sintered Magnets," *IEEJ Journal*, Vol.124, No.11, pp.695-698, November 2004 (in Japanese).
金子裕治, 「理論値を目指すNd-Fe-B焼結磁石」, 電気学会誌, 電気学会誌, Vol.124, No.11, pp.695-698, 2004年11月.

[Key01] Keyence, "CCD Laser Displacement Sensor LK–2000 Series Instruction" (in Japanese).
キーエンス, 「CCDレーザ変位センサLK–2000シリーズ 取扱説明書」.

[Key02] Keyence, "High-Speed and High-Precision CCD Laser Displacement Sensor LK–G Series User's Manual" (in Japanese).
キーエンス, 「高速・高精度CCDレーザ変位計LK–Gシリーズ ユーザーズマニュアル」.

[Kim97] W.J. Kim, "High-Precision Planar Magnetic Levitation," *PhD thesis, Massachusetts Institute of Technology*, June 1997.

[Kim98] W.J. Kim and D. L. Trumper, "High-Precision Magnetic Levitation Stage for Photolithography," *Precision Engineering*, Vol.22, No.2, pp.66-77, April 1998.

[Kim05] S. Verma, W.J. Kim, and H. Shakir, "Multi-Axis Maglev Nanopositioner for Precision Manufacturing and Manipulation Applications," *IEEE Transactions on Industry Applications*, Vol.41, No.5, pp.1159-1167, September/October 2005.

[Kiy04] W. Gao, S. Dejima, H. Yanai, K. Katakura, S. Kiyono, and Y. Tomita, "A Surface Motor-Driven Planar Motion Stage Integrated with an $XY\theta_Z$ Surface Encoder for Precision Positioning," *Precision Engineering*, Vol.28, No.3, pp329-337, July 2004.

[Kiy05a] W. Gao, M. Tano, S. Kiyono, Y. Tomita and T. Sasaki, "Precision Positioning of a Sawyer Motor-driven Stage –Proposal of the Positioning System and Experiments of Micro-Positioning–," *Journal of the Japan Society for Precision Engineering*, Vol.71, No.4, pp.523-527, April 2005 (in Japanese).
高偉, 田野誠, 清野慧, 冨田良幸, 佐々木卓也, 「Sawyer型平面モータの精密位置決めに関する研究 –位置決めシステムの提案と微小位置決め実験–」, 精密工学会誌, Vol.71, No.4, pp.523-527, 2005年4月.

[Kiy05b] S. Dejima, W. Gao, H. Shimizu, S. Kiyono, and Y. Tomita, "Precision Positioning of a Five Degree-of-Freedom Planar Motion Stage," *Mechatronics*, Vol.15, No.8, pp.969-987, October 2005.

[KNa01] K. Nakagawa, F. Kawashima, and T. Arai, "Isotropic SmZrFeN Bonded Magnet Powder with Highest Performance," TOSHIBA REVIEW, Vol.56, No.2, pp.56-59, February 2001 (in Japanese).
中側勝利, 川島史行, 新井智久, 「世界最強の SmZrFeN 系等方性ボンド磁石粉」, 東芝レビュー, Vol.56, No.2, pp.56-59, 2001 年 2 月.

[Kor06] N. Korenaga, "Alignment Apparatus and Exposure Apparatus Using the Same," *U.S. Patent* 7,075,198, July 11, 2006.

[Kos01] J. Liu and T. Koseki, "3 Degrees of Freedom Semi-Zero-Power Maglev Scheme for Two-Dimensional Linear Motor," *The International Symposium on Linear Drives for Industry Applications (LDIA2001)*, pp.114-119, Nagano, Japan, October 2001.

[Kos04] Y. Makino, J. Wang, and T. Koseki, "Control of 6-Degrees-of-Freedom Motion and Design of a Mover Consisting of Three Linear Induction Motors and Three U-Type Electromagnets," *The International Symposium on Power Electronics, Electrical Drive, Automation and Motion (SPEEDAM 2004)*, pp.430-435, Capri, Italy, June 2004.

[Lee08] L. Yan, I.M. Chen, C.K. Lim, G. Yang, W. Lin, and K.M. Lee, "Design and Analysis of a Permanent Magnet Spherical Actuator," *IEEE/ASME Transactions on Mechatronics*, Vol.13, No.2, pp.239-248, April 2008.

[Lee91] K.M. Lee and C.K. Kwan, "Design Concept Development of a Spherical Stepper for Robotic Applications," *IEEE Transactions on Robotics and Automation*, Vol.7, No.1, pp.175-181, February 1991.

[Lem01] LEM, "LA 55-P data sheet".

[Mae01] K. Takemura and T. Maeno, "Design and Control of an Ultrasonic Motor Capable of Generating Multi-DOF Motion," *IEEE/ASME Transactions on Mechatronics*, Vol.6, No.4, pp.499-506, December 2001.

[Mae04] K. Takemura, Y. Ohno, and T. Maeno, "Design of a Plate Type Multi-DOF Ultrasonic Motor and Its Self-Oscillation Driving Circuit," *IEEE/ASME Transactions on Mechatronics*, Vol.9, No.3, pp.474-480, September 2004.

[Mae05] K. Otokawa, K. Takemura, and T. Maeno, "Development of an Arrayed Multi-Degree-of-Freedom Ultrasonic Motor," *The International Symposium on Linear Drives for Industry Applications (LDIA2005)*, pp.258-261, Awaji, Japan, September 2005.

[MDD05] Investigating R&D Committee on Multi-dimensional Drive System, "Investigation of Possibility of Multi-Dimensional Drive System," *IEEJ Technical Report*, No.1029, July 2005 (in Japanese).
多次元ドライブシステム調査専門委員会,「多次元ドライブシステムの可能性を探る」, 電気学会 技術報告, No.1029, 2005 年 7 月.

[MDD07] Investigating R&D Committee on Multi Degrees of Freedom Motors and Their Element Technologies, "Multi Degrees of Freedom Motors and Their Element Technologies", *IEEJ Technical Report*, No.1081, March 2007 (in Japanese).
多自由度モータとその要素技術調査専門委員会,「多自由度モータとその要素技術」, 電気学会 技術報告, No.1081, 2007 年 3 月.

[MDD08] Investigating R&D Committee on Systematize Technology of Multi Degrees of Freedom Motors, "Systematize Technology of Multi Degrees of Freedom Motors", *IEEJ Technical Report*, No.1140, November 2008 (in Japanese).
多自由度モータのシステム化技術調査専門委員会,「多自由度モータのシステム化技術」, 電気学会 技術報告, No.1140, 2008 年 11 月.

[MTT01] MTT, "HERON DSP6067 hardware manual" (in Japanese).
MTT, 「HERON DSP6067 ハードウェア・マニュアル」.

[MTT02] MTT, "HERON ADM16–4 hardware manual" (in Japanese).
MTT, 「HERON ADM16–4 ハードウェア・マニュアル」.

[MTT03] MTT, "HERON DAM12–8 hardware manual" (in Japanese).
MTT, 「HERON DAM12–8 ハードウェア・マニュアル」.

[Nis07] H. Takahashi, O. Nishimura, T. Akita, and H. Tamura, "Development of a 2DOF Control Type Spherical Piezoelectric Motor with Wide Dynamic Range," *The 2007 JSPE Autumn Technical Meeting*, J44, pp.751-752, Asahikawa, September 2007 (in Japanese).
高橋博, 西村修, 秋葉敏克, 田村博幸, 「ダイナミックレンジが広い 2 自由度制御型球面圧電モータの開発」, 2007 年度 精密工学会 秋季大会 学術講演会, J44, pp.751-752, 旭川, 2007 年 9 月.

[Nis08] H. Takahashi, O. Nishimura, and H. Nukada, "Development of a 3DOF Spherical Piezoelectric Motor," *The 2008 JSPE Autumn Technical Meeting*, L36, pp.929-930, Sendai, September 2008 (in Japanese).
高橋博, 西村修, 額田秀記, 「3 自由度球面圧電モータの開発」, 2008 年度 精密工学会 秋季大会 学術講演会, L36, pp.929-930, 仙台, 2008 年 9 月.

[Ohs03] H. Ohsaki, N. Teramura, X. Huang, Y. Tsuboi, and Y. Ootani, "Electromagnetic Characteristics of a Coreless Surface Motor Using Halbach Permanent Magnets," *The International Symposium on Linear Drives for Industry Applications (LDIA2003)*, Birmingham, UK, PL-06 , pp.105-108, September 2003.

[Ohi04] Homepage of Ohira-Inui Laboratory, Nihon University
http://gt1.ce.nihon-u.ac.jp/~ohira/16nensotuken.html.

[Ohi06] S. Inui, N. Inubushi, and Y. Ohira, "Simulation of Controller Characteristics Applied to Magnetic Levitation for an X-Y Linear Synchronous Motor," *IEEJ Transaction on Industry Applications*, Vol.126, No.10, pp.1298-1302, October 2006.

[Ohi98] Y. Ohira, M. Karita, and E. Masada, "Fundamental Characteristics of the Transport Switch System with Levitation Using X-Y LIM," *IEEJ Transaction on Industry Applications*, Vol.118, No.1, pp.105-110, January 1998 (in Japanese).
大平庸一, 苅田充二, 正田英介, 「X-Y LIM を分岐に用いた浮上式搬送・分岐システムの基本特性」, 電気学会 論文誌 D, Vol.118, No.1, pp.105-110, 1998 年 1 月.

[Oza08] K. Ozaki, "Rare-earth magnets without heavy rare-earth elements," *AIST TODAY*, Vol.8, No.5, pp.12-13, May 2008 (in Japanese).
尾崎公洋, 「重希土類を使わない希土類磁石」, 産総研 TODAY, Vol.8, No.5, pp.12-13, 2008 年 5 月.

[Phi06] Philips Applied Technologies, "Magnetic Levitation Planar Technology Backgrounder," *Press Center*, October 2006
http://www.apptech.philips.com/html/press_center/planar_maglev_backgrounder.htm.

[Rau02] B. Dehez, D. Grenier, and B. Raucent, "Two-Degree-of-Freedom Spherical Actuator for Omnimobile Robot" *IEEE International Conference on Robotics and Automation*, Washington, DC, Vol.3, pp.2381-2386, May 2002.

[Rau06] B. Dehez, G. Galary, D. Grenier, and B. Raucent, "Development of a Spherical Induction Motor With Two Degrees of Freedom" *IEEE Transaction on Magnetics*, Vol.42, No.8, pp.2077-2089, August 2006.

[Sag07] M. Sagawa, M. Hamano, and M. Hirabayashi, "Permanent Magnet –Material Science and Application–," Agne Gijutsu Center, September 2007 (in Japanese).
佐川眞人, 浜野正昭, 平林眞, 「永久磁石 ー材料科学と応用ー」, アグネ技術センター, 2007 年 9 月.

[Sag84] M. Sagawa, S. Fujimura, N. Togawa, H. Yamamoto, and Y. Matsuura, "New Material for Permanent Magnets on a Base of Nd and Fe," *Journal of Applied Physics*, Vol.55, No.6, pp.2083-2087, March 1984.

[Sas96] K. Sasae, K. Ioi, Y. Ohtsuki, and Y. Kurosaki, "Development of a Small Actuator with Three Degrees of Rotational Freedom (3rd Report) –Design and Experiment of a Spherical Actuator–," *Journal of the Japan Society for Precision Engineering*, Vol.62, No.4 pp. 599-603, April 1996 (in Japanese).
佐々江啓介, 五百井清, 大築康生, 黒崎泰充, 「3 自由度小型アクチュエータの開発(第 3 報) –球面アクチュエータの設計と性能試験–」, 精密工学会誌, Vol.62, No.4 pp. 599-603, 1996 年 4 月.

[Saw68] B. A. Sawyer, "Magnetic Positioning Device," *U.S. Patent* 3 376 578, April 2, 1968.

[Shi01] Shin-Etsu Rare Earth Magnets, "N48H data sheet" (in Japanese).
信越レア・アースマグネット, 「N48H データシート」
http://www.shinetsu-rare-earth-magnet.jp/support/download.html.

[Taj06] H. Tajima, "Fundamentals of multi-body dynamics," *Tokyo Denki University Press*, November 2006 (in Japanese).
田島洋, 「マルチボディダイナミクスの基礎」, 東京電機大学出版局, 2006 年 11 月.

[Taw05] Y. Tawara and K. Ohashi, "Rare-Earth Permanent Magnet," *Morikita Publishing*, October 2005 (in Japanese).
俵好夫, 大橋健, 「希土類永久磁石」, 森北出版, 2005 年 10 月.

[Tex01] Texas Instruments, "OPA548 data sheet".

[Tom94] Y. Tomita, Y. Koyanagawa, and F. Satoh, "A Surface Motor-Driven Precise Positioning System," *Precision Engineering*, Vol.16, No.3, pp.184-191, July 1994.

[Tom96] Y. Tomita, M. Sugimine, and Y. Koyanagawa, "Development of Six-Axis Precise Positioning System Driven by Surface Motor," *JSME Transaction C*, Vol.62, No.597, pp.1840-1847, May 1996 (in Japanese).
冨田良幸, 杉峰正信, 小梁川靖, 「サーフェスモータを用いた六自由度精密 XY ステージの開発」, 日本機械学会誌 C, Vol.62, No.597, pp.1840-1847, 1996 年 5 月.

[Tru06] D.L. Trumper, "Levitation Linear Motors for Precision Positioning," *IEEJ Transactions on Industry Applications*, Vol.126, No.10, pp.1345-1351, October 2006.

[Tru96] Homepage of the Precision Motion Control Laboratory, Massachusetts Institute of Technology
http://web.mit.edu/pmc/www/pastprojects/Planar/planar.html.

[Tru97] D.L. Trumper, W.J. Kim, and M.E. Williams, "Magnetic Arrays," *U.S. Patent* 5 631 618, May 20, 1997.

[TSh06] T. Shikayama, H. Yoshitake, H. Honda, Y. Yoshida, M.E. Kabir, M. Takaki, and Y. Tsutsui, "Development of Planar Servo Drive," *IEEJ Tech. Meeting on Linear Drives*, SPC-06-169/LD-06-71, pp.13-19, Kanazawa, December 2006 (in Japanese).
鹿山透, 吉武博信, 本田英己, 吉田康, カビルムハマドエナムル, 高木護, 筒井幸雄, 「平面サーボドライブの開発」, 電気学会 半導体電力変換／リニアドライブ合同研究会, SPC-06-169/LD-06-71, pp.13-19, 金沢, 2006 年 12 月.

[Toy07] T. Mashimo, K. Awaga, and S. Toyama, "Development of a Spherical Ultrasonic Motor with an Attitude Sensing System using Optical Fibers," *The IEEE International Conference on Robotics and Automation*, pp.10-14, Rome, Italy, April 2007.

[Toy95] S. Toyama, S. Sugitani, G. Zhang, Y. Miyatani, and K. Nakamura, "Multi Degree of Freedom Spherical Ultrasonic Motor," *The IEEE International Conference on Robotics and Automation*, pp.2935-2940, Nagoya, Japan, May 1995.

[Toy96] S. Toyama, G. Zhang, and O. Miyoshi, "Development of New Generation Spherical Ultrasonic Motor," *The IEEE International Conference on Robotics and Automation*, pp.2871-2876, Minnesota, USA, April 1996.

[Tsu07] J. Tsuchiya and K. Yasuda, "The Positional Detection System for the Surface Motor Using Halbech-Type Permanent Magnets," *The International Symposium on Linear Drives for Industry Applications (LDIA2007)*, OS4.2, Lille, France, September 2007.

[Ueh05] H. Kawano, H. Ando, T. Hirahara, C. Yun, and S. Ueha, "Application of a Multi-DOF Ultrasonic Servomotor in an Auditory Tele-Existence Robot," *IEEE Transaction on Robotics*, Vol.21, No.5, pp.790-800, October 2005.

[Uet03a] T. Ueta and B. Yuan, "Moving Coil Type Planar Motor Control," *U.S. Patent Application Publication* US 2003/0102721 A1, June 5, 2003.

[Uet03b] T. Ueta, B. Yuan, and T.C. Teng, "Moving Magnet Type Planar Motor Control," *U.S. Patent Application Publication* US 2003/0102722 A1, June 5, 2003.

[Van06] A. Lebedev, E. Lomonova, D. Laro, and A.J.A. Vandenput, "Optimal Design Strategy for a Novel Linear Electromechanical Actuator," *IEEJ Transactions on Industry Applications*, Vol.126, No.10, pp.1330-1335, October 2006.

[Van07a] J.W. Jansen, C.M.M. van Lierop, E.A. Lomonova, and A.J.A. Vandenput, "Magnetically Levitated Planar Actuator with Moving Magnets," *The International Electric Machines & Drives Conference (IEMDC'07)*, Vol.1, pp.272-278, Antalya, Turkey, May 2007.

[Van07b] C.M.M. van Lierop, J.W. Jansen, E. Lomonova, A.A.H. Damen, P.P.J. van den Bosch, and A.J.A. Vandenput, "Commutation of a Magnetically Levitated Planar Actuator with Moving-Magnets," *The International Symposium on Linear Drives for Industry Applications (LDIA2007)*, OS6.2, Lille, France, September 2007.

[Van07c] A. Lebedev, D. Thakkar, D. Laro, E. Lomonova, and A.J.A. Vandenput, "Contactless Linear Electromechanical Actuator: Experimental Verification of the Improved Design," *The International Symposium on Linear Drives for Industry Applications (LDIA2007)*, OS11.3, Lille, France, September 2007.

[Yan04] T. Yano, "Multi Dimensional Drive System," *The 14th International Symposium on Power Electronics, Electrical Drives, Automation and Motion (SPEEDAM2004)*, pp.457-462, Capri, Italy, June 2004.

[Yan07] T. Yano, Y. Kubota, T. Shikayama, and T. Suzuki, "Basic Characteristics of a Multi-pole Spherical Synchronous Motor," *International Symposium on Micro-Nano Mechatronics and Human Science (MHS2007)*, pp.383-388, Nagoya, Japan, November 2007.

[Yan08a] T. Yano, Y. Kubota, T. Shikayama, and T. Suzuki, "Development of a Spherical Synchronous Motor with Two Degrees of Freedom," *The 20th Symposium on Electromagnetics and Dynamics (sead20)*, 21B1-1, pp.133-138, Beppu, May 2008 (in Japanese)..
矢野智昭, 久保田義昭, 鹿山透, 鈴木健生,「2 自由度球面同期モータの開発」, 第 20 回「電磁力関連のダイナミクス」シンポジウム, 21B1-1, pp.133-138, 別府, 2008 年 5 月.

[Yan08b] T. Yano, "Development of a High Torque Spherical Motor –Proposal of a Hexahedron–Tetrahedron Based Spherical Stepping Motor–," *Journal of the Japan Society of Applied Electromagnetics and Mechanics*, Vol.16, No.2, pp.108-113, June 2008 (in Japanese).
矢野智昭,「高トルク球面モータの開発 –正六面体と正四面体に基づく球面ステッピングモータの提案–」, 日本 AEM 学会誌, Vol.16, No.2, pp.108-113, 2008 月 6 月.

[Yan93] T. Yano and M. Kaneko, "Basic Consideration of Actuators with Multi Degrees of Freedom Having an Identical Center of Rotation," *Journal of the Robotics Society of Japan*, Vol.11, No.6, pp.107-114, June 1993 (in Japanese).
矢野智昭, 金子真, 「回転中心を同一とする多自由度アクチュエータの基礎的検討」, 日本ロボット学会誌, Vol.11, No.6, pp.107-114, 1993 年 6 月.

[Xia07] H. Li, C. Xia, P. Song, and T. Shi, "Magnetic Field Analysis of A Halbach Array PM Spherical Motor," *IEEE International Conference on Automation and Logistics*, pp.2019-2023, Jinan, China, August 2007.

Publications

Journal Papers

[P1] Y. Ueda and H. Ohsaki, "A Long-Stroke Planar Actuator with Multiple Degrees of Freedom by Minimum Number of Polyphase Currents," *Motion Control, IN-TECH Book,* ISBN: 978-953-7619-X-X, September 2009 (to be submitted).

[P2] Y. Ueda and H. Ohsaki, "Compact Three-Degree-of-Freedom Planar Actuator with Only Six Currents Capable of Driving over Large displacements in Yaw Direction," *IEEJ Transaction on Industry Applications*, Vol.129, No.3, March 2009 (in Japanese, to be published).
上田靖人, 大崎博之, 「2組の3相交流電流を適用してヨー方向に広い範囲で駆動が可能な小形の3自由度平面アクチュエータ」, 電気学会論文誌 D, Vol.129, No.3, 2009年3月 (掲載予定).

[P3] Y. Ueda and H. Ohsaki, "Positioning of a Maglev Planar Actuator by Controlling Three Sets of Two-Phase Currents," *Journal of the Japan Society of Applied Electromagnetics and Mechanics*, Vol.17, No.1, March 2009 (in Japanese, to be published).
上田靖人, 大崎博之, 「3組の2相電流制御による磁気支持平面アクチュエータの位置決め」, 日本 AEM 学会誌, Vol.17, No.1, 2009年3月 (掲載予定).

[P4] Y. Ueda and H. Ohsaki, "Six-Degree-of-Freedom Motion Analysis of a Planar Actuator with a Magnetically Levitated Mover by Six-Phase Current Controls," *IEEE Transaction on Magnetics*, Vol.44, No.11, Part 2, pp.4301-4304, November 2008.

[P5] Y. Ueda and H. Ohsaki, "A Planar Actuator with a Small Mover Traveling over Large Yaw and Translational Displacements," *IEEE Transaction on Magnetics*, Vol.44, No.5, pp.609-616, May 2008.

International Conference Proceedings

[P6] Y. Ueda and H. Ohsaki, "Armature Conductor Design of a Long-Stroke Planar Actuator with Multiple Degrees of Freedom," *The 7th International Symposium on Linear Drives for Industrial Applications (LDIA2009)*, Incheon, Korea, September 2009 (to be submitted).

[P7] Y. Ueda and H. Ohsaki, "Design and Control of a High-Performance Multi-Degree-of-Freedom Planar Actuator," *Symposium of Global COE at University of Tokyo on Secure-Life Electronics*, Tokyo, Japan, January 2009.

[P8] Y. Ueda and H. Ohsaki, "A Planar Actuator with a Magnetically Levitated Mover Capable of Planar Motions by Only Six-Current Control," *The 9th Seoul National University-University of Tokyo Joint Seminar on Electrical Engineering*, Tokyo, Japan, January 2009.

[P9] Y. Ueda and H. Ohsaki, "Six-Degree-of-Freedom Motion Analysis of a Planar Actuator with a Magnetically Levitated Mover by Six-Phase Current Controls," *The International magnetics conference (Intermag2008)*, GH-09, Madrid, Spain, May 2008.

[P10] Y. Ueda and H. Ohsaki, "Large Yaw Motion Control of a Planar Actuator for Two-dimensional Drive," *The 6th International Symposium on Linear Drives for Industrial Applications (LDIA2007)*, OS9.1, Lille, France, September 2007.

[P11] Y. Ueda and H. Ohsaki, "Fundamental characteristics of a small actuator with a magnetically levitated mover," *The 4th Power Conversion Conference (PCC-Nagoya2007)*, pp.614-621, Nagoya, Japan, April 2007.

[P12] Y. Ueda and H. Ohsaki, "Two-dimensional Drive with Yawing motion by a Small Surface Motor," *The 8th Seoul National University-University of Tokyo Joint Seminar on Electrical Engineering*, pp. 79-82, Seoul, Korea, February 2007.

[P13] Y. Ueda and H. Ohsaki, "Application of Vector Control to a Coreless Surface Motor based on a Permanent Magnet Type Linear Synchronous Motor," *The 2006 International Conference on Electrical Machines and Systems (ICEMS2006)*, Nagasaki, Japan, November 2006.

[P14] H. Ohsaki and Y. Ueda, "Numerical Simulation of Mover Motion of a Surface Motor using Halbach Permanent Magnets," *The 18th International Symposium on Power Electronics, Electrical Drives, Automation and Motion (SPEEDAM2006)*, pp.364-367, Taormina, Italy, May 2006.

[P15] Y. Ueda and H. Ohsaki, "Two-dimensional Drive by a Coreless Surface Motor using Halbach Permanent Magnet Array," *The 7th University of Tokyo-Seoul National University Joint Seminar on Electrical Engineering*, pp.157-161, Tokyo, Japan, November 2005.

[P16] Y. Ueda and H. Ohsaki, "Positioning Characteristics of a Coreless Surface Motor using Halbach Permanent Magnet Array," *The 5th International Symposium on Linear Drives for Industrial Applications (LDIA2005)*, pp.270-273, Awaji, Japan, September 2005.

[P17] Y. Ueda, Y. Kawamoto and H. Ohsaki, "Dynamic Characteristics of a Coreless Surface Motor using Halbach Permanent Magnets," *The 5th International Power Electronics Conference (IPEC-Niigata2005)*, S4-1, Niigata, Japan, April 2005.

Domestic Conference Proceedings (in Japanese)

[P18] 上田靖人, 大崎博之, 「6つの電機子導体を持つ磁気支持平面アクチュエータの平面運動制御」, 平成20年 電気学会 産業応用部門大会 III, pp.135-136, 高知, 2007年8月.

Y. Ueda and H. Ohsaki, "Planar Motion Control of a Maglev Planar Actuator with Six Armature Conductors," *IEEJ Annual Meeting on Industry Applications* III, pp.135-136, Kochi, August 2008.

[P19] 上田靖人, 大崎博之, 「光メモリ用の多自由度ドライブ装置の開発動向」, 電気学会 交通・電気鉄道／リニアドライブ合同研究会, TER-08-19/LD-08-19, pp.35-40, 鹿児島, 2008年7月.

Y. Ueda and H. Ohsaki, "Survey of Development of Multi-degree-of-freedom Drive for Optical Memories," *IEEJ Joint Tech. Meeting on Transportation and Electric Railway and Linear Drives*, Kagoshima, TER-08-19/LD-08-19, pp.35-40, July 2008.

[P20] 上田靖人, 大崎博之, 「3組の2相電流制御による磁気支持平面アクチュエータの位置決め」, 第 20 回「電磁力関連のダイナミクス」シンポジウム, 21B2-2, pp.165-170, 別府, 2008年5月.

Y. Ueda and H. Ohsaki, "Positioning of a Maglev Planar Actuator by Controlling Three Sets of Two-Phase Currents," *The 20th Symposium on Electromagnetics and Dynamics (sead20)*, 21B2-2, pp.165-170, Beppu, May 2008.

[P21] 上田靖人, 大崎博之,「平面アクチュエータの3自由度回転姿勢に対する電磁力特性」, 電気学会 全国大会, 5-213, p.321, 福岡, 2008年3月.
Y. Ueda and H. Ohsaki, "Electromagnetic Force Characteristics of a Planar Actuator for Three-Degree-of-Freedom," *IEEJ Annual Meeting*, 5-213, p.321, Fukuoka, March 2008.

[P22] 上田靖人, 大崎博之,「ヨー方向に大変位できる平面アクチュエータの可動子の位置検出」, 電気学会 リニアドライブ研究会, LD-07-34, pp.11-16, 東京, 2007年10月.
Y. Ueda and H. Ohsaki, "Position Detection of a Mover of a Planar Actuator Capable of Traveling over Large Displacements in Yaw Direction," *IEEJ Tech. Meeting on Linear Drives*, LD-07-34, pp.11-16, Tokyo, October 2007.

[P23] 上田靖人, 大崎博之, 「ヨー角に対する平面アクチュエータの位置決め特性」, 平成19年 電気学会 産業応用部門大会 III, pp.137-138, 大阪, 2007年8月.
Y. Ueda and H. Ohsaki, "Positioning characteristics of a planar actuator for yaw angle," *IEEJ Annual Meeting on Industry Applications* III, pp.137-138, Osaka, August 2007.

[P24] 上田靖人, 大崎博之, 「小形平面モータの磁気支持力特性」, 第19回「電磁力関連のダイナミクス」シンポジウム, A312, pp.363-365, 東京, 2007年5月.
Y. Ueda and H. Ohsaki, "Magnetic suspension force characteristics of a small planar motor," *The 19th Symposium on Electromagnetics and Dynamics (sead19)*, A312, pp.363-365, Tokyo, May 2007.

[P25] 上田靖人, 大崎博之,「小型多自由度アクチュエータの電磁力特性」, 電気学会 リニアドライブ研究会, LD-06-63, pp.79-84, 東京, 2006年10月.
Y. Ueda and H. Ohsaki, "Electromagnetic characteristics of a small actuator for multi-degrees of freedom," *IEEJ Tech. Meeting on Linear Drives*, LD-06-63, pp.79-84, Tokyo, October 2006.

[P26] 上田靖人, 大崎博之,「永久磁石同期モータに基づく空心形サーフェスモータの電磁力特性」, 平成18年 電気学会 産業応用部門大会 III, pp.155-158, 名古屋, 2006年8月.
Y. Ueda and H. Ohsaki, "Electromagnetic Characteristics of a Coreless Surface Motor based on Permanent Magnet Type Synchronous Motor," *IEEJ Annual Meeting on Industry Applications* III, pp.155-158, Nagoya, August 2006.

[P27] 上田靖人, 大崎博之, 「小型多自由度アクチュエータの駆動に関する検討」, 電気学会 交通・電気鉄道／リニアドライブ合同研究会, TER-06-51/LD-06-29, pp.19-24, 札幌, 2006 年 7 月.

Y. Ueda and H. Ohsaki, "Investigation about drive of a small actuator for multi-degrees of freedom," *IEEJ Joint Tech. Meeting on Transportation and Electric Railway and Linear Drives*, TER-06-51/LD-06-29, pp.19-24, Sapporo, July 2006.

[P28] 上田靖人, 大崎博之, 「永久磁石リニア同期モータを原理とする空心形サーフェスモータの駆動特性に関する考察」, 第 18 回「電磁力関連のダイナミクス」シンポジウム, A2P01, pp.489-494, 神戸, 2006 年 5 月.

Y. Ueda and H. Ohsaki, "Discussion about Drive Control of a Coreless Surface Motor based on Permanent Magnet Type Linear Synchronous Motor," *The 18th Symposium on Electromagnetics and Dynamics (sead18)*, A2P01, pp.489-494, Kobe, May 2006.

[P29] 上田靖人, 河本泰典, 大崎博之, 「ハルバッハ磁石を用いた空心形サーフェスモータにおける可動子の回転運動抑制制御」, 第 17 回「電磁力関連のダイナミクス」シンポジウム, pp.249-252, 高知, 2005 年 6 月.

Y. Ueda and H. Ohsaki, "Control of Mover Yawing Motion in a Coreless Surface Motor using Halbach Permanent Magnet," *The 17th Symposium on Electromagnetics and Dynamics (sead17)*, 2AM06, pp.249-252, Kochi, June 2005.

[P30] 河本泰典, 上田靖人, 大崎博之, 「ハルバッハ磁石を用いた空心形サーフェスモータの駆動特性」, 電気学会 リニアドライブ／半導体電力変換合同研究会, LD-04-98/SPC-04-170, pp.7-12, 諏訪, 2004 年 12 月.

Y. Kawamoto, Y. Ueda, and H. Ohsaki, "Drive Characteristics of a Coreless Type Surface Motor Using Halbach Permanent Magnets," *IEEJ Joint Tech. Meeting on Linear Drives and Semiconductor Power Converter*, LD-04-98/SPC-04-170, pp.7-12, Suwa, December 2004.

[P31] 上田靖人, 大崎博之, 正田英介, 「電磁吸引式磁気浮上車両の支持系へのファジィ制御の導入」, 電気学会 交通・電気鉄道／リニアドライブ合同研究会, TER-04-31/LD-04-52, pp.1-6, 名古屋, 2004 年 7 月.

Y. Ueda, H. Ohsaki, and E. Masada, "Application of Fuzzy Control to Suspension System of Electromagnetic Suspension Type Magnetically Levitated Vehicle," *IEEJ Joint Tech. Meeting on Transportation and Electric Railway and Linear Drives*, TER-04-31/LD-04-52, pp.1-6, Nagoya, July 2004.

Others

[P32] Y. Ueda, H. Uesugi, M. Nara, Y. Fujii, and E. Ohkuma, "Campus Life is Changed!?," *The Journal of IEEJ*, Vol. 126, No. 12, pp.775-778, December 2006 (in Japanese).
上田靖人, 上杉 春奈, 奈良 雅文, 藤井 康正, 大熊 栄一, 「キャンパスライフが変わる!?」, 電気学会誌, Vol. 126, No. 12, pp.775-778, 2006 年 12 月.

[P33] Y. Ueda, "Systematized technologies of multi degrees of freedom motors (Section 7.3: Lens Drive for Optical Memories)," *IEEJ Technical Report*, No.1140, pp.59-63, November 2008 (in Japanese).
上田靖人,「多自由度モータのシステム化技術(7.3 節：光メモリ用のレンズ駆動)」, 電気学会 技術報告 No.1140, pp.59-63, 2008 年 11 月.